First Principles Calculations of Quantum Transport Properties through π-Conjugated Molecules

von

Paul Baumeister

Diplomarbeit in Physik

vorgelegt der

Fakultät für Mathematik, Informatik und Naturwissenschaften
der Rheinisch-Westfälischen Technischen Hochschule Aachen

im
Februar 2008

angefertigt am

Institut für Festkörperforschung (IFF)
Forschungszentrum Jülich
Prof. Dr. Stefan Blügel

Contents

Abstract

Electronic structure calculations provide insight into the physics behind a large variety of properties of solids, among them transport properties. Density functional theory has proven to be a very powerful tool for this. Real-space methods of electronic structure calculations have the advantages that they allow flexible boundary conditions and, even more importantly, are expected to perform excellent on massively parallel computers. This opens new opportunities for investigating entire nano architectures composed of hundreds of atoms. Combining electronic structure and electronic transport calculations in a consistent formalism provides a framework for simulating and predicting the functionality of realistic quantum devices. In this work, real-space finite difference method based on norm-conserving pseudopotentials is presented as a new tool for electronic structure calculations. The electronic structure and transport properties have been determined for terephthalic acid, suspended between Cu(110) surfaces. The zero voltage conductivity vanishes due to the insulating nature of this molecule, but shifting of the chemical potential in the junction allows drastic changes of the electron transmission.

1 Introduction

The electronic structure of an atomic configuration is a major key towards understanding and predicting a wide range of material properties. Chemists and physicists are interested in quantities that can be observed and measured and thus verified in an experimental manner and calculated by realistic simulations. This includes mechanical properties such as bulk-, shear- and torsion-moduli, stiffness and rigidity as well as optical absorption spectra, thermodynamical properties such as heat capacity, melting points, structure formation and excitations and electrical properties such as dielectric response and conductivity. This work will concentrate on the methods to calculate the electronic structure, focusing on transport properties.

The electronic structure is governed by the Schrödinger equation. For single-electron systems, this equation can solved analytically(at least for certain potentials); such solutions have been known since the discovery of quantum mechanics. However, the interesting effects arise from the interactions of many electrons. An analytical solution for the many-body Schrödinger has not been found; the only way to determine electronic structure of atoms and systems of many atoms is numerically. Physics represented on a computer is always subject to certain constraints and limitations. The major approximation is that any number, infinite in nature, becomes finite on the machine. For example real numbers $\mathbb{R}$ are truncated to the finite subset of rational numbers $\mathbb{Q}$, i.e. $\mathbb{Q}_{\text{Computer}} \subset \mathbb{Q} \subset \mathbb{R}$. This effect is small for most applications and can be neglected with respect to other approximations. Quantum mechanics, especially considering solutions of the Schrödinger equation, are based on infinite-dimensional function spaces. The truncation to finite-dimensional subspace carries certain errors. However, the result of a calculation is assumed to converge with respect to the number of dimensions.

The solution of the many-body Schrödinger equation meets a computational effort that increases exponentially with the number of dimensions and electrons. This behavior can be circumvented by applying mean field approximations to the physics of a many-body electron system. In the framework of density functional theory, the local density [1, 2] approximation allows to decouple the enormous sets of non-linear equations. This works well for a system of weakly interacting electrons.

Density functional calculations have been performed on a vast variety of systems in the last decades. Many properties of complicated systems have been investigated that require a relatively small computational effort. The effort mainly depends on aspects of the system size such as volume, number of atoms, number of electrons,

but it also depends strongly on the symmetries as well. Every symmetry introduces constraints that, on one hand, reduce the number of degrees of freedom and, on the other hand, decouple the equations further. Consequently, given symmetries can always be exploited to reduce and restructure the computation.

Nowadays, interests point towards calculations of systems of low symmetry and large number of atoms, thus require a larger effort. Examples such as single impurities in bulk systems, molecules on surfaces and entire nano devices are challenging tasks. The growing demand of larger systems is compatible with the development of computer techniques which has grown exponentially in both, the capacity and the speed, over the last four decades. However, processor technologies will come to a halt in increasing the clock rate since the physical limits of the materials in use are about to be exceeded soon. The development of supercomputers has focused on multicore systems. Massively parallel machines are dominating the top-ten lists of the fastest computers of the world. The distribution of tasks and memory constricts the applications running efficiently on such systems to a certain type of parallel code architecture. For large setups, the real-space approach towards density functional calculations allows exploitation of the locality of the special operators very efficiently. The entire real-space region is therefore decomposed into domains so that the task of each domain can be assigned to one process element. Usually, one process element is represented by one node, i.e. a set of one or more processors. The parallel efficiency for totally independent tasks on a massively parallel computer is 100%. Dependencies between the tasks need additional communication which is not necessary running on a single processor. This decreases the efficiency on a parallel machine. If the code architecture provides a restricted communication scheme, the parallel efficiency is supposed to be very high. It is an intrinsic property of local and localized operations in real-space to limit the communication to the nearest-neighbors of a process element. This promises an efficient usage of the supercomputers.

Nano device engineering tries [3] to find new ways to employ quantum effects for information technology. The conventional transistor is commonly used as an amplifier in its linear region. For digital information technology, however, the best characteristic of a transistor would be a step function rather than a smoothly varying analog switch. Certain molecules have turned out to be very promising candidates for expedient digital switches. The underlying mechanism is based on molecules that are stable in two configurations and can therefore be tuned and switched by external fields easily. Scanning tunnelling microscopy measurements and density functional calculations have shown that organic molecules with a carboxylate group easily adsorb to certain surface sites on copper (110) surface. This is a promising basis for creating a functional device at the surface.

In this work, a novel real-space finite difference method [4] based on norm-conserving pseudopotentials are applied to compute electronic structures and transport properties on a transport setup of terephthalic acid. In particular, equidistant real-space

grids are used to represent wave functions and potentials of the density-functional calculations. Kleinman-Bylander type norm-conserving pseudopotentials [5, 6, 7] are applied to describe the properties of valence electrons in absence of core electrons not relevant for bonding or transport properties.

The real-space finite-difference approximations [4] enables the evaluation of the kinetic energy for real-space represented wave functions and is also applied to solve the Poisson equation in an iterative scheme. In general, iterative solvers [8, 9] dominate in most points of the real-space electronic structure calculation because the large number of degrees of freedom affects direct methods to become too expensive. The eigenvalue equation, for example, is solved by a conjugate gradient algorithm. Ono's double-grid technique [10] to treat the norm-conserving pseudopotential enables the use of relatively coarse grid spacings. This way higher accuracy of the results can be achieved and unphysical oscillations can be reduced.

On the basis of the pre-calculated electronic structure, electronic transport properties of terephthalic acid and similar aromatic molecule are determined using the over-bridging boundary method. In the Landauer-Büttiker transport picture [11], incident electron waves are matched to the solutions of the junction region. Therefore, the equilibriums Green-function of the combined system, the molecule and the surfaces of the electrodes, is determined. The effect of changing various environmental parameters on the transport properties are investigated in detail. π-conjugated molecules show delocalized electronic states forming aromatic bonds. These are chosen for this investigation because their electronic structure is well known [12, 13], especially their adsorption to the metal surface [14]. These molecules are promising candidates for applications as molecular nano device, since their functionality can be tuned almost arbitrarily [15].

Electronic devices of anorganic semiconductors have experienced the *top-down* scaling, miniaturizing the structures down to the wavelength UV light which is commonly used for lithography processes. However, these devices where well described by classical physics. Disregarding the difficulties in the production, even smaller circuit structure e.g. on a silicon chip will somewhen reach the quantum limit and its classical behavior will be influenced by steric effects. Molecular devices are the basis for the so called *bottom-up* approach for electronics. The single molecule as functional unit opens new ways of tailoring electronic devices which are several nanometers in size. The synthesis of organic compounds and their deposition on metallic surfaces are well known fields of chemistry which promises cheap production costs. Therefore, the application of properly designed organic molecules evokes an increasing interest. This work provides insight into the real-space finite-difference formalism for the calculation of the electronic structure and, based upon that, also transport properties. The first chapters will explain the approximations applied to the physics of the electronic structure. In particular, they will focus on the way, the local density approximation makes it possible to exploit the simplicity of density functional theory. Furthermore,

the numerical representation of the physical quantities and the numerical methods that enable the computation are introduced. These are the real-space grid, the finite difference approximation and the pseudopotential method. Taking these building blocks as a basis, the computational scheme for the determination of the electronic structure is outlined in detail. Electronic transport calculations may be performed on top of an electronic structure calculation. Therefore, the subsequent chapter treats the transport formalism in the single-particle picture and explains the jellium approximation applied to the molecular transport setup that has been investigated in this work. The transport properties of terephthalic acid and a set of similar, π-conjugated molecules, embedded between two copper leads, in various geometries are discussed in the results section.

2 Density Functional Theory

2.1 The many-body system

Quantum mechanics fully describe the phenomena of the nano world. The most observed properties of solid materials can be explained by solutions of the non-relativistic many-body Schrödinger equation $\mathrm{i}\frac{\partial}{\partial t}\left|\Psi_{\mathrm{full}}\right\rangle = \hat{H}_{\mathrm{full}}\left|\Psi_{\mathrm{full}}\right\rangle$, where

$$\begin{aligned}\hat{H}_{\mathrm{full}} = &\sum_{i}^{N_{\mathrm{e}}} \frac{\mathbf{p}_i{}^2}{2m_{\mathrm{e}}} + \sum_{k}^{N_{\mathrm{a}}} \frac{\mathbf{p}_k{}^2}{2m_k} - \sum_{i}^{N_{\mathrm{e}}}\sum_{k}^{N_{\mathrm{a}}} \frac{Z_k}{|\mathbf{r}_i - \mathbf{R}_k|} \\ &+ \sum_{i}^{N_{\mathrm{e}}}\sum_{j<i} \frac{1}{|\mathbf{r}_j - \mathbf{r}_i|} + \sum_{k}^{N_{\mathrm{a}}}\sum_{l<k} \frac{Z_l Z_k}{|\mathbf{R}_l - \mathbf{R}_k|}.\end{aligned} \tag{2.1}$$

Here the Hamiltonian $\hat{H}_{\mathrm{full}}$ contains the kinetic energy of the electrons, kinetic energy of the cores, the interactions of electrons with atom cores, electrons with electrons and cores with cores (in this order). It treats the atom cores as quantum particles. However the very different scale of masses $m_{\mathrm{core}} \approx 3676 \cdot Z m_{\mathrm{e}}$ justifies the separation of the of motions according to the different time scales. Therefore it is possible to treat only the electronic part of the Hamiltonian quantum mechanically assuming the atomic positions $\mathbf{R}_k$ to be parameters i.e. the atomic motion is treated classically even though their vibrational motion shows quantum nature as well. This so called *Born-Oppenheimer* approximation has shown to hold in most cases. It fails only in very special scenarios where *vibronic* (combined vibrational and electronic) states play a central role.

Density functional theory allows an approach towards solving the many-body Schrödinger equation for interacting electrons. This equation is the basis for (non-relativistic) quantum mechanics describing atomic interactions

$$\mathrm{i}\frac{\partial}{\partial t}\left|\Psi_{\mathrm{MB}}\right\rangle = \hat{H}_{\mathrm{MB}}\left|\Psi_{\mathrm{MB}}\right\rangle \tag{2.2}$$

with the electronic Hamiltonian

$$\hat{H}_{\mathrm{MB}}\{\mathbf{R}_k\} = \sum_{i}^{N_{\mathrm{e}}} \frac{\mathbf{p}_i{}^2}{2m_{\mathrm{e}}} + \sum_{i}^{N_{\mathrm{e}}}\sum_{k}^{N_{\mathrm{a}}} \frac{Z_k}{|\mathbf{r}_i - \mathbf{R}_k|} + \sum_{i}^{N_{\mathrm{e}}}\sum_{j<i} \frac{1}{|\mathbf{r}_j - \mathbf{r}_i|} \tag{2.3}$$

The challenge arising from this equation is the dimensionality of the underlying Hilbert space. Considering for example a system where each particle has two accessible eigenstates, e.g. a spin-$\frac{1}{2}$ system, the many-body Hilbert space is 2^N-dimensional. The exponential growth makes it problematic to find eigensolutions of the Schrödinger equation, since conventional numerical solvers for eigensystems scale with the third power of the dimension. This leads to a total workload proportional to $\propto 2^{3N}$ for finding the exact solutions of a spin system with N particles.
Our problem becomes even more challenging with electrons. Quantum mechanics tells us to express position and momentum of the electrons by a continuous distribution function. So we have to consider an entire function space to represent their state. Most approximations are based on truncating these function spaces to subspaces of a finite number of dimensions. However there is a constant tradeoff: The number of basis functions usually has to be kept large to preserve the accuracy of results and small at the same time because computations using d basis functions would still scale proportional to $\propto d^{3N}$, which makes this practically impossible for a system with a few electrons.
Electrons interact in many ways, but two interactions are most important: The Coulomb repulsion which is due to their charge and the exchange mechanism which is due to the fact that all electrons are identical and therefore cannot be distinguished from each other. Consider the electronic Hamiltonian of the many body system of interacting electrons

$$\hat{H}_{\mathrm{MB}} = \sum_{i}^{N_e} \frac{{\mathbf{p}_i}^2}{2m_e} + \sum_{i}^{N_e} V(\mathbf{r}_i) + \sum_{j>i}^{N_e} \frac{1}{|\mathbf{r}_j - \mathbf{r}_i|} \tag{2.4}$$

where $V(\mathbf{r})$ stands for the one-particle external potential of the atom cores like the electron-core interaction in equation (2.1). Optionally an additional electrical field can be included. Regarding the third sum, one may recognize the Coulomb energy from two repelling electrons according to the laws of electrostatics. The other interaction of the electrons, the exchange mechanism, is not directly visible as an expression in the Hamiltonian. It arises from the fact that the many-body wave function has to be antisymmetric under exchange of any two identical particles. Consider a two-particle wave function $\Psi_{\mathrm{ManyBody}}(\mathbf{r}_1, s_1; \mathbf{r}_2, s_2)$ with the spatial coordinates $\mathbf{r}_i$ and the spin states s_i. The Pauli exclusion principle demands that no two fermions are in the same state. The consequence is a wave function that is antisymmetric under the exchange of the particles, i.e. simultaneously interchanging $\mathbf{r}_1 \leftrightarrow \mathbf{r}_2$ and $s_1 \leftrightarrow s_2$ gives a factor -1:

$$\Psi_{\mathrm{MB}}(\mathbf{r}_2, s_2; \mathbf{r}_1, s_1) = -\Psi_{\mathrm{MB}}(\mathbf{r}_1, s_1; \mathbf{r}_2, s_2) \tag{2.5}$$

Now, if $\mathbf{r}_1 = \mathbf{r}_2 = \mathbf{r}$ and $s_1 = s_2 = s$ this results in

$$\Psi_{\mathrm{MB}}(\mathbf{r}, s; \mathbf{r}, s) = -\Psi_{\mathrm{MB}}(\mathbf{r}, s; \mathbf{r}, s) \tag{2.6}$$

i.e. $\Psi_{\text{manybody}}(\mathbf{r}, s; \mathbf{r}, s) = 0$. Therefore no two electrons can have the same position and spin coordinates. This holds for more than two particles, too. In practice this means that two electrons with the same spin will avoid being near to each other, giving a minimum in the spatial electron-electron correlation function known as the exchange hole. Because the electrons avoid coming close to each other, where the Hartree energy is high, the exchange hole leads to a lowering of the total energy.

Density functional theory for systems of interacting electrons was first introduced by Hohenberg and Kohn(1964) [16] who investigated on the Thomas-Fermi model. It was found that the electronic ground state energy only depends on the total electron density. From that point on, many different attempts towards finding the predicted unique mapping (called functional) between the total ground state density $n(\mathbf{r})$ and the total energy $E\{n(\mathbf{r})\}$ have been made. Under the assumption that the exact functional is known, density-functional theory is an exact method and should reproduce realistic ground state properties. The functional may be divided into the following parts

$$E\{n(\mathbf{r})\} = T_e\{n(\mathbf{r})\} + E_{ee}\{n(\mathbf{r})\} + E_{\text{ext}}\{n(\mathbf{r})\} \tag{2.7}$$

with the total kinetic energy $T_e\{n(\mathbf{r})\}$, the energy from electron-electron interactions $E_{e-e}\{n(\mathbf{r})\}$ and the contribution from external potentials $E_{\text{ext}}\{n(\mathbf{r})\}$ including the attractive atom core potentials. The simplest part of this expression is the energy contribution due to the external potential

$$E_{\text{ext}}\{n(\mathbf{r})\} = \int_V \mathrm{d}^3\mathbf{r}\, n(\mathbf{r}) V_{\text{ext}}(\mathbf{r}) \tag{2.8}$$

The electron-electron interaction energy may be evaluated according to

$$E_{\text{ee}}\{n(\mathbf{r})\} = \int_V \mathrm{d}^3\mathbf{r} \int_V \mathrm{d}^3\mathbf{r}' \, \frac{n(\mathbf{r}) n(\mathbf{r}')}{\mathbf{r} - \mathbf{r}'} + \int_V \mathrm{d}^3\mathbf{r}\, n(\mathbf{r}) \epsilon_{\text{xc}}\{n(\mathbf{r})\} \tag{2.9}$$

Herein the electrostatic repulsion of the electrons is included. Additionally the contributions ϵ_{xc} enter here that will be discussed later.
More complicated is the evaluation of the kinetic energy out of the density. Given the exact many-body wave-function, the kinetic energy could be evaluated via the Laplacian, in reciprocal space or real space. The latter becomes

$$T_e\{n(\mathbf{r})\} = -\frac{1}{2} \int_V \prod_{k=1}^{N} \mathrm{d}^3\mathbf{r}_k \, \Psi^*_{\text{MB}}(\mathbf{r}_1; \ldots; \mathbf{r}_N) \left[\sum_{i=1}^{N} \Delta_{\mathbf{r}_i} \right] \Psi_{\text{MB}}(\mathbf{r}_1; \ldots; \mathbf{r}_N) \tag{2.10}$$

The mapping $\Psi_{\text{MB}} \longrightarrow n(\mathbf{r})$ is well known because the density is just the probability of finding a particle at position $\mathbf{r}$, so $n(\mathbf{r}) = \langle \Psi_{\text{MB}} | \mathbf{r} \rangle \langle \mathbf{r} | \Psi_{\text{MB}} \rangle$. However the inverse is totally unknown.

An attempt towards finding the correct many-body wave function is the Hartree-Fock method using a determinant of single particle wave functions proposed by Slater [17]

$$\Psi^{(n)}_{\text{manybody}}(\mathbf{r}_1,\ldots,\mathbf{r}_n) = \begin{vmatrix} \phi_1(\mathbf{r}_1) & \phi_2(\mathbf{r}_1) & \cdots & \phi_n(\mathbf{r}_1) \\ \phi_1(\mathbf{r}_2) & \phi_2(\mathbf{r}_2) & & \phi_n(\mathbf{r}_2) \\ \vdots & & \ddots & \vdots \\ \phi_1(\mathbf{r}_n) & \phi_2(\mathbf{r}_n) & \cdots & \phi_n(\mathbf{r}_n) \end{vmatrix} \tag{2.11}$$

The mathematical construct of determinants intrinsically satisfies the antisymmetry constraint imposed by the Pauli principle. The single particle states $\phi_i(\mathbf{r})$ have to obey the Hartree-Fock equation

$$\begin{aligned} &\left(-\frac{1}{2}\Delta + \hat{V}_{\text{loc}}(\mathbf{r})\right)|\phi_i\rangle + \left(\sum_k \langle\phi_k| \frac{1}{|\mathbf{r}-\mathbf{r}'|} |\phi_k\rangle\right)|\phi_i\rangle \\ &- \sum_k \left(\langle\phi_k| \frac{1}{|\mathbf{r}-\mathbf{r}'|} |\phi_i\rangle\right)|\phi_k\rangle = E_i\,|\phi_i\rangle \end{aligned} \tag{2.12}$$

which follows from the many-body Schrödinger equation with the *ansatz* of a Slater-determinant for the many-body wave function. This leads to a very costly computational scheme that turned out not to contain the full electron-electron interaction. Even though the exchange interaction is treated in an exact manner, the *correlation* effect is not included in this.
Correlations in the statistical meaning are cross dependencies between the particles coordinates. Assuming the many body wave function as a product of single particle states gives a totally uncorrelated description for the electrons i.e. their probability distributions are independent of each other.

Similar to the single-particle wave functions of the Hartree-Fock method, single-particle wave functions are constructed in density functional calculations which enable to evaluate the kinetic energy functional. Kohn and Sham(1965) [1] showed that these single-particle states have to obey the Kohn-Sham equation which takes the form of a one-particle Schrödinger equation with an additional term representing the interaction of the single electron with the total density of all electrons

$$\hat{H}_{\text{KS}}\,|\psi_{\text{KS}}\rangle = \left\{\frac{\mathbf{p}^2}{2m_e} + \hat{V}_{\text{eff}}\{n\}\right\}|\psi_{\text{KS}}\rangle = \epsilon_{\text{KS}}\,|\psi_{\text{KS}}\rangle\,. \tag{2.13}$$

Here the right hand side term ϵ_{KS} has the unit of an energy but does not necessarily represent a physically measurable quantity because it is the single-particle energy of the non-interacting system. From the mathematical point of view it rather must be understood as a Lagrange multiplier that arises due the conservation of the particle number. Nevertheless the Kohn-Sham energies ϵ_{KS} are often treated as physically meaningful and so are derived quantities such as the density of states.
The effective potential operator $\hat{V}_{\text{eff}}$ includes all interactions of the single electron;

the electrostatic interaction with the electron density (Hartree potential), the ion potential and any external potential are treated classically. Corrections for the neglected exchange mechanism mentioned above, corrections for the kinetic energy and a special effect called *correlation* are included in the exchange-correlation potential $V_{\mathrm{xc}}\{n\}(\mathbf{r})$.

2.2 Mean-field approximation

The usage of density functionals has turned out to be a very successful application of a mean field method. The mean field approximation reduces a many body problem to a single particle system by creating an effective interaction. Here it can be considered as mapping a system with N interacting electrons to N systems of non-interacting electrons.

$$\text{exact complexity} \quad d^{3N} \quad \longrightarrow \quad N\ d^3 \quad \text{mean field complexity}$$

It is easy to see that this, on the one hand reduces the complexity but on the other hand truncates interactions in a certain way. Density functional calculations for example do not reproduce the effects observed in materials whose electronic structure is known to be strongly correlated.

2.3 Local density approximation

The simplest kind of approximation gives a potential $V_{\mathrm{xc}}\{n(\mathbf{r}')\}(\mathbf{r})$ that includes interactions with the total density $n(\mathbf{r}')$ only at the position $\mathbf{r}' = \mathbf{r}$. Therefore it is called the *local density approximation* (LDA). It is based on the assumption that the exchange interaction can be approximated by the exchange of a single electron with constant density of electrons all over space that has the value $n(\mathbf{r})$. The exchange energy then is given as

$$E_{\mathrm{x}}\{n\} = \int_V \mathrm{d}^3\mathbf{r}\ n(\mathbf{r})\epsilon_{\mathrm{x}}(n(\mathbf{r})) \quad \epsilon_{\mathrm{x}}(n) = -\frac{3}{4\pi}(3\pi^2\, n)^{\frac{1}{3}} \tag{2.14}$$

calculated in the Hartree-Fock model. The potential arising from this is the functional derivative with respect to the density

$$V_{\mathrm{x}}\{n(\mathbf{r})\} = \frac{\delta\epsilon_{\mathrm{x}}(n)}{\delta n(\mathbf{r})} = -\frac{1}{4\pi}(3\pi^2)^{\frac{1}{3}}\, n^{-\frac{2}{3}} \tag{2.15}$$

The contributions from correlation are evaluated by a numerically approximated function that has been fitted to exact many-body results achieved from Quantum Monte-Carlo simulations. For magnetic systems, the exchange-correlation potential depends on the total density $n(\mathbf{r})$ and the magnetization density $m(\mathbf{r})$ where

$n(\mathbf{r}) = n_\uparrow(\mathbf{r}) + n_\downarrow(\mathbf{r})$ and $m(\mathbf{r}) = n_\uparrow(\mathbf{r}) - n_\downarrow(\mathbf{r})$ and is then called local *spin* density approximation (LSDA).

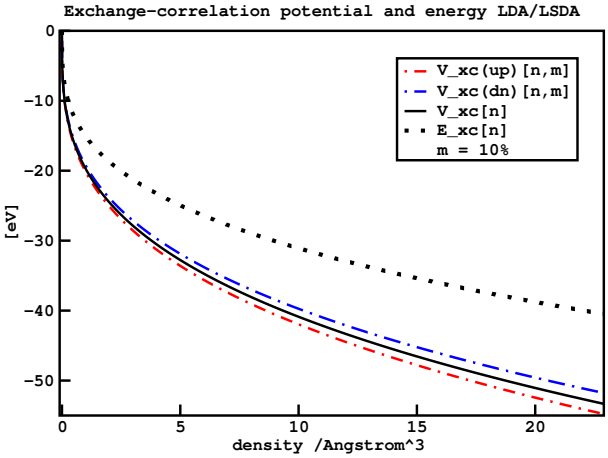

Figure 2.1: Exchange-correlation potential $V_{\mathrm{xc}}(n)$ and energy $\epsilon_{\mathrm{xc}}(n)$ for the local density approximation. Including spin (LSDA), the potential depends on the local magnetization. Here a 10% magnetization is shown.

Throughout this work the local density approximation of Perdew and Zunger (1981) [2] has been used.

3 Real-Space Finite-Difference

3.1 Uniform grids

The kinetic energy operator appears in the Schrödinger equation in the form of the Laplacian, i.e. the second derivative with respect to all three spatial directions. The central finite difference method (FD) truncates this derivative to a difference quotient. Consider an analytical function $f(x)$ and its representation on a uniform grid with a constant grid spacing h. The values $f_i = f(x_i)$ correspond to the function evaluated at the grid points x_i. By using a Taylor expansion up to second order we can express the value of the analytical function at neighboring points to both sides.

$$\begin{aligned} f_{i-1} = f(x_{i-1}) = f(x_i - h) &\overset{\text{Taylor}}{=} f(x_i) - hf'(x_i) + \frac{1}{2}h^2 f''(x_i) + \mathcal{O}(h^3) \\ f_i = f(x_i) & \\ f_{i+1} = f(x_{i+1}) = f(x_i + h) &\overset{\text{Taylor}}{=} f(x_i) + hf'(x_i) + \frac{1}{2}h^2 f''(x_i) + \mathcal{O}(h^3) \end{aligned} \tag{3.1}$$

This can be rewritten in matrix form as

$$\begin{pmatrix} f_{i-1} \\ f_i \\ f_{i+1} \end{pmatrix} = \begin{pmatrix} 1 & -1 & \frac{1}{2} \\ 1 & 0 & 0 \\ 1 & 1 & \frac{1}{2} \end{pmatrix} \begin{pmatrix} f(x_i) \\ hf'(x_i) \\ h^2 f''(x_i) \end{pmatrix} \tag{3.2}$$

This is a matrix relation between the vector of function values (f_{i-1}, f_i, f_{i+1}) and the derivatives $(f(x_i), hf'(x_i), h^2 f''(x_i))$ of the function $f(x)$ at the central grid points x_i. The corresponding powers of h have been kept for simplicity of the notation. Inversion of this matrix shows that the zeroth, first and second derivative of f can be expressed as a linear combination of the values f_{i-1}, f_i and f_{i+1}

$$\begin{pmatrix} 0 & 1 & 0 \\ -\frac{1}{2} & 0 & \frac{1}{2} \\ 1 & -2 & 1 \end{pmatrix} \begin{pmatrix} f_{i-1} \\ f_i \\ f_{i+1} \end{pmatrix} = \begin{pmatrix} f(x_i) \\ hf'(x_i) \\ h^2 f''(x_i) \end{pmatrix} \tag{3.3}$$

$$(N_f = 1) \quad \Rightarrow \quad f''(x_i) = \frac{1}{h^2}\left(f_{i-1} - 2f_i + f_{i+1}\right) \tag{3.4}$$

Thus, the coefficients for the second derivative are $c_{-1}^{''} = 1$, $c_0^{''} = -2$ and $c_1^{''} = 1$. It is easy to see that even derivatives (zeroth, second, fourth...) have a symmetric coefficient scheme while the symmetric coefficient is antisymmetric for odd derivatives (first, third...). To calculate higher derivatives than the second, one has to perform

the Taylor expansion for more than one neighboring site. With this method an even more accurate approximation for the second derivative can be achieved. Table 3.1 shows the coefficients for different numbers of considered neighbors, N_f.
The general case reads

$$f(x_{i+j}) = f(x_i + jh) = f_{i+j} = \sum_{k=0}^{2N_f} \frac{(jh)^k}{k!} \frac{\partial^k f(x_i)}{\partial x^k} \; + \mathcal{O}(h^{2N_f+1}) \; , j \in [-N_f, N_f] \tag{3.5}$$

The matrix of Taylor coeffients then is $t_{jk} = j^k/k!$. So the coefficient scheme for the first $2\,N_f$ derivatives are given by the rows of the inverse matrix of t_{jk}. For the m-th derivative, one finds

$$f_{\mathrm{FD}}^{(m)}(x_i) = \frac{1}{h^m} \sum_{l=-N_f}^{N_f} \left\{[t_{jk}]^{-1}\right\}_{ml} \; f_{i+l} \tag{3.6}$$

An explicit formula for high order coefficients of the first and second derivatives that does not require the inversion of a $(2N_f + 1) \times (2N_f + 1)$ matrix can be found later (Chapter 3.3).

$i-j$	0	±1	±2	±3	±4	±5	±6
N_f=1	-2.000	1.000					
N_f=2	-2.500	1.333	-0.083				
N_f=3	-2.722	1.500	-0.150	0.011			
N_f=4	-2.847	1.600	-0.200	0.025	-0.0018		
N_f=5	-2.927	1.667	-0.238	0.040	-0.0050	0.00032	
N_f=6	-2.982	1.714	-0.268	0.053	-0.0089	0.00103	-0.00006

Table 3.1: Finite difference coefficients for the second derivative. The number of finite difference neighbors $2\,N_f$ determines the order of approximation. Zero-valued coefficients are not shown. The error from this approach is of the order h^{2N_f}.

The second derivative relates the grid points x_i and x_j for all $|i - j| < N_f$ so the Laplacian operator is not local (diagonal in spatial representation) and is represented by a symmetric banded matrix. In the case of one spatial dimension these bands enclose the diagonal from the upper and lower site as depicted in Figure 3.1.

The sparsity of these matrices enables a banded storage form. If one includes the 3-dimensional case, these bands are not necessarily close to the diagonal any more. Periodic boundary conditions cause non-zero matrix elements relating the first and last grid points. The second picture in Figure 3.1 differs from the first only by an

entry in the upper left and lower right corner.
The absolute value of these matrix element is as before determined from the finite difference coefficients but there is one degree of freedom in the complex phase. The physics behind it is a phase modulation of a complex wave function which extends over an infinite number of unit cells. Therefore the Bloch-theorem can be applied and the complex phase factor of the upper right element is set to $c_1\, e^{-ikL}$ where L denotes the extend of the one-dimensional unit cell. The kinetic energy operator is an observable and so its matrix representation is hermitian. This fully determines the lower left element to be $c_1\, e^{ikL}$, where c_1 is real.

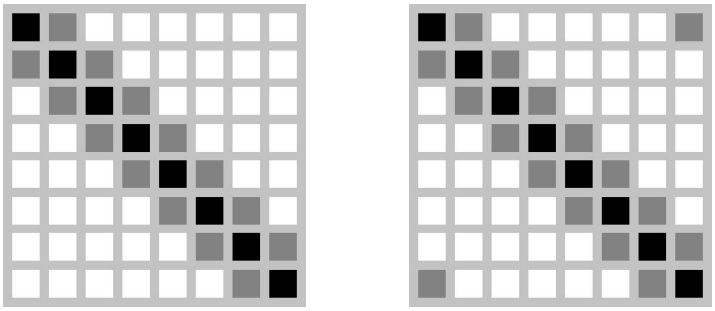

Figure 3.1: Matrix scheme for finite difference representation of the second derivative for $N_f = 1$ on a one-dimensional equidistant grid with N_g=8 grid points. On the left side, finite boundary conditions are depicted, assuming that any function $f(x)$ vanishes outside the super cell. On the right hand side, a matrix with periodic boundary conditions is depicted. The matrix representation in general is very sparse, i.e. the ratio of nonzero entries is $\frac{(2N_f+1)}{N_g}$ in the one-dimensional case.

3.2 Error estimate

Again the function represented on the grid is expanded into the Taylor polynomial. This time two orders more then requested to set up the matrix are taken into account. This gives an estimate for the error of the finite difference approach towards the second derivative:

$$f(x_i - h) \overset{\text{Taylor}}{=} f(x_i) - hf'(x_i) + \frac{h^2}{2}f''(x_i) - \frac{h^3}{6}f^{(3)}(x_i) + \frac{h^4}{24}f^{(4)}(x_i) + \mathcal{O}(h^5) \quad (3.7)$$

$$f(x_i + h) \overset{\text{Taylor}}{=} f(x_i) + hf'(x_i) + \frac{h^2}{2}f''(x_i) + \frac{h^3}{6}f^{(3)}(x_i) + \frac{h^4}{24}f^{(4)}(x_i) + \mathcal{O}(h^5) \quad (3.8)$$

$$f''(x_i) \approx \frac{1}{h^2}\,[1, -2, 1] \cdot \begin{bmatrix} f(x_i - h) \\ f(x_i) \\ f(x_i + h) \end{bmatrix} - \frac{h^2}{12}f^{(4)}(x_i) \quad (3.9)$$

Obviously the error in the second derivative enters as h^2. It can be shown that for $N_f > 0$ the error enters with h^{2N_f} multiplied by the $(2\,N_f{+}2)$-th derivative and an exponentially decreasing coefficient. Essentially, there are two ways to improve the quality of these derivatives. On one hand, the grid spacing h can be decreased which leads to an enormous increase of the computational costs. The other possibility is employing a higher order finite difference formula.

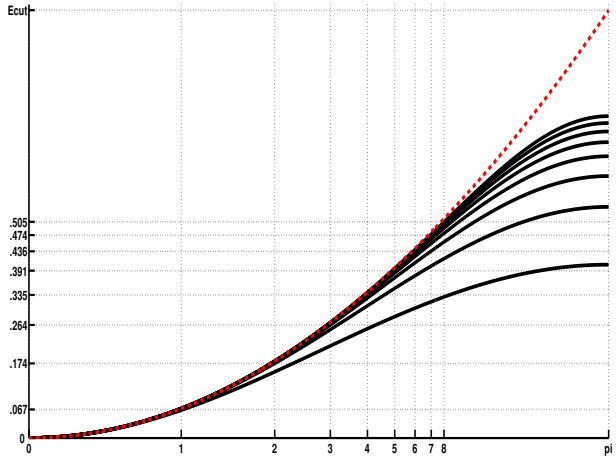

Figure 3.2: Error estimate of the finite-difference approximation for the second derivative applied to plane waves. Since $\mathbf{e}^{\mathrm{i}kx}$ is an eigenstates of the derivative operator, its second derivative is known analytically. For the allowed k-values in $[0, \frac{\pi}{h}]$, the FD-approximated 2nd derivative has been evaluated at the orders 2 to 16. The dispersion relation matches the exact derivative quite well as long as the k values stay below a certain fraction of the nominal cutoff wave vector $\frac{\pi}{h}$. The lowest black curve corresponds to the lowest order FD approximation (2nd order). A higher order finite difference approximation exploits the cutoff energy more efficiently. The vertical lines indicate a deviation of the derivative value of 1% and the horizontal lines the corresponding cutoff energy.

Figure 3.2 shows the dispersion relation of a plane wave where the kinetic energy is computed with finite difference approximations of various orders and analytically for comparison. It can be seen that the 2nd derivative deviates more from the analytical solution $\frac{1}{2}k^2$ for low order finite difference sets (lower curves). This means that the FD approximation is only accurate up to a certain fraction of the nominal cutoff energy $\frac{1}{2}\left(\frac{\pi}{h}\right)^2$. A very efficient way to reduce this error is by increasing the number of finite difference neighbors such that a larger fraction of the nominal cutoff energy can be exploited.

3.3 Lagrange interpolation

The Taylor expansion technique and so the central finite difference formula is equivalent with Lagrange interpolation: a polynomial $Q(x)$ of degree $2\,N_f$ is fitted such that it matches the values f_i at the grid points x_i perfectly i.e. $Q(x_i) = f_i$ for all $i \in [-N_f, N_f]$. Since a polynomial of degree m has exactly $m{+}1$ degrees of freedom, we have to fit it to exactly $2\,N_f{+}1$ pairs of point and value (x_i, f_i). To keep it symmetric we choose one central point x_0 and N_f neighboring points to each side i.e. $x_{-N_f}, x_{-N_f+1}, ..., x_0, ...x_{N_f-1}, x_{N_f}$. The generic solution for the Lagrange interpolated polynomial centered around x_0 reads

$$Q(x) = \sum_i \; f_i \prod_{k \neq i} \frac{x - x_k}{x_i - x_k} = \sum_i \; f_i \; c_i^{(0)}(x) \tag{3.10}$$

(all indices in $\sum$ or $\prod$ run from $-N_f$ to N_f). The expansion coefficients for the interpolated function are thus given by

$$c_i^{(0)}(x) = \prod_{k \neq i} \frac{x - x_k}{x_i - x_k} \tag{3.11}$$

So the first derivative of the polynomial reads

$$Q'(x) = \sum_i \; f_i \; \frac{\partial}{\partial x} c_i^{(0)}(x) = \sum_i \; f_i \; c_i^{(1)}(x) \tag{3.12}$$

$$c_i^{(1)}(x) = \sum_{j \neq i} \frac{1}{x_i - x_j} \prod_{k \neq i,j} \frac{x - x_k}{x_i - x_k} \tag{3.13}$$

and the second derivative

$$Q''(x) = \sum_i \; f_i \; \frac{\partial^2}{\partial x^2} c_i^{(0)}(x) = \sum_i \; f_i \; c_i^{(2)}(x) \tag{3.14}$$

$$c_i^{(2)}(x) = \sum_{j \neq i} \frac{1}{x_i - x_j} \sum_{l \neq i,j} \frac{1}{x_i - x_l} \prod_{k \neq i,j,l} \frac{x - x_k}{x_i - x_k} \tag{3.15}$$

This yields a direct formula to compute high order central FD coefficients for the second derivative $c_i^{(2)}(x = 0)$ without inverting the Van-der-Monde matrix. On an equidistant grid, the difference in the denominator $x_j - x_k$ is an integer multiple of the grid spacing h and never zero because the case $k = j$ is explicitly excluded such that equation (3.15) can be simplified to

$$c_i^{(2)}(0) = \frac{1}{h^2} \sum_{j \neq i} \frac{1}{i - j} \sum_{l \neq i,j} \frac{1}{i - l} \prod_{k \neq i,j,l} \frac{k}{i - k} \tag{3.16}$$

The coefficents $c_i^{(2)}(0)\,h^2$ are displayed in Table 3.1 for N_f in $[1, 6]$.
The consistency of the finite difference approach with the Lagrange interpolation

technique is important because in later sections of this work, Lagrange interpolation will be applied to find values of a wave function in between two grid points. Figure 3.3 shows the effect of interpolation with a finite number of grid points onto sharp-featured functions. The interpolation operator $\hat{\mathcal{I}}$ applies Lagrangian interpolation to find the translate from a coarse grid to a finer grid. This operator shows a sparse matrix representation if the order of interpolation is finite. The operators matrix representation does not even require an explicit storage if the coarse grid spacing, h_{coarse}, is an integer multiple of the fine grid spacing, h_{fine}. The 'inverse' operation $\hat{\mathcal{I}}^{\dagger}$ reverts the translation from a finer grid to the coarse grid. However, this operator may not be called the inverse of $\hat{\mathcal{I}}$ because both matrices are not square. The consequent execution of both operations, $\hat{\mathcal{I}}^{\dagger}\hat{\mathcal{I}}$, will be the unity operation and let the function on the coarse grid unchanged as long as the order of interpolation is equal to the number of grid points. Any truncated formula with $2\,N_{\mathrm{itp}} < N_{\mathrm{g}}$ will introduce an error to sharp features of the function as depicted in Figure 3.3.

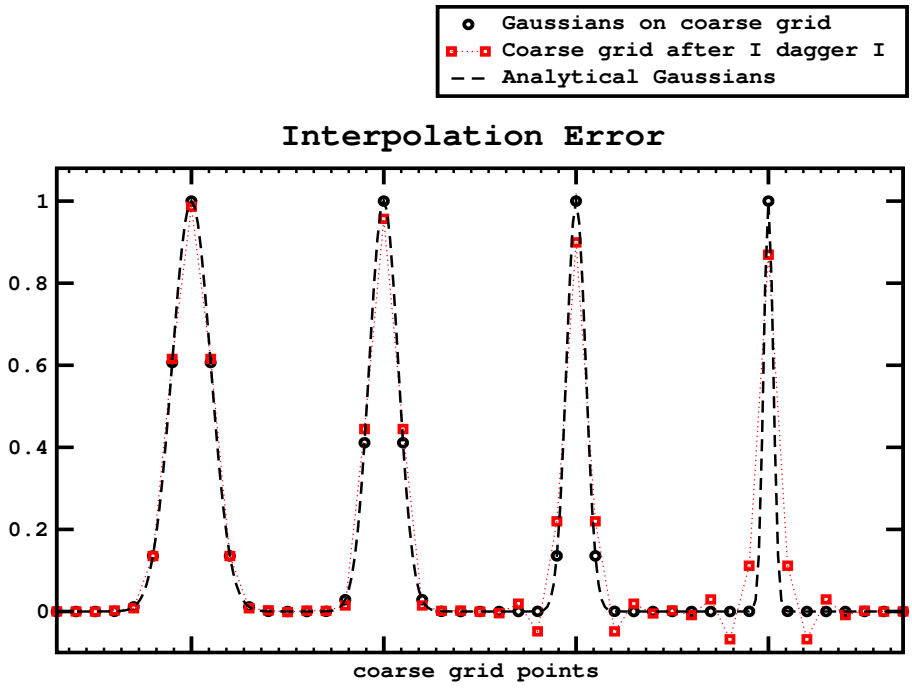

Figure 3.3: Interpolation technique error estimate. Gaussians of different width on a coarse grid after their treatment with an $\mathcal{I}^{\dagger}\mathcal{I}$ operation, interpolating these onto a $3\times$ finer grid and back using $2\,N_{\mathrm{itp}} = 10$ values to fit the polynomials. Obviously a sharper peak causes stronger deviations from the original function. This means that $\mathcal{I}^{\dagger}\mathcal{I}$ resembles the unity operator for slowly varying functions but introduces errors for high frequencies.

3.4 The grid choice

The different scales of potential - very deep in the core region but shallow in the interstitial region - lead to a difficulty representing potentials and wave functions on a grid with equal grid spacing in the entire space. The $\frac{1}{r}$-singularity of the core potentials can not be treated properly on a grid with constant grid spacing since its structure has no proper scale and thus needs a very high basis density (grid points or plane waves) to resolve it in a sufficiently accurate manner. The deep potential corresponds to a high kinetic energy and so all electronic wave functions will oscillate in high frequency modes in the vicinity of the nuclei. The maximum frequency to be represented on a equidistant grid with a grid spacing of h is $k_{\max} = \frac{\pi}{h}$. This is called sampling theorem and where $k_{\max}$ denotes the Nykvist-frequency. The theoretical maximum of kinetic energy $\frac{\pi^2}{2h^2}$ will further on be called 'nominal cutoff energy'. In order to represent highly oscillating functions the grid spacing h must be decreased. The increasing costs ($\propto \frac{1}{h^3}$) for computational resources attached to this have been mentioned before. This motivates the usage of pseudopotentials (see Chapter 4). Alternatively the grid spacing can adopt to the local potential which leads to a non-uniform grid and entails difficulties of another kind (see Chapter 3.5).

3.5 Non-uniform grids

Non-uniformity of the grid implies that the spacing between grid points differs and therefore is a function of the grid point index. In principle one can determine the coefficients for the finite difference representation by the same technique as outlined above but the coefficients as well become functions of the grid index. This is quite easy on a one-dimensional grid but three spacial dimensions require mathematical construct like non-diagonal Riemann tensors. This in general includes so called *adaptive coordinates* [18] and *finite element* methods [19]. Another consequence is that even derivatives do not result in symmetric coefficients any more. The matrix representation is neither symmetric nor hermitian any longer. Diagonalizing such a non-symmetric matrix (e.g. second derivative on a non-uniform one-dimensional grid with exponentially growing grid spacing) produces as expected *only real* eigenvalues. This shows that physical significance of the observable has been kept, but simply the underlying mathematics has changed.
The advantage of a non-uniform grid is the possibility of increasing the grid point density in the vicinity of atomic cores. This enables all-electron calculations where fast oscillating core states and slowly varying valence wave functions are represented on the same grid. Also in the case of a widely extended vacuum region inside the super cell, this could help to save resources such as computational time and memory. Although it does produce a computational overhead: the least of which is determining and setting up the grid. This costs time once in the beginning of a computation of the electronic structure plus some additional memory but the major factor is the determination and storage of the spatially dependent operators and their application

to wave functions in each iterative cycle. Parallelization of an adaptive coordinate grid in real space requires that a domain decomposition has to be chosen in a sophisticated way to provide an effective load balance.
Despite the advantages of nonuniform grids, the advantages of simple formulas and easy implementations on a uniform grid are the striking reasons to use a constant grid spacing in this work.

4 Pseudopotentials

Density functional calculations aim to simulate the chemical environment inside a finite volume. For the chemical binding process the valence states are the most important while core states inside closed shells contribute fairly little and can so be considered inert. This justifies the *frozen core* approximation where the relaxed core states and the interaction of valence states with core states are integrated out and only the screened core potential becomes visible. This approximation has proven to be valid for most chemical environments. The full potential and the all-electron valence wave function are hardly representable with a reasonably small number of grid points or plane waves. Neither the singularity of the full potential at the core position can be resolved nor the rapid oscillations of the valence functions in the vicinity of the cores. For this reason a *pseudization* is performed: An augmentation sphere centered around the atom is introduced. Inside the sphere the strong core potential is replaced by weak and smooth pseudo potential. The valence wave function are replaced by a pseudo wave function with just the same logarithmic derivative at the augmentation radius as the all electron wave function [7]. The pseudo wave function is supposed to be very smooth (no high frequency components) and contain no nodes but it has to fulfill the radial Kohn-Sham equation containing the smooth pseudized potential. Furthermore the norm of the pseudized wave function has to be preserved. The advantage of this technique is the removal of the divergent core potential and the fast oscillations of the valence wave function due to it. The radial Kohn-Sham equation is the radial single particle Schrödinger equation with a potential that depends on the total electron density.

$$\left[-\frac{1}{2}\frac{\mathrm{d}^2}{\mathrm{d}r^2} + \frac{\ell(\ell+1)}{2r^2} + V\{\varrho(r)\}(r)\right] rR_{n\ell}(r) = \epsilon_{n\ell}\ rR_{n\ell}(r) \tag{4.1}$$

$$\varrho_{\mathrm{new}}(r) = \sum_{n\ell}\ f_{n\ell}\ R_{n\ell}(r) \tag{4.2}$$

where $f_{n\ell}$ are the occupation numbers for the orbitals with principle quantum number n and angular momentum quantum number ℓ. This equation is to be solved self-consistently i.e. the new density $\varrho_{\mathrm{new}}(r)$ that is gained from the radial wave functions has to coincide with the density $\varrho(r)$ that has been used to construct the potential $V\{\varrho(r)\}(r)$.

4.1 Kleinman-Bylander norm-conserving pseudopotentials

Analogous to the Schrödinger equation the effective potential from the angular momentum part in the radial Kohn-Sham equation (4.1) depends on the quantum number ℓ. So the pseudopotential differs with respect to the ℓ-channel. Kleinman and Bylander [5] suggested a separable form for the pseudopotential which splits into a nonlocal part and a local part.

$$\hat{V}_{\text{pseudo}}(r) = V_{\text{loc}}(r) + \sum_{\ell} V_{\text{nonloc},\ell}\ \hat{P}_{\ell}(r) \tag{4.3}$$

The local part contains the pseudized core potential and contributions from the interactions with the electron density. The nonlocal part consists of coefficients $V_{\text{nl},\ell}$ which are different for each particular ℓ-channel whereas the spatial dependency is included in the projectors $\hat{P}_{\ell}(r)$. These enable the specific treatment of **s**, **p** and **d** states such that the nonlocal pseudopotential acts onto the proper part of the wave function. Therefore the projection operation is performed inside the augmentation sphere with radius r_{cut} centered around the ion core. The local pseudopotential and the radial part of the projector functions are depicted in Figure 4.1 for hydrogen, carbon, nitrogen and oxygen. Here the shape of the Coulomb potential $-\frac{1}{r}$ is approximated by a smooth linear combination of two error functions divided by r. $\mathcal{Z}^{(s)}$ is the core charge of the respective species minus the number of core electrons, so the (positive) ionic charge.

$$V_{\text{loc.}}^{(s)}(r - \mathbf{R}^{(a)}) = -\mathcal{Z}^{(s)} \cdot \left[C_1^{(s)} \frac{\text{erf}(\sqrt{\alpha_1^{(s)}} r)}{r} + C_2^{(s)} \frac{\text{erf}(\sqrt{\alpha_2^{(s)}} r)}{r} \right] \tag{4.4}$$

In the limit of $r \to \infty$ the approximate function $\frac{\text{erf}(\sqrt{\alpha} r)}{r}$ approximates $\frac{1}{r}$ quite well. Already at $r = 2.0/\sqrt{\alpha}$ their values deviate only by 0.5%. The values for $C_{1,2}$ and $\alpha_{1,2}$ have to be determined in the generation of the pseudopotential such that the local potential is converged to the all electron potential within the cutoff radius, r_{cut}. The long range Coulomb potential far away from the core must be exactly $-\frac{\mathcal{Z}^{(s)}}{r}$. This leads to the constraint

$$C_1^{(s)} + C_2^{(s)} = 1.0. \tag{4.5}$$

Assume, that $\alpha_1^{(s)} > \alpha_2^{(s)}$. Then the contributions to the local pseudopotential can be divided into a localized 'hard' part and a smooth part (the species index (s) is suppressed in the following).

$$\begin{aligned} V_{\text{loc.}}(r) &= -\frac{\mathcal{Z}}{r} \left[C_1 \text{erf}(\sqrt{\alpha_1} r) + C_2 \text{erf}(\sqrt{\alpha_2} r) \right] \\ &= -\frac{\mathcal{Z}}{r} C_1 \left[\text{erf}(\sqrt{\alpha_1} r) - \text{erf}(\sqrt{\alpha_2} r) \right] \qquad \text{hard part} \\ &\quad -\frac{\mathcal{Z}}{r} \left[C_2 - C_1 \right] \text{erf}(\sqrt{\alpha_2} r) \qquad \text{smooth part} \end{aligned} \tag{4.6}$$

The hard part and the projectors for the nonlocal part cannot be represented accurately on the coarse grids. Therefore the double-grid technique is applied to it. A second grid is introduced with a smaller grid spacing than the coarse grid but only localized within the sphere. The projectors can be considered as sums of *dyads* i.e.

$$\hat{P}_\ell = \sum_m |p_{\ell m}\rangle \langle p_{\ell m}| \tag{4.7}$$

The notation $\langle .| .\rangle$ stands for *bra* and *ket* meaning that an integration of the product of both functions is performed in real space. These integrals are evaluated numerically on a the fine grid, only inside the augmentation sphere (see Chapter 5.6 for details of the double-grid technique).

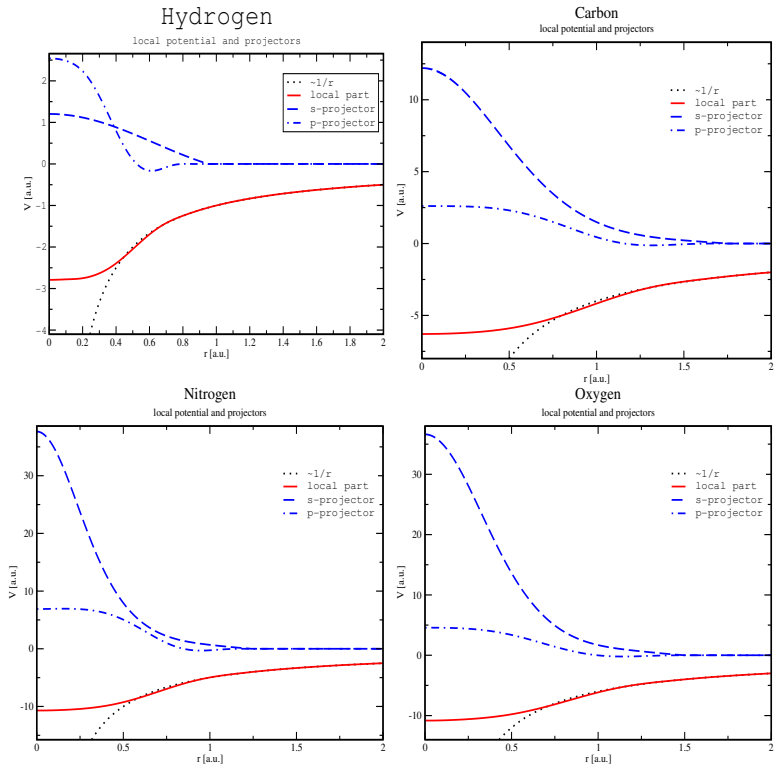

Figure 4.1: Local and non-local part of the pseudopotentials. Plotted are the local pseudopotential as a function of the radius and the $1/r$-ion potential for comparison. Furthermore the shape of the **s** and **p** projectors is depicted in dotted lines.

4.2 Convergence

Employing pseudopotentials in a calculation always requires convergence tests to ensure its accuracy. This means that a quantity such as the total energy here, is calculated at different grid spacings to determine the maximum grid spacing that

produces accurate results and, to get an error estimate for the calculated quantity. The results of convergence tests of the total energy of an isolated atom are shown in Figure 4.2.

It can be read off that around $E_{\text{cut}} = 70\,\text{Ry}$ the total energy for H and C differs only slightly from its final value at 177 Ry which means a quite accurate representation of these species. Nevertheless nitrogen and oxygen still lower their total energy considerably when increasing the 'cutoff energy' above 70 Ry. The fact that the total energy decreases monotonously with an increasing number of basis element (grid points in this particular case) points out the variational nature of this approach towards the ground state. A more precise description always gets closer to the real (continuously defined) ground state wave functions because it gives access to a larger number of degrees of freedom.
The special case of nitrogen shows here an unpredictable behavior of the total energy for small cutoff energies. This can be explained by a quite hard (rapidly varying) local part of the pseudopotential that cannot be displayed with sufficient accuracy on a grid with a low cutoff energy. The pseudo wave functions are not orthogonalized to the core states, so it is not guaranteed that they will fall into a lower, unphysical state. These states are called *ghost states* and are the unwanted side-effect of the pseudization. Apparently this appears mainly at very large grid spacings.

Density-functional calculations are often used to find differences of the total energy e.g. a reaction enthalpy or barrier. The systematic error on the total energy is strongly related to the level of convergence when pseudopotentials are used. Fortunately the error on energy differences can be much smaller due to error cancellation.

4.3 New generation pseudopotentials

In order to speed up *ab inito* calculations a pseudopotential technique is required which gives the same accuracy at lower costs i.e. less plane waves or larger grid spacings. Vanderbuilt [20] discovered that loosening the norm-conserving constraint gives way to much smoother pseudo wave functions. The physics are maintained by introducing *augmentation charges* that countervail the charge difference.
Blöchl [21] constructed an interface to an all-electron method. The *projector augmented wave*(PAW) method is quite promising to be used with small cutoff energies. Though making use of the frozen core approximation it enables to retrieve the all-electron energies and all-electron wave functions and densities. An extension, the *gauge including projector augmented wave* (GIPAW), even provides shielding tensors. These help to understand the results of nuclear magnetic resonance spectroscopy (NMR) [22].

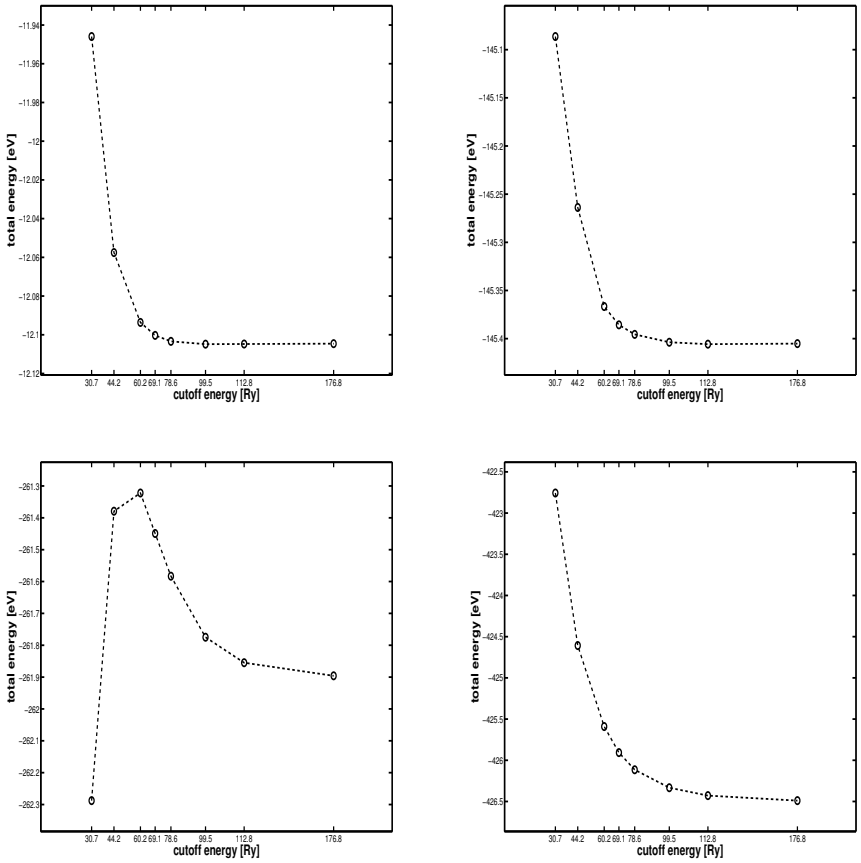

Figure 4.2: Convergence of the pseudopotentials. Plotted is the total energy against the 'cutoff energy' (compare Chapter 3.2) for one atom of hydrogen, carbon, nitrogen and oxygen, respectively. Each atom is calculated in a $5 \times 5 \times 5\,\text{Å}^3$ box with isolated boundary conditions. For a cutoff energy of 70 Ry, H and C are well converged whereas the total energy difference $E_{\text{tot}}(70\,\text{Ry}) - E_{\text{tot}}(\infty)$ for N and O is about one magnitude larger. $E_{\text{tot}}(\infty)$ has here been approximated by $E_{\text{tot}}(177\,\text{Ry})$. Nitrogen obviously requires a minimum cutoff energy of 60 Ry to ensure that no ghost states appear from the norm-conserving pseudopotential. Above 60 Ry, the behavior of the total energy is monotonous so that error cancellation can be expected.

5 Electronic structure calculation

Real-space techniques for density functional calculations of the electronic structure have a lot in common with those methods that have been developed in the last decades for density functional calculators using plane waves or other basis functions, despite the fact, that the equidistant real-space grid allow a simple and efficient parallelization of the unit cell. In the following, the parallelization will be kept in the background whereas the focus will be set to the essential steps of the determination of the electronic structure.

5.1 Self consistency scheme

Real-space methods make use of iterative solvers on various levels. Especially because of the vast numbers of grid points, direct methods and explicit matrix operators are disadvantageous for larger system sizes due to the enormous memory consumption. The highest level of iterative solvers for the determination of the electronic structure is the self-consistency iteration scheme introduced here. Its aim is to calculate the self-consistent density i.e. a density that causes an effective potential, thus an effective single-particle Hamiltonian whose eigenstates lead again to exactly the same density. This flowchart will give only a brief introduction to what kinds of calculations are preformed and which techniques are applied for this. The single steps of one cycle are explained further in the referenced chapters.

- Given a total density $n^{(k)}(\mathbf{r})$ in the k-th cycle we can evaluate the effective potential $V_{\text{eff}}(\mathbf{r})$ as the sum of the exchange-correlation potential (see Chapter 2.3), Hartree potential $V_{\text{H}}[n](\mathbf{r})$(see Chapter 5.4), ion potentials $V_{\text{ions}}(\mathbf{r})$ and external potential $V_{\text{ext}}(\mathbf{r})$, if e.g. an electrical field is present.

- The Kohn-Sham Hamiltonian is set up as $\hat{H}_{\text{KS}} = -\frac{1}{2}\Delta + V_{\text{eff}}(\mathbf{r})$, where the kinetic energy operator is approximated by a higher order finite difference formula replacing the second spatial derivatives.

- The lowest N_{bands} eigenvalues $\epsilon_{\text{KS}}^{(i)}$ and eigenstates $\psi_{\text{KS}}^{(i)}(\mathbf{r})$ of the Hamiltonian are calculated (see Chapter 5.2). N_{bands} also includes some unoccupied states.

- The occupation numbers f_i are computed according to the Fermi-Dirac distribution, where E_{F} is to be determined before. $f^{(i)} = \frac{1}{\mathbf{e}^{(\epsilon^{(i)}-E_{\text{F}})/k_{\text{B}}T}+1}$ (see Chapter 5.9).

- A new density is created from the wave functions of the occupied bands/molecular orbitals $n^{(k)}_{\text{new}}(\mathbf{r}) = \sum_i f^{(i)} |\psi^{(i)}(\mathbf{r})|^2$.

- The next density $n^{(k+1)}(\mathbf{r})$ is combined from $n^{(k)}_{\text{new}}(\mathbf{r})$ and $n^{(k)}(\mathbf{r})$ by density mixing (see Chapter 5.7).

This algorithm needs an initial density guess $n^{\text{init}}(\mathbf{r})$. A very simple choice is to assume spherical gaussian distributions around the ion cores where the charge of each cloud corresponds to the number of valence electrons of that particular atom.

The self-consistency is reached when the density does not change more than a certain threshold. The change of the total density is measured via a spatial average over the square deviation of the new density from the old i.e.

$$\sigma^{(k)}_{n(\mathbf{r})} = \left[\frac{1}{V} \int_V \mathrm{d}^3\,\mathbf{r} \left(n^{(k)}_{\text{new}}(\mathbf{r}) - n^{(k)}(\mathbf{r}) \right)^2 \right]^{\frac{1}{2}} \tag{5.1}$$

Another possible way to check for convergence is the change of the total energy $\Delta E^{(k)}_{\text{total}} = E^{(k)}_{\text{total}} - E^{(k-1)}_{\text{total}}$.

5.2 The eigenvalue solver

The kinetic energy functional $T\{n(\mathbf{r})\}$ can only be evaluated via auxiliary wave functions, the Kohn-Sham states. The lowest N_{bands} eigenstates of the Kohn-Sham Hamiltonian are required. Given the Hamiltonian matrix explicitly, a common numerical solver can produce all eigenvalues and eigenvectors within a number of operations that scales cubically with the matrix size (proportional to N^3_{tot}, where N_{tot} is the total number of grid points). However, for an Hamiltonian that is not given explicitly but whose action on a state vector is well defined, eigenvalues and eigenstates can be be found employing iterative algorithms. Especially the fact is exploited that the number of requested eigenvectors N_{bands} is small against the dimension N_{tot}. Several methods apply for this task. Krylov-subspace methods can compute the lowest (or highest) eigenvalue and the corresponding eigenvector from a given action of a hermitian operator with the Lanczos algorithm. However some higher (in energy) eigenvalues are needed. The class of *generalized minimal residual* methods has turned out to work well.

The eigenstates of the Kohn-Sham Hamiltonian are found by applying a steepest descent (SD) method to minimize their residual. The eigenvalue equation to be solved is

$$\hat{H}_k \ |\psi_{nk}\rangle - \epsilon_{nk} \, |\psi_{nk}\rangle = 0 \tag{5.2}$$

where k labels the different Bloch-states and n is the band index. Therefore the residual norm is minimized. The residual is defined as

$$\left[\hat{H} - \epsilon^{(m)}\right] \left|\psi^{(m)}\right\rangle = \left|r^{(m)}\right\rangle \tag{5.3}$$

where $\epsilon^{(m)}$ is set to the expectancy value of the Hamiltonian $\left\langle\psi^{(m)}\right| \hat{H} \left|\psi^{(m)}\right\rangle$. The residual norm $R^{(m)}$ is defined as

$$R^{(m)} = \left\langle \psi^{(m)}\right| r^{(m)}\left\rangle = \left\langle\psi^{(m)}\right| \left[\hat{H} - \epsilon^{(m)}\right] \left|\psi^{(m)}\right\rangle \tag{5.4}$$

is assumed to have a quadratic minimum around 0. Consequently its gradient with respect to the approximate eigenstate is

$$\left|\nabla R^{(m)}\right\rangle = \frac{\delta R^{(m)}}{\delta \left\langle\psi^{(m)}\right|} = \left[\hat{H} - \epsilon^{(m)}\right] \left|\psi^{(m)}\right\rangle . \tag{5.5}$$

The steepest descent (SD) is an iterative algorithm finding the minimum of the scalar $r^{(m)}$ performing a line search in the direction opposite to the gradient.

$$\left|\psi^{(m+1)}\right\rangle = \left|\psi^{(m)}\right\rangle - \lambda \left|\nabla R^{(m)}\right\rangle \tag{5.6}$$

$$\lambda = \frac{\left\langle \nabla R^{(m)}\right| \nabla R^{(m)}\left\rangle\right.}{\left\langle\nabla R^{(m)}\right| \hat{H} - \epsilon^{(m)} \left|\nabla R^{(m)}\right\rangle}. \tag{5.7}$$

A more sophisticated scheme is called *conjugate gradients* (CG). There the search direction is determined to be a linear combination of the new gradient and previous search directions i.e. a memory about previous steps is set up. Of course the first step of CG is equivalent to the steepest descent since there is no previous step. In fact it has turned out that a few CG steps are enough to get sufficiently accurate eigenvectors. The subspace diagonalization method (Chapter 5.8) helps to suppress the errors introduced by not converging the eigenstates fully.
The eigenstates of the Hamiltonian being a hermitian operator are orthogonal to each other. The steepest descent algorithm described above will converge an approximate eigenstate to its nearest exact eigenstate of the Hamiltonian. In the beginning of a calculations, starting from initial guess vectors, one has to ensure that the first wave function corresponds to the energetically lowest state. Any state with a higher energy is constraint to be orthogonal to the lower ones so when SD or CG are applied the state and the search direction have to be orthogonalized to the previous states by Schmidt-orthonormalization. Otherwise errors could affect, that two states approach each other and converge to the same eigenvector.

$$\left|\phi_{i,\mathrm{orthog}}\right\rangle = \left|\phi_i\right\rangle - \sum_{j<i} \left|\psi_j\right\rangle \left\langle\psi_j\right| \left.\phi_i\right\rangle \tag{5.8}$$

$$\left|\phi_{i,\mathrm{orthon}}\right\rangle = \frac{\left|\phi_{i,\mathrm{orthog}}\right\rangle}{\sqrt{\left\langle \phi_{i,\mathrm{orthog}}\right| \left.\phi_{i,\mathrm{orthog}}\right\rangle}} \tag{5.9}$$

In addition to the conjugate gradients methods, preconditioning is applied to the search direction in order to speedup the convergence. The preconditioner $\hat{K}$ applied onto the discretized search direction ψ_i is a broadening operator, that relates neighboring grid points. A simple one-dimensional broadening could be described as follows.

$$\hat{K}\,|\psi\rangle : \qquad \sum_j K_{ij}\psi_j = \frac{1}{4}\psi_{i-1} + \frac{1}{2}\psi_i + \frac{1}{4}\psi_{i+1}. \tag{5.10}$$

5.3 Boundary conditions

The great advantage of real-space representation of wave functions and densities is the possibility to arbitrarily combine periodic and finite boundary conditions (BCs). Out of this, eight ($= 2^3$) cases can be constructed in three dimensions. However, only four of them are unique with respect to spatial rotations.

periodic BCs	finite BCs	Example	Equivalence
none	3	molecules, clusters	000
1	2	wires, nanotubes	100 010 001
2	1	surfaces, films	011 101 110
3	none	bulk	111

The implementation of these four cases is quite simple, regarding the fact, that the decomposition of the real space unit cell into calculation domains for parallelization requires data exchange at the boundaries of each domain. This will be explained further in Chapter 6.1. Periodic boundary conditions will therefore enforce data exchange also across the cell boundaries, whereas it is assumed for insolated BCs that the values of the wave functions outside of the cell are exactly zero.
Apart from these straightforward cases, realizations of very special boundary conditions can be set. The implementation of the real-space finite-difference method on a parallelepiped-shaped unit cell (non-orthogonal base vectors) is in principle feasible but the simplicity of the finite-difference second derivative stencil will be lost. Much simpler and faster is still the rectangular unit cell. Nevertheless some crystal structure (e.g. hexagonal) require a larger super cell than their unit cell when computed with a rectangular cell shape. The uneven boundary conditions enable to exploit these symmetries and keep the cell small though using a rectangular calculation domain. Figure 5.1 shows the example of uneven boundaries on a graphene sheet. The next unit cell in e.g. y-direction is shifted in x-direction. Usually the smallest rectangular cell would contain 4 atoms but the shift reproduces the rhomboid geometry of the lattice and so enables a calculation with only 2 atoms contained in the cell. Instead of taking a shift of half the cell length, one could think of any fraction s as shift and so compute a shear modulus. Certain values for this fraction are advantageous, i.e. if the shift s is an integer multiple of the grid spacing h, because then, data can be sent across the boundary without additional interpolation.

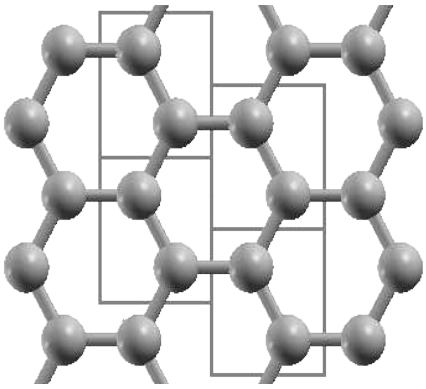

Figure 5.1: Uneven boundary conditions. The shift enables a calculation of a graphene sheet with two instead of four atoms per unit cell.

A very special case is the twist boundary condition. The case of periodicity in one direction and a chiral symmetry along that axis can be represented and calculated with a reasonably small super cell in axis direction. This is very useful for calculating e.g. the electronic structure of certain carbon nanotubes (CNTs). Armchair-wrapped (n, n) or zigzag-wrapped $(n, 0)$ CNTs show high translational symmetry and can so be represented in a short super cell (4.62 Å for armchair and 2.67 Å for zigzag). For other (n, m)-wrapped nanotubes $[n > m > 0]$ the symmetry is lower and so a very long super cell is required in principle. Twist boundary conditions are able to exploit their chiral symmetry, though. Figure 5.2 shows a $(11, 5)$ CNT. At the boundaries a *screw operator* is applied in the plane perpendicular to the axis. This operator is based on interpolation between the grid points according to the Lagrange interpolation technique introduced in Chapter 3.3. Applications for finding the torsion modulus of a system with one-dimensional periodicity can be realized by computing the total energy dependence of the twist angle.

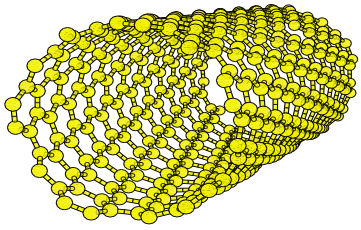

Figure 5.2: Twist boundary conditions. A $(11, 5)$ carbon nanotube may be calculated with a cell of 1/8th of its periodicity in axis direction using a twist boundary condition.

5.4 The Hartree potential

The classical electrostatic repulsion of the electrons contributes to the effective single-particle potential in the form of the Hartree potential term $V_{\mathrm{H}}\{n\}(\mathbf{r})$. From classical electrodynamics we know that a point charge q at the position $\mathbf{r}'$ creates an electrostatic potential according to

$$v_q(\mathbf{r}) = \frac{q}{|\mathbf{r} - \mathbf{r}'|}. \tag{5.11}$$

The superposition principle tells that the potential of a charge distribution is

$$V_{\mathrm{H}}\{n\}(\mathbf{r}) = \int_V \mathrm{d}^3\mathbf{r}' \frac{n(\mathbf{r}')}{|\mathbf{r} - \mathbf{r}'|}. \tag{5.12}$$

The same is expressed by the Poisson equation

$$\Delta_{\mathbf{r}} V_{\mathrm{H}}\{n\}(\mathbf{r}) = -4\pi n(\mathbf{r}). \tag{5.13}$$

These two equivalent equations indicate two different possibilities of calculating the Hartree potential in real-space. The first one is the direct method, using the Green-function of the Poisson equation

$$g(\mathbf{r}, \mathbf{r}') = \frac{1}{|\mathbf{r} - \mathbf{r}'|}. \tag{5.14}$$

On a grid, this operator becomes

$$g_{i,j} = \frac{1}{|\mathbf{r}_i - \mathbf{r}_j|} \tag{5.15}$$

for finite boundary conditions. However, $g_{i,j}$ is a full matrix i.e. relating each grid point directly to any other. Even though this operator is simple to determine, the action of this operator scales as $\propto N_{\mathrm{tot}}^2$, where N_{tot} denotes the total number of grid points, $N_{\mathrm{tot}} = N_x N_y N_z$.
The alternative opportunity is to start at equation (5.13) and express the Laplacian via real-space finite-difference formula (Chapter 3) which results in a large, inhomogeneous set of linear equations. The Laplacian itself then is a sparse operator again. This promotes the use of iterative scheme for solving this. The conjugate gradient (CG) method is one opportunity. Alternatives are the multigrid methods [9], some of them even employ the *Mehrstellen* formula [9].

The residual to be minimized in the CG algorithm at the m-th step is defined as

$$R_m = \langle r_m | \, r_m \rangle \, ; \qquad |r_m\rangle = |\Delta V_{\mathrm{H},m}\rangle - (-4\pi)\,|n\rangle \tag{5.16}$$

The conjugate gradient scheme is explained in detail in Chapter A.1. For the electrostatic problem a preconditioning technique can be applied. Useful preconditioning works with an approximation of the inverse of the operator at hand [23]. In this particular case the inverse is known to be the Green-function $\frac{1}{|\mathbf{r}-\mathbf{r}'|}$ but it is not sparse, as pointed out before. A sparse approximate of that is a broadening operator e.g. gaussian broadening as the preconditioner $\hat{K}$:

$$\hat{K}(\mathbf{r},\mathbf{r}') = \frac{\mathbf{e}^{-\frac{1}{2}(\mathbf{r}-\mathbf{r}')^2/\sigma^2}}{(2\pi\sigma^2)^{\frac{3}{2}}} \tag{5.17}$$

Due to the rapidly decaying exponential function it may be truncated to a finite range instead of the long ranged $\frac{1}{r}$ function. Simultaneously it is taken care of the singularity at $\mathbf{r} = \mathbf{r}'$, which requires a special treatment otherwise.

The problem to overcome is the stalling process due to the long wavelength error which is reduced only very slowly with a finite difference formula truncated to some N_f grid points. Preconditioning is one way to increase the convergence speed of the residual minimization. New solutions towards this employ the *multigrid technique* that has been mentioned above.
Any number of finite boundary conditions (see Chapter 5.3) requires a special treatment when determining the Hartree potential. Outside of the super cell the the charge density $n(\mathbf{r}_{\text{outside}}) = 0$ vanishes. The electrostatic potential for a charge distribution localized inside a certain region can be approximated by an expansion into cartesian multipole moments;

$$V_{\text{H,outside}}(\mathbf{r}) = \frac{q}{r} + \frac{\mathbf{D}\cdot\mathbf{r}}{r^3} + \frac{\mathbf{r}\cdot Q\cdot\mathbf{r}}{r^5} + \mathcal{O}(\frac{1}{r^7}) \tag{5.18}$$

where q is the monopole charge, $\mathbf{D}$ the dipole vector and Q the quadrupole tensor. By construction, $\Delta V_{\text{H,outside}}(\mathbf{r})$ vanishes in the entire space outside the cell.
Thus the Hartree potential is subjected to the constraint that the potential in the vacuum is given by $V_{\text{H,outside}}(\mathbf{r})$ at the cell boundaries with finite boundary conditions. This enters the differential equation on the right hand side. The equation determining the Hartree potential then is

$$\Delta V_{\text{H}}(\mathbf{r}) = -4\pi n(\mathbf{r}) - \Delta V_{\text{H,outside}}(\mathbf{r}) \tag{5.19}$$

so that the usage of the conjugate gradient method for the discretized inhomogeneous system of equations is not affected at all. The determination of the Hartree potential outside the cell $V_{\text{H,outside}}(\mathbf{r})$ via multipole moments is described in Chapter 5.5.
For systems with periodicity in all spatial directions the Hartree energy is, in principle, unconstraint but the usage of Bachelet, Hamann, Schlüter (BHS) pseudopotentials [6] requires that

$$\int_V \mathrm{d}^3\mathbf{r}\ V_{\text{H}}(\mathbf{r}) = 0 \tag{5.20}$$

5.5 Fuzzy cell decomposition

The constraint on the Hartree potentials outside of the finite boundary conditions is calculated by a multipole expansion of the charge distribution inside the cell. The cell borders are usually not far away from non-vanishing densities. Therefore the potential needs to be expanded to a very high order to keep the errors at the cell borders low if the single-centered multipole expansion is used indicated in equation (5.18). The multi-centered expansion has the advantage that it does not require a high expansion order to reduce the errors significantly since most of the centers are far from the vacuum. The calculation domain is divided into so called *fuzzy cells* (FCs) such that each FC contributes to the potential but with only low order components (usually up to the quadrupole moment). The fuzzy cell is a spatial region centered around the atomic positions where the multipole moments of the density are integrated. In order to avoid fluctuating charges to cause a equally strong fluctuating moment, the fuzzyness is introduced by smearing out the borders of these cells. Any point in space thus belongs with a certain weight to any fuzzy cell whereas the major contribution falls to the closest center. Reducing the fuzzyness to 0 would yield the Voronoi-polyhedra (Wigner-Seitz-cell) around the atomic positions.

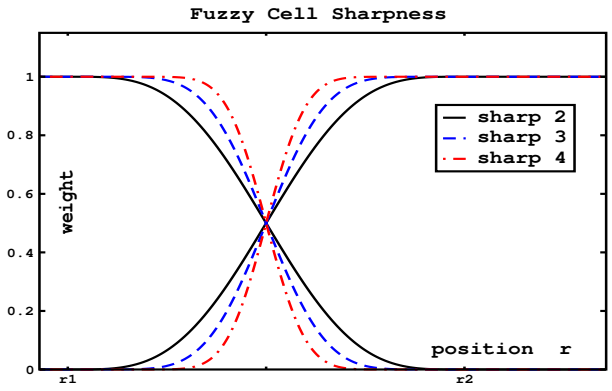

Figure 5.3: Fuzzy cell weights in one dimension for two atoms at $\mathbf{r}_1$ and $\mathbf{r}_2$. Different sharpness parameters can be applied according to the grid spacing. A small grid spacing allows high sharpness to be resolved in a smooth weight function.

The monopole moments of the expanded charge distribution could in principle give a rough estimate of the charge transfer between atoms. An example is hydrofluoric acid (HF). Calculating the self consistent density as an isolated molecule at the equilibrium distance of 0.72 Å, the fuzzy cells divide the super cell into equal parts whereas the separating plane in the middle becomes a smeared out region. However the two fuzzy cell weight functions are exact mirror images of each other. It can be observed that a charge of 1.9 e contribute to the fuzzy-cell monopole around hydrogen whereas the remaining 6.1 e of 8 shared valence electrons are in the flourine fuzzy cell. For the accuracy of the multipole expansion fuzzy cells of equal size may be good but

in order to get an estimate of the charge transfer in e.g. polar bonds (Bader-analysis) the fuzzy cell volume has to depend on the atomic species.

5.6 Double grid technique

The projectors of the nonlocal pseudopotentials introduced before (Chapter 4) are products of radial functions inside the augmentation sphere and spherical harmonics. Choosing a small cutoff radius r_{cut} affects that the radial projector functions show rapid changes for $r \in [0, r_{\text{cut}}]$. Especially the norm-conserving pseudopotential method produces quite 'hard' pseudopotentials for some first-row elements when a small r_{cut} is applied. Performing the scalar product of the wave function and the projector on the coarse grid produces very inaccurate results. Especially quantities as e.g. the total energy and forces fluctuate with respect to the atomic position with a period of the coarse grid spacing [10]. This unphysical behavior is crucial for the forces if these are employed for geometry optimization. A solution towards this is to perform the scalar product on a finer grid: Inside the augmentation sphere, the grid is refined by introducing additional grid points between those of the coarse grid. An integer refinement factor N_{refine} ensures that the grid points of the coarse grid are simultaneously elements of the fine grid. The grid spacing is then decreased by the refinement factor, $h_{\text{fine}} = h_{\text{coarse}}/N_{\text{refine}}$. Typically one uses 2 to 4 times more grid points per dimension on the fine grid. Throughout this work, the grid refinement factor was kept constant at $N_{\text{refine}} = 3$ i.e. 27 times more points in the augmentation sphere. The rapidly varying projector function or the hard part of the local pseudopotential, respectively, can be represented more accurately on the fine grid. The wave function is assumed to be smooth and so its values are interpolated from the coarse grid points to the fine grid points in between them. i and k label coarse and fine grid points, respectively.

$$\left\langle p^{\ell m} \middle| \psi \right\rangle = \sum_k p_k^{\ell m}\, \psi_k^{\text{fine}} = \sum_k p_k^{\ell m} \sum_i \mathcal{I}_{ki} \psi_i^{\text{coarse}} \tag{5.21}$$

The interpolation operator $\hat{\mathcal{I}}$ uses Lagrange interpolation of the values at $2\,N_{\text{itp}}$ grid points with constant coefficients (see Chapter 3.3) if the grids are aligned, i.e. coarse grid points are simultaneously fine grid points. Those fine grid points that are identical with the coarse grid do not require interpolation. If there is no fixed alignment between the grids, but rather the fine grid is fixed to the atomic position, the interpolation coefficients depend on the position of the core relative to its nearest coarse grid point. As emphasized in Chapter 3.3, the Lagrange interpolation technique is equivalent to the finite difference approximation. Typically the order of Lagrange interpolation is chosen in agreement with the order of the finite difference formula applied for the kinetic energy and the Laplacian to keep consistency and suppress numerical errors. As well as the finite difference derivatives the interpolation operator relates only grid points that differ at most N_{itp} in their index along each cartesian direction. The interpolation operator can be set up as a product of of interpolation coefficients for each spatial direction

$$\hat{\mathcal{I}} = \hat{\mathcal{I}}_x \otimes \hat{\mathcal{I}}_y \otimes \hat{\mathcal{I}}_z.$$

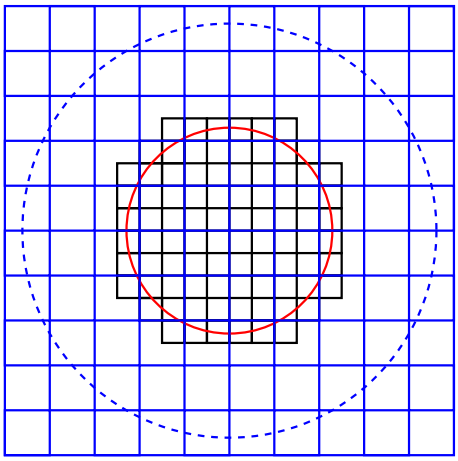

Figure 5.4: Double grid technique. Inside the augmentation radius r_{cut}, a locally refined grid is introduced. The values of the coarse grid are interpolated to the fine grid, including information of N_{itp} neighboring coarse-grid points. This defines the outer radius $r_{\mathrm{itp}} = r_{\mathrm{cut}} + N_{\mathrm{itp}}\, h$, where h is the grid spacing of the coarse grid. The results of the projection operation performed on the fine grid show significantly less unphysical dependency of the sphere's relative position with respect to the coarse grid points.

Disregarding if the coarse and the fine grid are aligned, the interpolation coefficients for each of these operators $\hat{\mathcal{I}}_{direction x,y \text{ or } z}$ are independent of the coarse grid index, if the grid spacings of coarse and fine grid are related by an integer factor.

However, after the action of the dyadic operator $|p\rangle \langle p|$ onto a wave function $|\psi\rangle$, the result is a scalar multiple of the projector $|p\rangle$. This one has to be represented on the coarse grid again. The straightforward way would be to drop all the additional grid points that make up the fine grid such that only the coarse grid is kept. Although this looks correct we have to keep in mind that the projector is a part of the Hamiltonian. The Hamiltonian is constrained to be an hermitian operator and therefore the projector must be so, too. The nonlocal potential is as well a real function as the local parts so that the matrix representation must be symmetric (for **k**-points other then the Γ-point the projectors are hermitian). The manner outlined above would be

$$\hat{P} = |p\rangle \langle p| \hat{\mathcal{I}} \tag{5.22}$$

which is obviously not symmetric if $\hat{\mathcal{I}}$ differs from unity. Thus the correct translation from the fine grid back to the coarse grid representation is an inverse interpolation:

$$\hat{P} = \hat{\mathcal{I}}^{\dagger} |p\rangle \langle p| \hat{\mathcal{I}} \tag{5.23}$$

The action of these projectors are required every time that the Hamiltonian is applied to a wave function. In order to speed it up the performance, the interpolation is

performed in advance when the projectors are set up. The projector functions are so directly merged with the interpolation operators

$$|P\psi\rangle = \hat{\mathcal{I}}^{\dagger} |p\rangle \langle p| \hat{\mathcal{I}} |\psi\rangle = |\mathcal{I}p\rangle \langle \mathcal{I}p| \psi\rangle \tag{5.24}$$

where the interpolated projectors $|\mathcal{I}p\rangle$ are represented on the coarse grid. This can be done because both, the interpolation operators and projector functions are unchanged as long as the atomic positions are constants. This ordering of the summations saves a lot of computational effort compared with the case when the interpolation has to be performed every time that the Hamiltonian act upon a wave function. The radial extent of the region where the interpolated projectors are nonzero is not given by the cutoff radius r_{cut} but rather by $r_{\mathrm{proj}} = r_{\mathrm{cut}} + N_{\mathrm{itp}}\, h$, where h is the coarse grid spacing, because the inverse interpolation assembles information in a nonlocal manner. When pseudopotentials are applied, the augmentation spheres are supposed not to intersect.

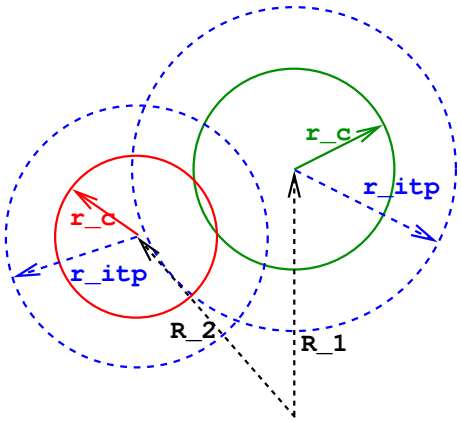

Figure 5.5: Intersection of the outer augmentation spheres. The interpolation of the projectors inside the cutoff radius r_{cut} to the refined grid requires data of the coarse grid points inside the outer the sphere with radius r_{itp}. Pseudopotential theory does not allow the augmentation spheres to intersect.

5.7 Density mixing

Self-consistency usually is approached in an iterative algorithm as mentioned in Chapter 5.1. We can evaluate the new density as a functional of the given input density $\tilde{n}\{n(\mathbf{r})\}$. Therefore we define $\mathcal{F}\{n(\mathbf{r})\} = \tilde{n}\{n(\mathbf{r})\} - n(\mathbf{r})$. The self-consistent density will satisfy $\mathcal{F}\{n^*(\mathbf{r})\} = 0$. This corresponds to a set of coupled nonlinear equations to be solved. Different solving methods are available. Here, the simple mixing and Broyden mixing scheme are introduced but several others are available, among them Pulay mixing, [24, 24].

Simple mixing

Simple density mixing works just as the steepest descent method. Here the residual to be minimized is $\langle \mathcal{F} | \mathcal{F} \rangle$. The set of non-linear equations is assumed to be linear for small changes so that the minimum is quadratic and the update vector is proportional to the gradient.

$$n^{(m+1)} = n^{(m)} + \alpha \mathcal{F}\{n^{(m)}\} \tag{5.25}$$

Simple mixing shows linear convergence i.e. an exponentially decreasing behavior is expected. Nevertheless *critical slowing down* can be observed as a significant change in the slope that occurs earlier the larger the mixing ratio is. This effect is known from *conjugate gradient* methods for linear solvers where the long wave length error spoils the convergence. In the self consistency solver the slowing down occurs due to a too large mixing ratio. One could also speak of a damping too weak to suppress fluctuations. This is crucial for metals. The eigenvalues of the Hamiltonian change slightly during the self-consistency iteration. This may cause a reordering of the levels. Since a metal is supposed to show a nonzero density of states around the Fermi level, occupation numbers for these states may change drastically which leads to *charge sloshing*. Introducing an artificial smearing temperature helps to converge (see Chapter 5.9). Nevertheless, simple mixing is very stable i.e. does not get trapped easily in a local minimum.

Broyden mixing

Newton-Raphson methods are known to perform well (quadratic convergence) for linear systems but need the full Jacobian matrix and its inverse explicitly. The update goes as follows

$$n^{(m+1)} = n^{(m)} - \left[\mathcal{J}\{n^{(m)}\}\right]^{-1} \mathcal{F}\{n^{(m)}\} \tag{5.26}$$

$$\mathcal{J}\{n^{(m)}\} = \left.\frac{\delta F\{n\}}{\delta n}\right|_{n=n^{(m)}} \tag{5.27}$$

In one dimension this procedure is also known as Newton method for finding zero points. Handling with many degrees of freedom the exact Jacobian is very expensive

to generate and direct inversion even scales with $\propto n^3$ (with the third power of the dimensions). Quasi-Newton methods benefit from the *quadratic convergence* of the class of Newton-Raphson methods but instead the inverse Jacobian is approximated by a sum of *dyads* that can easily be represented as outer product of two vectors. The algorithm for *Broyden's 2nd method* is here kept in the bra-ket-notation which expresses scalar products.

$$n^{(m+1)} = n^{(m)} + \left(\mathbf{1} - \left\langle v^{(m)} \middle| \mathcal{F}^{(m)} \right\rangle\right) u^{(m)} \tag{5.28}$$

with

$$u^{(m)} = \Delta n^{(m)} + \alpha \Delta \mathcal{F}^{(m)} - \sum_{i=2}^{m-1} \left\langle v^{(i)} \middle| \Delta \mathcal{F}^{(m)} \right\rangle u^{(i)} \tag{5.29}$$

$$v^{(m)} = \frac{\Delta \mathcal{F}^{(m)}}{\left\langle \Delta \mathcal{F}^{(m)} \middle| \Delta \mathcal{F}^{(m)} \right\rangle} \tag{5.30}$$

with the definitions $\Delta n^{(m)} = n^{(m)} - n^{(m-1)}$ and $\Delta \mathcal{F}^{(m)} = \mathcal{F}^{(m)} - \mathcal{F}^{(m-1)}$. In real implementations the sum $\sum_{i=2}^{m-1}$ does not run over all steps that have been done before but the Broyden history is truncated to a finite number of steps. Alternatively the history can be discarded and the algorithm be restarted after a certain number of steps. The latter has shown to work fine. The mixing ratio α looks like the simple mixing ratio. It has turned out that with simple mixing this ratio has to be kept below a α_{critical} to damp oscillations and charge sloshing. α_{critical} depends on the dielectric response of the system and may be very small for metals. The Broyden-α may be much larger. Values like 0.2 and 0.3 have shown to perform well.

A comparison between the Broyden mixing scheme and simple mixing can be seen in Figure 5.6. Here the change in density $\langle \mathcal{F} | \mathcal{F} \rangle$ is a number to measure how the system approaches self-consistency. Explicitly written it is

$$\langle \mathcal{F} | \mathcal{F} \rangle = \frac{1}{V} \int_V \mathrm{d}^3\mathbf{r} \, [\, \tilde{n}(\mathbf{r}) - n(\mathbf{r}) \,]^2 \tag{5.31}$$

and $\sqrt{\langle \mathcal{F} | \mathcal{F} \rangle}$ is the root mean square of the density.

The change in density converges much faster for Broyden-mixing although it follows a very volatile, not monotonous curve. This behavior depends on the level of convergence of the new approximate eigenstates.

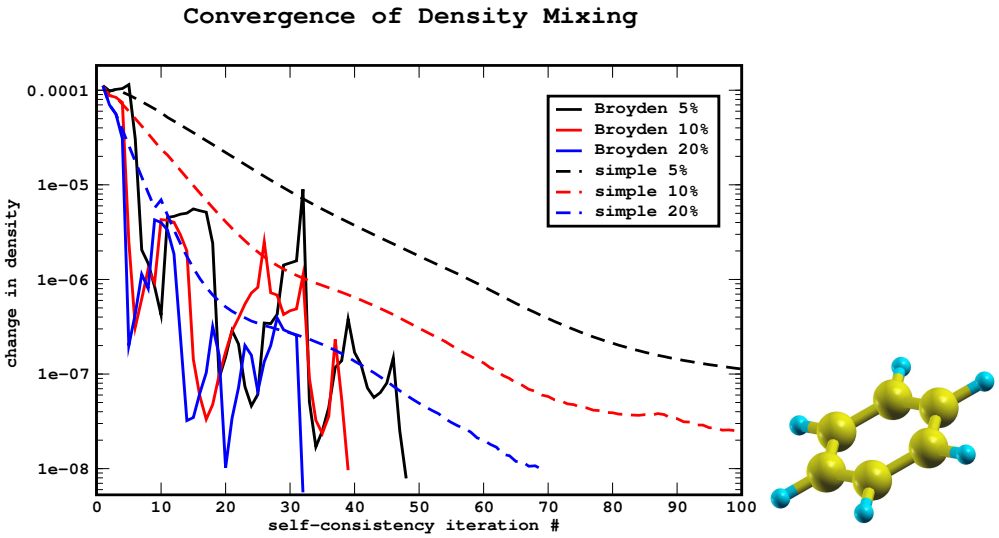

Figure 5.6: Convergence with a Broyden mixing scheme. With simple mixing (straight mixing) the change in density follows a smooth function. The results of the Broyden-type mixing schemes are not at all monotonous but reach the threshold performing much less steps. Calculation of benzene in a $8.3 \times 8.3 \times 4.1$ Å^3 box with finite BCs and 12 Broyden history elements.

5.8 Subspace diagonalization method

As long as the density changes a lot at each self-consistency iteration step it is advantageous to stop the eigenstate solver after a few steps in order to save time. Using very poor approximations of the eigenstates requires more steps until self-consistency is reached but converging them every time down to a tiny residual. The approximate eigenstate may contain remaining portions of other states. Therefore a subspace method is invoked. The matrix elements of the Hamiltonian with respect to the approximate eigenstates of each Bloch state are explicitly computed.

$$H_{ij} = \left\langle \psi^{(i)}_{\text{approx}} \right| \hat{H} \left| \psi^{(j)}_{\text{approx}} \right\rangle \tag{5.32}$$

This matrix is exactly diagonalized so that

$$\hat{H} = \hat{S}\, \hat{D}\, \hat{S}^{\dagger} \tag{5.33}$$

where $\hat{S}$ is a unitary operator and and $\hat{D}$ a diagonal matrix. The eigenvalues D_{ii} are taken as new eigenvalues $\epsilon^{(i)}_{\text{new}}$ for the next self-consistency step, analogously the new eigenstates are transformed according to the eigenvectors

$$\left| \psi^{(i)}_{\text{new}} \right\rangle = \sum_j S_{ij} \ \left| \psi^{(j)} \right\rangle \tag{5.34}$$

This method is very efficient as long as the number of bands in the system is kept small and only few CG/SD-steps are preformed. Converging the eigenstates very far makes this method redundant because then the states are close to eigenstates and the off-diagonal matrix elements are of tiny magnitude. However it scales $\propto N_{\text{bands}}^3$ for the diagonalization and linear combination of the new wave functions. Additionally it requires a number of operations $\propto N_{\text{bands}}^2$ with a large prefactor for setting up the matrix elements.
When a calculation is performed from the start and so atomic orbitals are used as initial wave functions the subspace method reflects the hybridization of the atomic states into bonding and anti-bonding linear combinations before the first self-consistency cycle starts.

5.9 Bisection method

The new density is calculated from the eigenstates of the Hamiltonian. The Kohn-Sham states are occupied with electrons according to the Fermi-Dirac distribution which is a function of the Kohn-Sham energies E_i (i labels all states i.e. all bands, spins and k-points) and the Fermi energy E_{F} which is unknown. The sum of all occupation number has to be equal to the number of electrons in the system, N_{ele}. This is achieved by tuning the Fermi level E_{F} until

$$\sum_i \frac{1}{\mathbf{e}^{\beta(E_i - E_{\text{F}})} + 1} - N_{\text{ele}} = 0 \tag{5.35}$$

where $\beta = 1/(k_{\text{B}}T)$ corresponds to a fictitious smearing temperature explained below. We have to find a null in the function $\sum_i f(E_i, E_{\text{F}}) - N_{\text{ele}}$ with respect to E_{F}.

The null of a function $g(e)$ can be found applying the bisection method. This is based on a search interval which is iteratively divided into two smaller intervals. If the function g is monotonous in the start interval $[e_1, e_2]$ and has a null, the method is supposed to always converge. One iteration of the bisection performs the following steps.

1. evaluate $g(e_1) = g_1$ and $g(e_2) = g_2$. By assumption we know that g_1 and g_2 are of opposite sign since the interval contains exactly one null.
2. bisect the interval $e_{\text{m}} = \frac{1}{2}(e_1 + e_2)$.
3. evaluate $g(e_{\text{m}}) = g_{\text{m}}$.
4. if g_1 and g_{m} are of opposite sign the null must be in $[e_1, e_{\text{m}}]$. restart with $[e_1, e_{\text{m}}]$, otherwise restart with $[e_{\text{m}}, e_2]$.

The convergence of this algorithm is known to be linear since the error will be divided by 2 every iteration. the length of the last interval gives an estimate for the error.

The reason to use a finite temperature in the Fermi-Dirac distribution is not the systems real temperature. Rather smeared out occupation numbers around the Fermi level. Systems with a band gap will not notice the finite temperature since the highest state below the gap will be occupied and the first states above the gap unoccupied. However, bands that cross the Fermi level produce a non-zero density of states at E_{F}. Also using a finite number of **k**-points will produce some eigenenergies close to E_{F}. Within the self-consistency cycle, these energies may change slightly. Consider the Fermi-Dirac distribution at $T_{\mathrm{smear}} = 0$ i.e. a step function that drops discontinuously at E_{F}. If the energy of an unoccupied state above the Fermi level falls below the energy of an occupied states, these states will exchange their occupancies. The new density,$\tilde{n}(\mathbf{r})$, is created from the occupied states only. Therefore the new density will deviate a lot from the old density, $n(\mathbf{r})$. The changed density may effect the eigenenergies to assume their previous ordering. One can see that there is an instability leading to oscillations and a constant change in density. In order to damp this out, the finite temperature produces partial occupancies around the Fermi level E_{F}, mainly in the interval $[E_{\mathrm{F}} - k_{\mathrm{B}}T_{\mathrm{smear}}, E_{\mathrm{F}} + k_{\mathrm{B}}T_{\mathrm{smear}}]$. The exchange of two energies E_i and E_j does then not induce a change of the occupancies f_i and f_j from 0 to 1 and vice versa but the change is proportional to $(E_i - E_j)/(k_{\mathrm{B}}T_{\mathrm{smear}})$ if both energies are close to the Fermi level, i.e. $|E_{i\,\mathrm{or}\,j} - E_{\mathrm{F}}| \ll k_{\mathrm{B}}T$. Consequently, these oscillations may be damped by increasing the smearing temperature T_{smear}. Temperature smearing is usuallv turned on for metallic systems.

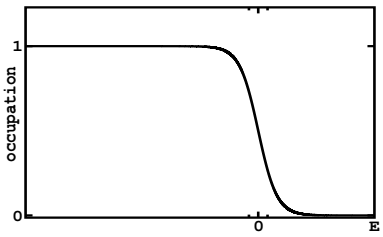

$$n(E_{\mathrm{KS}}) = \frac{1}{\mathbf{e}^{\beta(E-E_{\mathrm{F}})} + 1} \tag{5.36}$$

Figure 5.7: Fermi-Dirac distribution function. A finite temperature enables a linearization around E_{F} which is 0 in the plot.

5.10 Forces

According to the Hellmann-Feynman theorem, the forces on the atomic cores may be computed directly. The *Born-Oppenheimer* approximation allows to treat the atomic positions as external parameters. The force on an atom is thus the gradient of the total energy with respect to the atomic position.

$$-\mathbf{F}_a = \frac{\partial E_{\text{tot}}}{\partial \mathbf{R}_a} = \frac{\partial}{\partial \mathbf{R}_a} \langle \Psi | \hat{H} | \Psi \rangle \tag{5.37}$$

$$= \frac{\partial \langle \Psi |}{\partial \mathbf{R}_a} \hat{H} | \Psi \rangle + \langle \Psi | \frac{\partial \hat{H}}{\partial \mathbf{R}_a} | \Psi \rangle + \langle \Psi | \hat{H} \frac{\partial | \Psi \rangle}{\partial \mathbf{R}_a} \tag{5.38}$$

using the eigenvalue equation for the ground state $\hat{H} | \Psi \rangle = E_{\text{tot}} | \Psi \rangle$ and its adjoint $\langle \Psi | \hat{H} = E_{\text{tot}} \langle \Psi |$ gives

$$= \frac{\partial \langle \Psi |}{\partial \mathbf{R}_a} E_{\text{tot}} | \Psi \rangle + \langle \Psi | \frac{\partial \hat{H}}{\partial \mathbf{R}_a} | \Psi \rangle + \langle \Psi | E_{\text{tot}} \frac{\partial | \Psi \rangle}{\partial \mathbf{R}_a} \tag{5.39}$$

$$= E_{\text{tot}} \frac{\partial \langle \Psi | \Psi \rangle}{\partial \mathbf{R}_a} + \langle \Psi | \frac{\partial \hat{H}}{\partial \mathbf{R}_a} | \Psi \rangle \tag{5.40}$$

Due to the norm conservation condition $\langle \Psi | \Psi \rangle = N_{\text{elec}}$ its derivative vanishes.

$$\Rightarrow \quad \mathbf{F}_a = - \langle \Psi | \frac{\partial \hat{H}}{\partial \mathbf{R}_a} | \Psi \rangle \tag{5.41}$$

Although the ground state $|\Psi\rangle$ should be the many-body state, this holds for the single particle states $\left| \Psi_{\text{KS}}^{(i)} \right\rangle$ occupied according to their energy eigenvalues $\epsilon_{\text{KS}}^{(i)}$ with the weight f_i (see Chapter 5.9). The kinetic energy term in the Hamiltonian does not depend on the atomic positions so it is sufficient to regard the derivative of the potential operator

$$\mathbf{F}_a = - \sum_i f_i \left\langle \Psi_{\text{KS}}^{(i)} \right| \frac{\partial \hat{V}}{\partial \mathbf{R}_a} \left| \Psi_{\text{KS}}^{(i)} \right\rangle \tag{5.42}$$

5.11 Application

The results of the electronic structure calculation may be used for many purposes. Some applications are explained in detail below.

Polarizability

The response of a molecule to an external electrical field is the formation of a dipole i.e. the field **E** polarizes the molecule. Due to the shifted minimum of the local potential, the electron density will move its center of mass opposite to the field. The ionic charges do not move in 1st order approximation due to their much higher mass. Ions and valence electrons together form an effective dipole **P**. In the limit of very small field strength, the polarization process can be assumed linear

$$P_i = \sum_{j=1}^{3} \alpha_{ij} E_j \tag{5.43}$$

where the α_{ii} is the polarizability with respect to the spatial direction i. These can be calculated easily by taking the differences between the dipole moment of the self-consistent charge density with and without electrical field.

$$\alpha_{ij} = \frac{\partial P_i}{\partial E_j} = \lim_{E_j \to 0} \frac{P_i(E_j) - P_i(0)}{E_j} \tag{5.44}$$

Of course the values for E_j have to be chosen small enough so that the polarization effect is still linear but large enough to prevent numerical errors in the difference. Figure 5.8 shows an example setup.

Band structure

In the computation of periodic systems it is made use of *Bloch*'s theorem. This means that for a periodic boundary condition, all quantities have to be integrated in reciprocal space. In practice, a set of **k**-points has to be evaluated. Of course the spectrum of single-article energies of these self-consistent **k**-points provides some information about the band structure already but they do not resolve e.g. band gaps in detail. Therefore non-self-consistent **k**-points are applied:
A self-consistent density is computed with some **k**-points (the larger the super cell the less points are needed to converge the calculation with respect to this number). This yields a self-consistent Hamiltonian. Now this Hamiltonian is applied to an arbitrary set of **k**-points and solved for its lowest eigenvalues at each **k**-point. Usually a path within the first Brillouin zone is chosen in order to analyze the dispersion relations, band gaps and effective masses. The path samples a dense set of **k**-points along the lines of high symmetry.

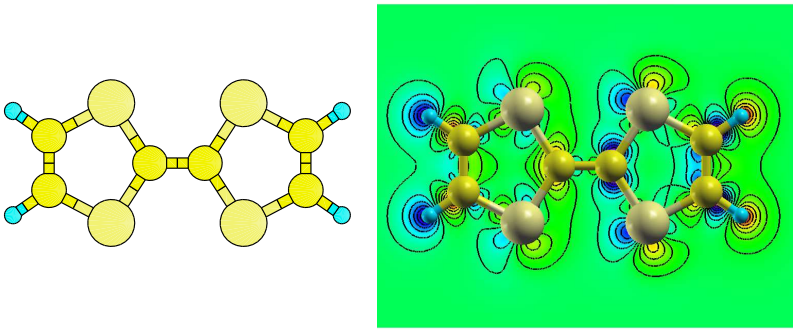

Figure 5.8: Polarizability calculations on tetrathiofulvalene (TTF). An electrical field of 5.0 mV/Å in x-direction induced a dipole moment of -0.01 Åe in x-direction so that the polarizability coefficient is $\alpha_{xx} = -2.0\,\text{Å}^2/\text{V}$. The maximal change of valence density $\max(|\Delta n(\mathbf{r})|)$ is $0.45\,\text{m}e/\text{Å}^3$ which is less than 1% of the maximum of value of the valence density. Consequently, the electrical field is sufficiently small to apply assume linearity. The blue areas correspond to a negative change whereas the red color indicates a density gain.

Molecular dynamics

Molecular dynamics (MD) is the classical motion of the atoms according to the *ab initio*-calculated forces. Demanding energy conservation over the time evolution we may simulate the translations, vibrations and rotations of molecule or even the propagation of lattice distortions by introducing a discretized and thus finite time step. The total energy E_{MD} must be conserved which contains the total electronic energy and additionally the (non-relativistic) kinetic energy of the cores.

$$E_{\text{MD}} = E_{\text{elec}} + \sum_a \frac{\mathbf{p}_a^2}{2m_a} \tag{5.45}$$

where the momenta $\mathbf{p}_a(t)$ are updated at every time step according to the self-consistently calculated forces

$$\mathbf{p}_a(t^{(m+1)}) = \mathbf{p}_a(t^{(m)}) + \mathbf{F}_a(t^{(m)}) \cdot \Delta t \tag{5.46}$$

and the atomic positions $\mathbf{R}_a(t)$ according to the velocities

$$\mathbf{R}_a(t^{(m+1)}) = \mathbf{R}_a(t^{(m)}) + \frac{\mathbf{p}_a(t^{(m)})}{m_a} \cdot \Delta t. \tag{5.47}$$

Geometry optimization

Geometry optimization is means the minimization of the atomic forces. This can be achieved in the limit of strong friction in molecular dynamics calculations. Friction

means that the energy is not conserved but rather taken away from the atomic cores after each molecular dynamics time step. The maximal friction possible can be realized by taking away the entire momenta of the atoms after the position update. This procedure definitely converges to an minimum of the total energy and can be considered as the *over-damped* case of an oscillator since its convergence is linear close to the minimum. Successful approaches have been made by estimating the right friction coefficient to hit the *aperiodic* limit or apply quasi-Newton methods analogous to those introduced for the self-consistency iterations (see Chapter 5.7).

6 Parallelization and scalability

6.1 Parallel computation

The premise to perform a calculation in parallel is the ratio independent tasks over interacting ones. Many operations in real space are local and can so be performed independently for each of the grid points. The native way of parallelizing such a independent operation thus is simply linear e.g. grid points 1 to 10 are stored and computed on process element # 0, 11 to 20 on # 1 and so on. Now taking into account non-local operations, this means a lot of communication between the processes. If we consider a fully non-local operation where each of the grid points has to interact with each other, the total amount for communication needed scales as $N_\mathrm{P}(N_\mathrm{P}\text{-}1)$ and the time needed $\propto (N_\mathrm{P}\text{-}1)$. This is for example the case when distributing the workload and the memory for a Fourier transform among N_P process elements. The real-space techniques introduced in Chapter 5 intrinsically avoid these completely non-local operations.

As illustrated in Chapter 3, derivatives as e.g. the Laplacian become non-local operators when space is discretized but can be truncated to a finite interaction radius without losing much of accuracy. These operations require data from their neighboring grid points. At the borders of the super cell neighboring data is either 0 (isolated case) or can be retrieved from the other end of the cell (periodic case). To parallelize this in the linear way, mentioned previously, a lot of communication between process elements has to be established to exchange the required data. Therefor one adopts the parallelization scheme to fit best to kind of nearest neighbor interaction arising from the non-local derivative approximations. The concept is called *domain decomposition* and consists of a parallelization along each spatial dimension. Of course the one-dimensional case will end up in linear distribution again. Data that has to be exchanged among process elements causes communication which is an overhead compared to the performance of the same method in a single process. The parallel efficiency is defined to be the speedup (The factor by which a program is performed faster on N_P process elements) divided by the number of process elements. Obviously an overhead due to communication lowers the parallel efficiency. The three dimensional domain decomposition reduces the communication needed for a finite difference derivative most when the surface is minimized whereas the surface can be identified with the number of border elements of all cuboid-shaped domains. The

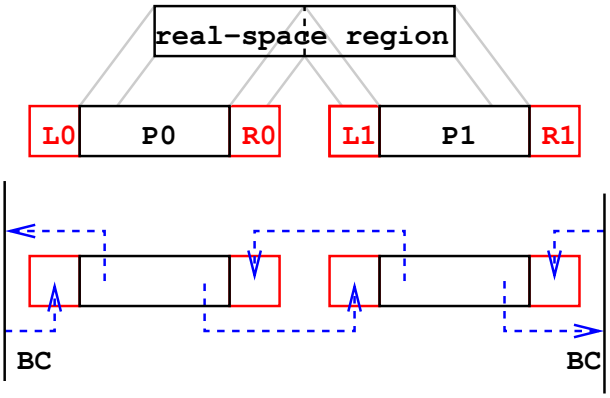

Figure 6.1: Domain decomposition in a one-dimensional scheme. The real-space region is divided into equal parts, each belonging to a specific process element. However, semi-local operations require the data of neighboring grid points. For this reason, so called *halos* are attached to the local arrays at each interface. These are auxiliary arrays, containing a copy of the border data of the neighboring domain. The update of these copies is sketched roughly in the lower part of the picture. Each process sends its border data into the halo of the nearest neighbor via the **MPI**-environment. The data sent across the boundary (BC) will be treated according to the boundary conditions. Finite boundary conditions will multiply the data with 0 (or just not send) whereas periodic boundary conditions require the Bloch-phase factor $\mathbf{e}^{\mathrm{i}kL}$ for the wave functions, where L is the extent of the one-dimensional unit cell and k the Bloch vector.

surface of a three dimensional grid $N_x \times N_y \times N_z$ then is

$$\begin{aligned} S(m_x, m_y, m_z) &= 2\ (m_x N_y N_z + m_y N_x N_z + m_z N_x N_y) \\ &= 2\, N_x N_y N_z \cdot \left(\frac{m_x}{N_x} + \frac{m_y}{N_y} + \frac{m_z}{N_z} \right) \end{aligned}$$

under the constraint that all N_i and m_i are integer values. The ratio of volume by surface (in terms of grid points) is best for a domain shape which is as close as possible to the cube.

6.2 Inter process communication

Parallelization with the `MPI`-library (`Message Passing Interface`) has become a standard in the last decade and can be used with a wide variety of parallel computer systems. According to its name, messages containing data are exchanged between the processes via a network, a hub or in special cases even shared memory although there are faster ways to use these setups such as `OpenMP` or `ShMem`. The data from a neighboring process is then transferred into the extensions of the enlarged array

so that the semi-local function working on the array do not have to manage a discontinuity in memory. Since the interaction from derivatives only involves cartesian neighbors of grid points, this holds also for the processes. A process only has to communicate with its 6 direct cartesian neighbor processes. This fact limits the amount of communication to a fix ratio and so parallel efficiency will not break down at a high level of parallelization. The application becomes extremely efficient on a supercomputer where the point-to-point communication network is constructed in a 3-dimensional cartesian torus as e.g. the `BlueGene`-type.

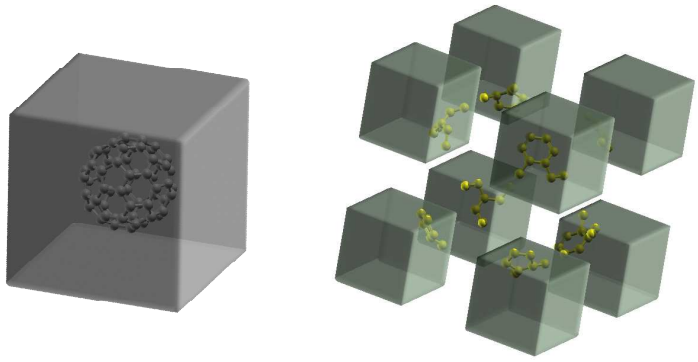

Figure 6.2: Domain decomposition. A cubic super cell is divided into $2 \times 2 \times 2$ parts. The tasks of each domain is given to a specific process element (PE). The real-space representation allows an efficient parallelization of the total workload. For local and quasi-local operators the reduced communication is exploited by the fact hat each PE only needs to exchange data with its nearest neighbors. For simple boundary conditions (periodic or finite) this number is limited to the 6 cartesian neighbors.

6.3 Parallel speedup

Let T_1 be the time needed to perform the computation with one process element. Amdahl's law states that a program spending αT_1 in the sequential part and $(1-\alpha)T_1$ in the part that can be parallelized can at maximum reach a speedup of $S_{\max} = 1/\alpha$. This is intuitive considering that the time for a parallel execution is $T_N = \alpha T_1 + (1 -$

Figure 6.3: Prediction model for parallel speedup. Serial parts of the code hinder the speedup to get larger than $1/\alpha$. Unrestricted all-to-all communication may even slow down and thus lead to a negative slope meaning that the computation takes more time using more processors.

$\alpha)T_1/N$. The parallel speedup $S(N) = T_1/T_N$ then is

$$S(N) = \frac{N}{\alpha(N-1)+1}$$

In the limit $N \to \infty$ the speedup $S(N) \to 1/\alpha$ is limited. This motivates to parallelize an application as much as possible before running it in massively parallel.

In general there is another quantity influencing the speedup: When communication is not restricted in any form, we have $N(N\text{-}1)$ communication operations which need at least N-1 times the overhead of a communication operation. This may lead to a speedup curve with an absolute maximum at a certain number of process elements. This means that the parallel efficiency drops heavily for higher numbers. Fortunately the cartesian domain decomposition restricts communication to the 6 cartesian neighbors. Instead of comparing the parallel execution time to T_1 we can take T_8(exactly 2 PEs in each direction) as a reference time so that a drop of the speedup can only arise from global communication.

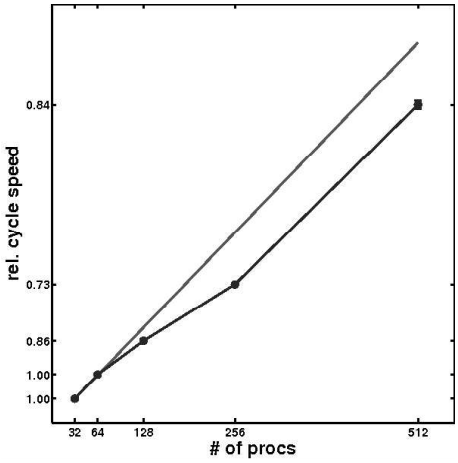

Figure 6.4: Parallel speedup S_N for 32 water molecules in a $10\times10\times10$ Å^3 box with periodic boundary conditions. Plotted is the total time ratio $S_\mathrm{N} = T_{32}/T_N$, where N is the number of process elements (PEs). The times have been compared to T_{32}, the time needed with the smallest set of processors. This scaling curve has been measured on a **IBM BlueGene L** where the local mapping of the process ranks is exploited to minimize the communication processes that are due to the domain decomposition. A close look at the data shows a slightly lower parallel efficiency $E_\mathrm{parallel} = S_\mathrm{N}/N$ of the setup with 256 PEs than at 512 PEs. This is an effect of the local mapping that does not fit perfectly to the hardware given periodic boundary conditions when using half a rack (256 nodes).

7 Transport Theory

The determination of electronic transport properties in the quantum regime by calculation is a goal of current research. Experimental techniques to measure conductivity have brought up a new aspects in the development of scanning tunnelling microscopy and also break junctions. The focus has settled to the transport properties of single molecules. In this work, the transport properties of terephthalic acid are calculated using a real-space transport formalism that will be explained for the general case in this chapter.

Consider systems with two half infinite electrodes enclosing a junction. The electrodes can be a bulk-like structures, a films or wires whereas the geometry of the material inside the junction can be diverse. Systems of interest for transport calculations are layers of different materials, narrow cracks like in a break junction, lattice mismatches, impurities, molecules and many others. The procedure for calculating a setup which shows translational invariance in the leads exploits the fact, that the range of interactions described by the Hamiltonian can be considered finite. Therefore, the entire system is divided into three parts; the left electrode, the junction region and the right electrode. Each of these systems is solved separately first, then the solutions are matched together with the over-bridging boundary method.

7.1 Landauer-Büttiker ballistic transport

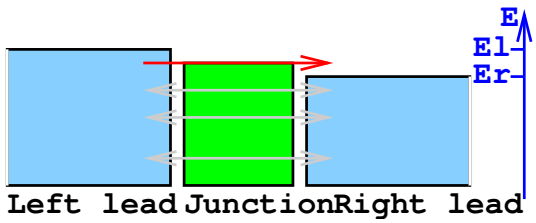

Figure 7.1: Scheme of the Landauer-Büttiker transport formalism. A junction is embedded between two semi-infinite conducting leads. The difference of chemical potentials (Fermi energies) $E_{\mathrm{L}} - E_{\mathrm{R}}$ affects that the right propagating electrons with energies E to contribute to a net current, if $E_{\mathrm{R}} < E < E_{\mathrm{L}}$ and if the junction itself shows a non-vanishing density of states $D(E)$ at that energy.

Electronic transport is well described by the very simple model of the Landauer-Büttiker formalism [11]. Ballistic means, that the only scattering that occurs is the elastic scattering process at the junction itself. We assume to have a setup aligned in a way that a scattering region is embedded between two electrodes. The scattering region contains the structure of interest whereas the electrodes are semi-infinite metallic leads. In the following the names 'left' (L) and 'right' (R) will refer to the electrode of the incident electrons and the transmitted ones, respectively. Let us assume electrons propagating from left to right and from right to left. These electrons will be referred as right-movers and left-movers, respectively. An incident electron can be either reflected or transmitted so that transmission and reflection probability add up to unity $\mathcal{T} + \mathcal{R} = 1$. However, the net current across the junction region is zero, if there are as many right-movers as left-movers, but in general we may assume different levels of the chemical potential μ (at zero temperature, the chemical potentials is equivalent to the Fermi energy E_F). A finite difference between the chemical potentials of the two electrodes causes an electrical field across the region of the junction. Consider μ_L to be larger than μ_R. Then all right-movers with energy E will contribute to a net current if, $\mu_\mathrm{R} > E > \mu_\mathrm{L}$. Their contribution to the total current is proportional to the charge of each electron e, its transmission probability $\mathcal{T}$ and its group velocity $\mathbf{v}$ expressed by the derivative of the dispersion relation $E(\mathbf{k})$

$$I(\mathbf{k}) = -e\mathcal{T}(E)\frac{\partial E(\mathbf{k})}{\partial \hbar k} \tag{7.1}$$

where k denotes the component of $\mathbf{k}$ in transport direction. The total current resulting from all electrons in the energy range between $[\mu_\mathrm{R}, \mu_\mathrm{L}]$ including a factor 2 from the integration over the spins

$$\begin{aligned} I_\mathrm{total} &= 2\int_{k_\mathrm{R}}^{k_\mathrm{L}} I(k)\frac{\mathrm{d}k}{2\pi} = -2\int_{k_\mathrm{R}}^{k_\mathrm{L}} e\mathcal{T}(E)\frac{\partial E(\mathbf{k})}{\partial \hbar \mathbf{k}}\frac{\mathrm{d}k}{2\pi} \\ &= -\frac{2e}{h}\int_{\mu_\mathrm{R}}^{\mu_\mathrm{L}} \mathcal{T}(E)\mathrm{d}E \end{aligned} \tag{7.2}$$

In the following, the limit of zero voltage bias will be considered. Let the voltage difference $\mu_\mathrm{L} - \mu_\mathrm{R} \to 0_+$ become vanishing small. Then the dependency $\mathcal{T}(E)$ can be approximated by $\mathcal{T}(E_\mathrm{F})$.

$$I_\mathrm{total} \approx -\frac{2e}{h}\ \mathcal{T}(E_\mathrm{F})\ \ (\mu_\mathrm{L} - \mu_\mathrm{R}) \tag{7.3}$$

whereas the voltage is $V = (\mu_\mathrm{L} - \mu_\mathrm{R})/(-e)$. The total conductance becomes

$$G_\mathrm{total} = \frac{I_\mathrm{total}}{V} = \frac{2e^2}{h}\mathcal{T}(E_\mathrm{F}). \tag{7.4}$$

This shows the intrinsic units of conductivity in the quantum regime: $G_0 = \frac{2e^2}{h}$ is often called 'quantum conductance' and $R_0 = \frac{h}{2e^2} = 25.8\,k\Omega$ 'quantum resistance'.

7.2 Method

The transport formalism in real space is very intuitive within the framework of the Laudauer-Büttiker theory.
As outlined above, the entire transport setup is divided into three space parts, the scattering region embedded between the semi-infinite left and right electrode. An incident electron is described in the single-particle picture of the Kohn-Sham formalism by a wave function, which extends over all three volumes

$$\Psi(\mathbf{r}) = \begin{cases} \Psi_{\mathrm{L}}(\mathbf{r}), & \mathbf{r} \in \text{left electrode} \\ \Psi_{\mathrm{S}}(\mathbf{r}), & \mathbf{r} \in \text{scattering region} \\ \Psi_{\mathrm{R}}(\mathbf{r}), & \mathbf{r} \in \text{right electrode} \end{cases} \tag{7.5}$$

and obeys the Kohn-Sham equation for the incident energy E

$$\begin{pmatrix} \hat{H}_{\mathrm{L}} & \hat{H}_{\mathrm{LS}} & 0 \\ \hat{H}_{\mathrm{LS}}^{\dagger} & \hat{H}_{\mathrm{S}} & \hat{H}_{\mathrm{SR}} \\ 0 & \hat{H}_{\mathrm{SR}}^{\dagger} & \hat{H}_{\mathrm{R}} \end{pmatrix} \cdot \begin{pmatrix} \Psi_{\mathrm{L}}(\mathbf{r}) \\ \Psi_{\mathrm{S}}(\mathbf{r}) \\ \Psi_{\mathrm{R}}(\mathbf{r}) \end{pmatrix} - E \begin{pmatrix} \Psi_{\mathrm{L}}(\mathbf{r}) \\ \Psi_{\mathrm{S}}(\mathbf{r}) \\ \Psi_{\mathrm{R}}(\mathbf{r}) \end{pmatrix} = 0 \tag{7.6}$$

The diagonal elements $\hat{H}_{\mathrm{L}}$, $\hat{H}_{\mathrm{S}}$ and $\hat{H}_{\mathrm{R}}$ contain the local and non-local parts of the Hamiltonian of the left electrode, the scattering region and the right electrode, respectively. The off-diagonal element $\hat{H}_{\mathrm{LS}}$ represents the non-local interaction of the left electrode with the scattering region and analogously $\hat{H}_{\mathrm{SR}}$ the interaction of the scattering region with the right electrode. One may already see that the long ranged interaction of the left and right electrode across the junction is neglected, i.e. the element $\hat{H}_{\mathrm{LR}} = 0$ and therefore not denoted explicitly in equation (7.6).
The setup of the three partial volumes has been done arbitrarily and therefore must not affect the results. This imposes the constraint that the scattering wave function is continuous $\Psi_{\mathrm{L}}(\mathbf{r}_{\mathrm{Lb}}) = \Psi_{\mathrm{S}}(\mathbf{r}_{\mathrm{Lb}})$ and $\Psi_{\mathrm{S}}(\mathbf{r}_{\mathrm{Rb}}) = \Psi_{\mathrm{R}}(\mathbf{r}_{\mathrm{Rb}})$ in the left and right boundary plane, respectively (For simplicity, two planes, both perpendicular to the transport direction have been chosen to confine the scattering region). Taking out the central equation from (7.6), we get

$$\begin{aligned} &\hat{H}_{\mathrm{LS}}^{\dagger}\Psi_{\mathrm{L}}(\mathbf{r}) + (\hat{H}_{\mathrm{S}} - E)\Psi_{\mathrm{S}}(\mathbf{r}) + \hat{H}_{\mathrm{SR}}\Psi_{\mathrm{R}}(\mathbf{r}) = 0 \\ &\qquad \Leftrightarrow (E - \hat{H}_{\mathrm{S}})\Psi_{\mathrm{S}}(\mathbf{r}) = \hat{H}_{\mathrm{LS}}^{\dagger}\Psi_{\mathrm{L}}(\mathbf{r}) + \hat{H}_{\mathrm{SR}}\Psi_{\mathrm{R}}(\mathbf{r}). \end{aligned} \tag{7.7}$$

$\Psi_{\mathrm{L}}(\mathbf{r})$ is a superposition of the incident wave function and the reflected wave. The incident wave is an energy eigenstate of the (left) electrode because the electron cannot be subject to any interaction with the junction when it is still in a far left position. $\Psi_{\mathrm{R}}(\mathbf{r})$ is the transmitted wave only. We can expand $\Psi_{\mathrm{L}}(\mathbf{r})$ in eigenstates of the left electrode and the transmitted part $\Psi_{\mathrm{R}}(\mathbf{r})$ in eigenstates of the right electrode where we have to distinguish between propagating solutions and the so called *evanescent waves*, solutions with negative kinetic energy which describe an exponentially decaying tail. Assuming Ψ_{L} and Ψ_{R} are well known, we can find the scattering wave

function inside the junction

$$\Psi_{\mathrm{S}}(\mathbf{r}) = \hat{\mathcal{G}}(E)\left[\hat{H}^{\dagger}_{\mathrm{LS}}\Psi_{\mathrm{L}}(\mathbf{r}) + \hat{H}_{\mathrm{SR}}\Psi_{\mathrm{R}}(\mathbf{r})\right] \tag{7.8}$$

where the Green-function $\hat{\mathcal{G}}(E)$ is defined as

$$\hat{\mathcal{G}}(E) = \left(E - \hat{H}_{\mathrm{S}}\right)^{-1}. \tag{7.9}$$

Here, the Hamiltonian of the scattering region $\hat{H}_{\mathrm{S}}$ is required. Therefore, the electronic structure of the scattering region has to be determined in advance. The scatterer can be regarded as some impurity in the, otherwise infinite, lead. For this reason, the position of the boundary planes has to be chosen, such that the electronic structure has assumed bulk-like properties outside the boundaries. Then it is justified, that each region is treated in a separate calculation. The electronic structure of the right and left electrode region are determined in a straightforward bulk calculation, where 'bulk' only refers to the periodic boundary conditions in transport direction. The boundary conditions perpendicular to the transport direction are not affected.

The scattering region, however, is also solved with periodic boundary conditions in transport direction, but the fact, that the electronic structure has converged to bulk-values ensures, that the impurity hardly interacts with its periodic replica. The boundary conditions perpendicular to the transport direction have to be the same as the boundary conditions of the leads, e.g. if the leads are wires, the scattering region is a wire, too.

Now we assume that the interaction described by $\hat{H}_{\mathrm{LS}}$ and $\hat{H}_{\mathrm{SR}}$ are spatially localized around the boundary planes at $\mathbf{r}_{\mathrm{Lb}}$ and $\mathbf{r}_{\mathrm{Rb}}$, respectively. In particular the presumption is important that they have no spatial overlap. This requires a certain minimum thickness $(z_{\mathrm{Rb}} - z_{\mathrm{Lb}})$ of the scattering region. The minimum thickness is given by the maximum range of non-local interactions $z_{\mathrm{Rb}} - z_{\mathrm{Lb}} > 2\, r_{\mathrm{non-local}}$.

Discretizing space into equidistant grid points allows to separate the 3 dimensional scattering problem into a set of x-y-planes with $N_x \times N_y$ grid points in each plane and a one-dimensional scattering problem in z-direction (transport direction). The finite difference approximation (see Chapter 3) induces a relation of only $2\,N_f{+}1$ planes in the Hamiltonian i.e. the interactions are localized within the interaction radius $r_{\mathrm{int}} = (N_f{+}1)\, h_z$ where h_z is the grid spacing in z-direction. In terms of the x-y-planes the Hamiltonian takes the form of a banded diagonal matrix (just like in the one dimensional FD-case) where the matrix elements are itself matrices operating on each x-y-plane. A single equation at the plane $[k]$ out of this set looks like follows

$$\begin{aligned} &\hat{B}^{(-N_f)}_{[k-N_f]}\psi_{[k-N_f]} + \cdots + \hat{B}^{(-1)}_{[k-1]}\psi_{[k-1]} \\ &+ \left(\hat{H}_{[k]} - E\right)\psi_{[k]} + \hat{B}^{(1)}_{[k]}\psi_{[k+1]} + \cdots + \hat{B}^{(N_f)}_{[k]}\psi_{[k+N_f]} = 0 \end{aligned} \tag{7.10}$$

where $\hat{B}^{(-n)}_{[k]} = (\hat{B}^{(n)}_{[k]})^{\dagger}$ for all $n \in [1, N_f]$. Note that the plane index $[k]$ varies for the $\hat{B}$-operators on the left side of the central term $\hat{H}_{[k]}$ whereas it is constant on the

right side. We will see in equation (7.13) that this is necessary to obtain a hermitian Hamiltonian. The operator $\hat{H}_i$ contains the local potential, FD-approximated kinetic energy in x- and y-direction and the central FD-coefficient for the second derivative in z-direction. Then the elements $\hat{H}_{\mathrm{LS}}$, $\hat{H}_{\mathrm{SR}}$ and $\hat{H}_{\mathrm{S}}$ in the Schrödinger equation (7.6) are given for $N_f = 2$; the general case can be found in the appendix (A.2).

$$\hat{H}_{\mathrm{LS}}^{\dagger} = \begin{pmatrix} \cdots & 0 & \hat{B}_{[-1]}^{(-2)} & \hat{B}_{[0]}^{(-1)} \\ & \cdots & 0 & \hat{B}_{[0]}^{(-2)} \\ & & \cdots & 0 \\ & & & \cdots \end{pmatrix}, \tag{7.11}$$

$$\hat{H}_{\mathrm{SR}} = \begin{pmatrix} \cdots & & & \\ 0 & \cdots & & \\ \hat{B}_{[n-1]}^{(2)} & 0 & \cdots & \\ \hat{B}_{[n]}^{(1)} & \hat{B}_{[n]}^{(2)} & 0 & \cdots \end{pmatrix} \tag{7.12}$$

and

$$\hat{H}_{\mathrm{S}} = \begin{pmatrix} \hat{H}_{[1]} & \hat{B}_{[1]}^{(1)} & \hat{B}_{[1]}^{(2)} & & & 0 \\ \hat{B}_{[1]}^{(-1)} & \hat{H}_{[2]} & \hat{B}_{[2]}^{(1)} & \hat{B}_{[2]}^{(2)} & & \\ \hat{B}_{[1]}^{(-2)} & \hat{B}_{[2]}^{(-1)} & \hat{H}_{[3]} & \hat{B}_{[3]}^{(1)} & \hat{B}_{[3]}^{(2)} & \\ & \ddots & \ddots & \ddots & \ddots & \ddots \\ & & & & & \\ \ddots & \ddots & \ddots & \ddots & \ddots & \\ & \hat{B}_{[n-4]}^{(-2)} & \hat{B}_{[n-3]}^{(-1)} & \hat{H}_{[n-2]} & \hat{B}_{[n-2]}^{(1)} & \hat{B}_{[n-2]}^{(2)} \\ & & \hat{B}_{[n-3]}^{(-2)} & \hat{B}_{[n-2]}^{(-1)} & \hat{H}_{[n-1]} & \hat{B}_{[n-1]}^{(1)} \\ 0 & & & \hat{B}_{[n-2]}^{(-2)} & \hat{B}_{[n-1]}^{(-1)} & \hat{H}_{[n]} \end{pmatrix}. \tag{7.13}$$

where n_z is the number of x-y-planes in the scattering region. The requirement of no spatial overlap of the interactions may then be expressed as $n_z > 2\,N_f$.
At this point further explanation refers to the case of $N_f = 1$ to keep the notation as simple as possible. The main equation (7.7) becomes

$$(\hat{H}_{\mathrm{S}} - E) \cdot \begin{pmatrix} \psi_{[1]} \\ \psi_{[2]} \\ \vdots \\ \psi_{[n-1]} \\ \psi_{[n]} \end{pmatrix} = \begin{pmatrix} \hat{B}_{[0]}^{(-1)} \psi_{[0]} \\ 0 \\ \vdots \\ 0 \\ \hat{B}_{[n-1]}^{(1)} \psi_{[n+1]} \end{pmatrix}. \tag{7.14}$$

Leaving out all lines that have a 0 on the right side yields a shortened version of equation (7.8).

$$\begin{pmatrix} \psi_{[1]} \\ \psi_{[n]} \end{pmatrix} = \begin{pmatrix} \hat{\mathcal{G}}_{[1,1]} & \hat{\mathcal{G}}_{[1,n]} \\ \hat{\mathcal{G}}_{[n,1]} & \hat{\mathcal{G}}_{[n,n]} \end{pmatrix} \cdot \begin{pmatrix} \hat{B}^{(-1)}_{[0]} \psi_{[0]} \\ \hat{B}^{(1)}_{[n-1]} \psi_{[n+1]} \end{pmatrix} \tag{7.15}$$

We now introduce the solutions $\Phi^{\mathrm{L,R}}_{[k],i}$ of the left and right electrode determined either numerically or analytically (see Chapter 7.4) in a separated calculation. The waves $\Phi^{\mathrm{L,R}}_{[k],i}$ form a basis for the reflected and transmitted waves. Here $[k]$ denotes the x-y-plane index and i labels the different states. These are not only eigenstates of the Hamiltonian but also generalized Bloch-states. We identify for $\Psi_{\mathrm{L}}(\mathbf{r})$ the incident and the reflected waves and for $\Psi_{\mathrm{R}}(\mathbf{r})$ the transmitted wave

$$\Psi_{\mathrm{L}}([k], \mathbf{r}_{\parallel}) = \Phi_{\mathrm{inc}}([k], \mathbf{r}_{\parallel}) + \Psi_{\mathrm{ref}}([k], \mathbf{r}_{\parallel}), \tag{7.16}$$

$$\Psi_{\mathrm{R}}([k], \mathbf{r}_{\parallel}) = \Psi_{\mathrm{tra}}([k], \mathbf{r}_{\parallel}). \tag{7.17}$$

The incident wave $\Phi_{\mathrm{inc}}[k]$ is a single propagating eigenstate of the lead whereas $\Psi_{\mathrm{ref}}[k]$ and $\Psi_{\mathrm{tra}}[k]$ are expanded in terms of the solutions $\Phi^{\mathrm{L,R}}_{[k],i}$.

$$\Psi_{\mathrm{ref}}[k] = \sum_i r_i \; \Phi^{\mathrm{L}}_{[k],i} \tag{7.18}$$

$$\Psi_{\mathrm{tra}}[k] = \sum_i t_i \; \Phi^{\mathrm{R}}_{[k],i} \tag{7.19}$$

In the following, the summation over i will be replaced by the dot-product $(\,\cdot\,)$. The setup of leads is often symmetric i.e. the basis of solutions identical $\Phi^{\mathrm{L}} \equiv \Phi^{\mathrm{R}}$ but to keep it as general as possible we will continue labelling the left(L) and right(R) electrode.

$$\Psi_{\mathrm{L}}([k]) = \Phi^{\mathrm{inc}}_{[k]} + \Phi^{\mathrm{L}}_{[k]} \cdot \mathbf{r} \tag{7.20}$$

$$\Psi_{\mathrm{R}}([k]) = \Phi^{\mathrm{R}}_{[k]} \cdot \mathbf{t} \tag{7.21}$$

Consequently equation (7.15) becomes

$$\begin{pmatrix} \Phi^{\mathrm{inc}}_{[1]} + \Phi^{\mathrm{L}}_{[1]} \cdot \mathbf{r} \\ \Phi^{\mathrm{R}}_{[n]} \cdot \mathbf{t} \end{pmatrix} = \begin{pmatrix} \hat{\mathcal{G}}_{[1,1]} & \hat{\mathcal{G}}_{[1,n]} \\ \hat{\mathcal{G}}_{[n,1]} & \hat{\mathcal{G}}_{[n,n]} \end{pmatrix} \cdot \begin{pmatrix} \hat{B}^{(-1)}_{[0]} \left(\Phi^{\mathrm{inc}}_{[0]} + \Phi^{\mathrm{L}}_{[0]} \cdot \mathbf{r} \right) \\ \hat{B}^{(1)}_{[n-1]} \Phi^{\mathrm{R}}_{[n+1]} \cdot \mathbf{t} \end{pmatrix}. \tag{7.22}$$

Solving for $\mathbf{r}$ and $\mathbf{t}$ gives

$$\begin{pmatrix} \Phi^{\mathrm{inc}}_{[1]} - \hat{\mathcal{G}}_{[1,1]} \hat{B}^{(-1)}_{[0]} \Phi^{\mathrm{inc}}_{[0]} \\ -\hat{\mathcal{G}}_{[n,1]} \hat{B}^{(-1)}_{[0]} \Phi^{\mathrm{inc}}_{[0]} \end{pmatrix} =$$

$$\begin{pmatrix} \hat{\mathcal{G}}_{[1,1]} \hat{B}^{(-1)}_{[0]} \Phi^{\mathrm{L}}_{[0]} - \Phi^{\mathrm{inc}}_{[1]} & \hat{\mathcal{G}}_{[1,n]} \hat{B}^{(1)}_{[n-1]} \Phi^{\mathrm{R}}_{[n+1]} \\ \hat{\mathcal{G}}_{[n,1]} \hat{B}^{(-1)}_{[0]} \Phi^{\mathrm{L}}_{[0]} & \hat{\mathcal{G}}_{[n,n]} \hat{B}^{(1)}_{[n-1]} \Phi^{\mathrm{R}}_{[n+1]} - \Phi^{\mathrm{R}}_{[n]} \end{pmatrix} \cdot \begin{pmatrix} \mathbf{r} \\ \mathbf{t} \end{pmatrix}. \tag{7.23}$$

This $(2N_xN_y) \times (2N_xN_y)$ set of linear equations is to be solved directly.
Once the reflection coefficients r_i and the transmission coefficients t_i are found for this particular incident wave Φ_j^{inc}, we know the transmission matrix elements t_{ij}. The total transmission can then be evaluated according to

$$\mathcal{T} = \sum_{ij} \frac{v_j}{v_i} |t_{ij}|^2 \tag{7.24}$$

where the factor $\frac{v_j}{v_i}$ accounts for different group velocities. The meaning of $|t_{ij}|^2$ is the probability of scattering an incident wave Φ_i^{L} into a transmitted wave Φ_j^{R}. The number of contributing incident waves $n_{\text{waves}}^{\text{in}}$ is determined by the potential at the left boundary plane. Any solution with an energy E lower than E_{F} gives one incident wave. Analogously the number of outgoing waves $n_{\text{waves}}^{\text{out}}$ is determined at the right boundary plane. Thus in a symmetric setup with zero voltage bias one can expect $n_{\text{waves}}^{\text{in}} = n_{\text{waves}}^{\text{out}}$.

7.3 Generalized eigenstates

In a system with a discrete translational symmetry in z-direction, the eigenstates of the Hamiltonian can be described in terms of Bloch-states i.e.

$$\Psi_{\text{Bloch}}(\mathbf{r}_\parallel, z) = \mathbf{e}^{\mathrm{i}k_z z}\ \tilde{\Psi}_{\text{peri}}(\mathbf{r}_\parallel, z) \tag{7.25}$$

Consider the electronic state of an electron in a infinite crystal. The periodic boundary conditions requires us to choose k_z real valued so that the phase factor $\mathbf{e}^{\mathrm{i}k_z z}$ has the absolute value 1. This allows to normalize the wave function to the unit volume. However, the transport setup foresees semi-infinite leads on each side of the junction. For the left (right) electrode also exponentially growing (decaying) states can be normalized so that k_z may be complex. The (generalized) eigenstates corresponding to complex k_z values are usually connected to the *complex band structure*. Figure 7.2 depicts an evanescent wave of the right electrode schematically.

7.4 Jellium approximation

The jellium model is a very simple, but also very rough approximation for a metal. The delocalized electronic states in bulk metallic material cause *screening*. This means that strong core potentials are screened and so create a relatively smooth background potential. In the limit of maximal screening, the localized positive charge of the cores is approximated by a homogeneous background charge distributed in space. This produces a maximally smooth local effective potential in the single-particle picture. One can imagine that this model will not reproduce the same characteristic wave functions as the original bulk material. Analogously, the chemical bonds to it will suffer from the loss of structure and the gain of symmetry.

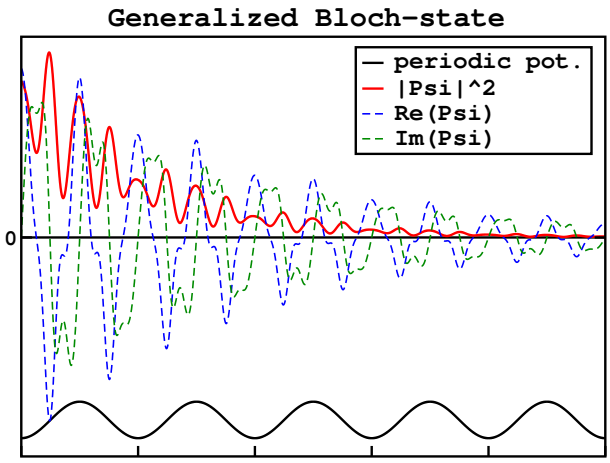

Figure 7.2: Sketch of a generalized Bloch-state. The electronic wave functions envelope is exponentially decaying. Such states can be normalized inside a half-infinite volume such as the right electrode.

Jellium as leads for transport calculations is of particular interest because its electronic structure can be described analytically. The crystalline structure given by the core positions gets lost due to the smearing. Consequently, a pure bulk jellium system has the full translational invariance and isotropy assuming an infinitely extended system. The eigensolutions of such a homogeneous electron gas are known to be plane waves, occupied up to the Fermi energy E_{F}. However, the solutions needed for the transport calculations outlined in Chapter 7.2 contain eigenstates (plane waves) and generalized eigenstates (exponentially growing or decaying waves). These can be expresses by

$$\Phi^{\mathrm{jellium}}(\mathbf{r}) = \mathbf{e}^{\mathrm{i}\vec{q}\mathbf{r}-\vec{\kappa}\mathbf{r}} \tag{7.26}$$

Discretizing the leads analogues to the junction region with peridic boundary condition for $\mathbf{k}_{\parallel}$ gives Bloch-states in plane. The exponentially growing or decaying factor is only relevant in the transport direction so that $\vec{\kappa}$ is assumed to consist of κ_z only.

$$\Phi^{L,R}([k], \mathbf{r}_{\parallel}) = \mathbf{e}^{\mathrm{i}\mathbf{k}_{\parallel}\mathbf{r}_{\parallel}} \cdot \mathbf{e}^{\mathrm{i}\mathbf{q}_z z_k} \cdot \mathbf{e}^{\pm\kappa_z z_k} \tag{7.27}$$

The local potential inside the junction region is subject to match the local potential of the leads at the boundary planes at z_{Lb} and z_{Rb}, respectively. The junction region is computed self-consistently in a so called *repeated slab* model i.e. with periodic boundary conditions in transport direction. Both sides of the junction region have to include some of the lead material. This causes the leads to interact with the junction and equally the junction to interact with the surface of the leads. If for example a molecule makes up the junction, the presence of a metal causes hybridization so that the molecular states are broadened. The surface of the lead breaks the translational symmetry so that it cannot be treated in a periodic calculation like regions deep inside the leads. The consequence are states localized at the surface. It has to be

ensured that the extend of the lead material included in the junction region is long enough to show bulk-like properties at the boundary planes. The screening effect in metals enables a rapid convergence but still there are effects arising from the calculation with a finite slab thickness that will be discussed later.
Another, very striking advantage of jellium for the transport calculations is that all the operators $\hat{B}^{(n)}_{[k]}$ in Chapter 7.2 are scalars i.e. scalar multiples of the unity operator. The scalar values are exactly the off-diagonal finite difference coefficients of the kinetic energy operator $\hat{B}^{(n)}_{[k]} = c^{(2)}_n \cdot \hat{1}$ and thus independent of the discretized z-position index k.

7.5 Computational costs

The important quantity for transport calculations is the Green-function $\hat{\mathcal{G}}(\mathbf{r}, \mathbf{r}', \mathbf{k}_\parallel, E)$. The spatial coordinates $\mathbf{r}$ and $\mathbf{r}'$ become vectors of indices $[i_x, i_y, i_z]$ and $[j_x, j_y, j_z]$, respectively due to the discretization, so the Green-function represented on the grid is $g([i_x, i_y, i_z], [j_x, j_y, j_z], [k_x, k_y]_\parallel, E)$. If the only nonlocal contribution from the Hamiltonian at the boundary planes is given by a short ranged finite difference formula, e.g. N_f=2 or N_f=1, for the kinetic energy in z-direction, the transport calculation demands only certain elements of the Green-function. A general form of equation (7.15) shows that the number required elements of $g([i_x, i_y, i_z], [j_x, j_y, j_z], [k_x, k_y]_\parallel, E)$ is given by $(2\,N_f N_x N_y)^2$. This means that the step from $N_f = 1$ to $N_f = 2$ brings the strongest relative increase of computational costs.
The single elements of the Green-function g are computed with a CG solver applying preconditioning for convergence acceleration. The residual norm

$$R_{\hat{\mathrm{G}}}(\mathbf{r}) = \int \left\{ \int \left[E\,\delta(\mathbf{r}'', \mathbf{r}') - \hat{H}_{\mathbf{k}_\parallel}(\mathbf{r}'', \mathbf{r}') \right] \hat{G}(\mathbf{r}', \mathbf{r}, \mathbf{k}_\parallel, E) \mathrm{d}\mathbf{r}' - \delta(\mathbf{r}'', \mathbf{r}) \right\}^2 \mathrm{d}\mathbf{r}'' \quad (7.28)$$

is minimized for all discretized vectors $\mathbf{r}$ in the first and last N_f x-y-planes, i.e. $2\,N_f N_x N_y$ vectors. Presumably, some computational effort can be saved by a clever guess for the initial Green-function that is required to start the iterative algorithm. A good guess would be

$$\hat{\mathcal{G}}_{\mathrm{init}}(\mathbf{r}, \mathbf{r}', \mathbf{k}_\parallel, E) = \sum_i^{N_{\mathrm{bands}}} \frac{\Psi^{(i)}_{\mathbf{k}_\parallel}(\mathbf{r}) \Psi^{(i)}_{\mathbf{k}_\parallel}(\mathbf{r}')}{E - \epsilon^{(i)}_{\mathbf{k}_\parallel}} \quad (7.29)$$

which should be a good approximation even for a finite number of computed states N_{bands}, where i is a band index, also including spin if spin is considered.

8 Molecular Transport Results

My investigation of the transport properties of terephthalic acid, embedded between two copper (110) surfaces, started at the isolated molecule in the gas phase, optimizing its structure and determining its electronic ground state structure. Then the one-sided adsorption and later on, the double adsorbed geometry are discussed. The conductance calculations have been performed using the jellium approximation. Applying jellium requires several aspects of convergence to be taken into account. I investigated the dependency of the equilibrium conductance on various parameters, especially the change of electron transmission when the Fermi level is shifted.

8.1 Isolated TPA

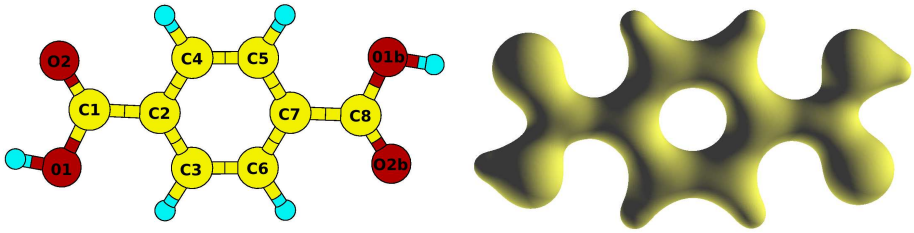

Figure 8.1: Terephthalic acid in the gas phase (isolated). The structure has been optimized in a $7.3 \times 10.3 \times 12.7\,\text{Å}^3$ box with finite boundary conditions. After a geometry optimization, the residual forces do not exceed $50\,\text{meV/Å}$. The density iso-surface is taken at $1.5\,e/\text{Å}^3$.

Terephthalic acid is a simple organic compound that consists of a benzene ring structure with two carboxylic functional groups in (1,4) position i.e. attached at opposite side of the ring (also called para-position). Figure 8.1 shows the structure visualized in a molecular viewer. The hexagonal ring of carbon atoms is known to be very stable due to the aromatic configuration. Each carbon atom is configured in a $\mathbf{sp}^2$-state, so that the third **p**-orbital can hybridize with the others to a delocalized π-state. This delocalized **p**-orbital has a nodal plane in the plane of the ring. That causes the density of this molecular orbital to be strongly localized in two torus structures, one above and one underneath the hexagonal ring of carbon cores. The D_{h6}-symmetry is

Bond Length (Å)	This work	Ref.[13]
O1-C1	1.34	1.390
O2-C1	1.20	1.291
C2-C1	1.46	1.480
C3-C2	1.38	1.417
C4-C2	1.38	1.415
C5-C4	1.37	1.405
O1b-C8	1.34	1.390
O2b-C8	1.20	1.291
C7-C8	1.46	1.480
C5-C7	1.38	1.417
C6-C7	1.38	1.415
C6-C3	1.37	1.405

Bond Angle (°)	This work	Ref.[13]
O1-C1-O2	122.6	121.7
O1-C1-C2	112.9	113.6
O2-C1-C2	124.4	124.7
C1-C2-C3	117.6	122.4
C1-C2-C4	121.5	119.3
C3-C2-C4	120.8	120.4
C2-C4-C5	119.4	
C2-C3-C6	119.8	120.3
C3-C6-C7	119.4	
C4-C5-C7	119.8	
C5-C7-C6	120.8	
C5-C7-C8	117.1	
C6-C7-C8	122.0	
C7-C8-O1b	124.2	
C7-C8-O2b	113.2	
O1b-C8-O2b	122.6	

Table 8.1: Structural data of terephthalic acid (TPA) in the gas phase. Bond length and angles are measured after a geometry optimization as described in Chapter 5.11. The calculation parameters are: cell extent $7.3 \times 10.3 \times 12.7\,\text{Å}^3$, finite boundary conditions and a force-cutoff $F_{\text{cutoff}} = 50\,\text{meV/Å}$, i.e. the atomic positions $\mathbf{R}^{(a)}$ are not updated after the determination of the electronic structure as soon as their forces $|\mathbf{F}^{(a)}| < F_{\text{cutoff}}$ fall below the cutoff.

broken due to the functional carboxylic group binding to the first and fourth carbon of the ring (labelled C2 and C7) atom replacing hydrogen atoms. The steric effect of them can be seen in a small deviation of the bond angles, listed in Table 8.1. The angles at C2 and C7 of the terephthalic acid deviate about 0.84° from the equilibrium angle of benzene which is exactly 120° due to its symmetry. This has been found in a geometry optimization of the isolated TPA structure in a $7.3 \times 10.3 \times 12.7\,\text{Å}^3$ unit cell with isolated boundary conditions and a grid spacing of $[0.152, 0.161, 0.159]$ Å. The forces have been relaxed below $F_{\text{cutoff}} = 50\,\text{meV/Å}$. The results have been found to agree qualitatively with the reference data from [13]. The bond angles differ only slightly whereas the bond lengths are systematically shorter. This is due to the usage of the P91-functional [2] in this work and the PBE96GGA-functional [25] in the reference.

This tiny change of the bond angle justifies the assumption that the electronic structure in the carbon ring has changed only slightly from the one of benzene. Figure 8.2 shows the density of the molecular state that has a strong contribution of **p**-orbitals. Additionally, hybridization with the states localized around the oxygen pairs occurs. However, the shape of the central cloud represents the π-conjugated orbital in

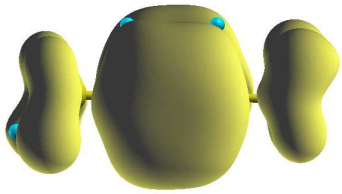

Figure 8.2: Iso-surface of a conjugated π-state. The nodal plane of the **p**-orbitals coincides with the plane of the carbon ring structure. Hybridization occurs also with the **p**-states of the oxygen pairs.

agreement with the prediction from benzene.

8.2 TPA on Cu(110) surface

The carboxylate group of terephthalic acid easily dissociates the hydrogen in order to bind to a metallic surface. The functional carboxylic group assumes a symmetric equilibrium structure after removing the hydrogen due to the gained mirror symmetry. Atodiresei *et al.* investigated the adsorption process of the carboxylic acid group on the basis of *ab inito* calculations for single formate molecules (CH_3COOH) [14] as well as for terephthalic acid itself [13]. The arrangement of the organic molecules on a Cu(110) surface is such that one carboxylic group couples to the outermost copper layer. This configuration was found more stable than adsorption at any hollow site of the (110)-surface. Each of the two oxygen atoms of the lower carboxylic group bind to one copper surface atom. The molecule arranges itself to be standing vertically on the surface [15].

The self assembly process is strongly controlled by the surface coverage. A set of terephthalic acid molecules (TPA) standing packed on the surface interact due to their small intermolecular distance. Their separation is induced by the surface structure. The equilibrium lattice constant of copper $a = 3.59\,\text{Å}$ forces the molecular axis to be separated by $3.59\,\text{Å} = a$ in x-direction and $5.08\,\text{Å} = a\sqrt{2}$ in y-direction so that a full coverage leads to repulsive forces between the hydrogen atoms. The effect is that the benzene ring is tilted with respect to the $(1\bar{1}0)$ direction [12]. At full coverage, i.e. every adsorption site is occupied, the torsion angle is 24.7 degrees [13], when the structure is relaxed.

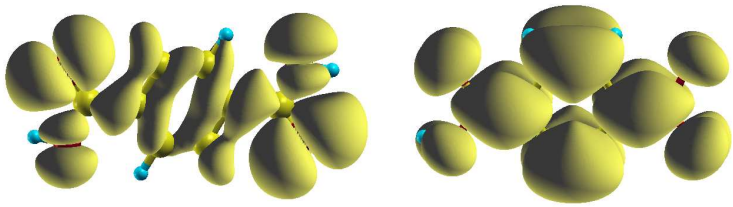

Figure 8.3: Isosurfaces at $0.2 \cdot 10^{-3}\, e/\text{Å}^3$ of the HOMO (left) and LUMO (right) Kohn-Sham states. The HOMO state shows mainly σ-bonds inside the carbon ring whereas the LUMO state consists of π-orbitals with a nodal plane that coincides with the plane of the molecule. The HOMO-LUMO gap is 3.66 eV (difference of Kohn-Sham energies).

8.3 TPA in the transport setup

Terephthalic acid in its one-sided adsorption geometry, as described in the previous Chapter, has been measured using scanning tunnelling microscopy (STM). This technique requires a conductive substrate and a metallic tip which is positioned close above the surface of the substrate. In this particular setup the tip approaches the upper end of the upright standing molecule. STM measurements produce a characteristic dependence of the tunnel current in dependence of the voltage, applied between tip and substrate, and the spatial separation between tip and molecule. Consider a tip that is brought close to upper end of the TPA molecule so that the upper carboxylic group binds to the closest atoms of the tip.

The self-assembled array of molecules can easily be calculated using periodic boundary conditions and one molecule in the unit cell. However, the tip approaching the molecule breaks the translational invariance so that periodic boundaries are not applicable any longer. A realistic model of a STM tip would require a huge super cell with many molecules and surface atoms because usual tip radii are larger than a hundred Å. Furthermore some vacuum between the periodic replicas of the tips would be necessary to come closer to the system of a single tip. Alternatively, an impurity calculation could treat the single tip over the surface. To simplify the problem, the tip has been replaced by a second copper (110) surface. The result is a symmetric setup of two surfaces enclosing the molecule as depicted in Figure 8.4. Note that this setup will not fully reproduce the results of STM measurements for various reasons. Copper is too flexible to produce a tip out of it; rather Tungsten works well and is used frequently. A major difference is also induced by the change of boundary conditions. The copper surface with its two-dimensional boundary conditions will

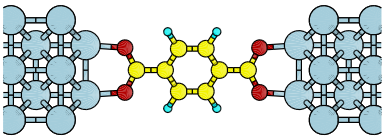

Figure 8.4: Terephthalic acid in the transport setup. The molecule is chemisorbed to both Cu (110) surfaces simultaneously. The coupling to both electrodes promises transport via the molecular states.

produce a different density of states than the tip which is expected to show finite size effects due to its small extent in the direction parallel to the surface.
In the process of the molecules chemisorption to the surface, the hybridization of the molecular states with the metallic states of the leads is of special interest. In particular the broadening of the molecular states is crucial for the transport mechanism. The effect of the molecule onto the surface and the effect of the surface onto the molecule can be considered relatively weak. This can be seen from the results of the projection method.

Consider the Kohn-Sham states $\left|\psi^{(j)}_{\text{junc}}\right\rangle$ of the junction containing the molecule and the surfaces. The total interaction can be called weak when these states separate into molecular states and electrode state. This can be observed in the projected density of states. The junction states are projected onto states of the molecule without electrodes $\left|\psi^{(i)}_{\text{mol}}\right\rangle$ and onto states of the electrode without a molecule $\left|\psi^{(i)}_{\text{elec}}\right\rangle$. The coefficients are used as weights for the particular state in the projected density of states (PDoS).

$$w^{(j)}_{\text{mol}} = \left\langle \psi^{(j)}_{\text{junc}} \right| \left[\sum_i \left| \psi^{(i)}_{\text{mol}} \right\rangle \left\langle \psi^{(i)}_{\text{mol}} \right| \right] \left| \psi^{(j)}_{\text{junc}} \right\rangle = \sum_i \left| \left\langle \psi^{(i)}_{\text{mol}} \middle| \psi^{(j)}_{\text{junc}} \right\rangle \right|^2 \tag{8.1}$$

and

$$w^{(j)}_{\text{elec}} = \left\langle \psi^{(j)}_{\text{junc}} \right| \left[\sum_i \left| \psi^{(i)}_{\text{elec}} \right\rangle \left\langle \psi^{(i)}_{\text{elec}} \right| \right] \left| \psi^{(j)}_{\text{junc}} \right\rangle = \sum_i \left| \left\langle \psi^{(i)}_{\text{elec}} \middle| \psi^{(j)}_{\text{junc}} \right\rangle \right|^2 \tag{8.2}$$

For a non-interacting system, the weights $w^{(j)}_{\text{elec}}$ and $w^{(j)}_{\text{mol}}$ must add up to unit for each state j. Figure 8.6 depicts the total density of states (weight 1) and the projected densities of states. The sum of both parts adds up to unity almost everywhere. Note

Direction	Length	Grid points	Grid spacing	Cutoff energy
x	3.59 Å	20	0.179 Å	83.3 Ry
y	5.08 Å	28	0.181 Å	81.7 Ry
z	21.4 Å	160	0.134 Å	155.4 Ry

k-point	in $\frac{2\pi}{L}$		Weight
0.00	0.00	0.00	1/16
0.25	0.00	0.00	2/16
0.50	0.00	0.00	1/16
0.00	0.25	0.00	2/16
0.25	0.25	0.00	2/16
0.50	0.25	0.00	2/16
0.00	0.50	0.00	1/16
0.25	0.50	0.00	2/16
0.50	0.50	0.00	1/16
0.25	-0.25	0.00	2/16

N_{atoms}	34
$N_{\text{electrons}}$	258
N_{bands}	144

Table 8.2: Details of the calculation. The grid spacings in the directions parallel to the surfaces have been chosen, according to the results of the convergence test, relatively small, because the number of required Green-function elements is proportional to the number of grid points in the x-y-plane. The **k**-point set has been chosen according to the Monkhorst-Pack[26] scheme $4\times4\times1$. N_{atoms} is the number of real atoms. It differs in those calculations where jellium has been used to replace the inner layers of the copper slab, but the total number of valence electrons is kept constant.

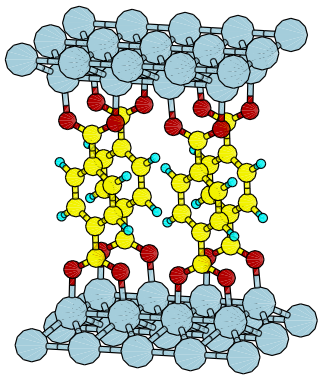

Figure 8.5: Periodic transport setup. A realistically extended surface has to be simulated in a periodic model. Choosing the smallest unit cell that accommodates one molecule leads to a small intermolecular separation. This causes the carbon rings to relax into an tilted equilibrium structure due to the repulsions of the hydrogen atoms. The super cell in this calculation is $3.59 \times 5.08\,\text{Å}^2$ and 21.4 Å in transport direction. A set of 2×2 super cells is shown.

that this does not mean, that states of the electrode and states of the molecule that have the the same energy do not hybridize, but rather it means that the hybrid states are very close to linear combinations of each components states. Thus the energy splitting is small.

As pointed out in Chapter 7.4, the transport calculations using jellium is much simpler and faster than the general case employing crystalline electrodes. Therefore the junction system must be adopted to the jellium leads. Especially the valence density and local potential of the junction region have to be continuous at the boundary planes. The first derivatives of the valence density and of the local potential have to vanish in order to find a smooth transition to the constant density and potential. Fortunately, this is an intrinsic feature of a mirror symmetric junction region. However, this goal can be reached by including some jellium into the junction region. As mentioned previously, also layers of real atoms have to be included there to model the surface structure. The transport setup has to be converged with respect to both, the number of atomic buffer layers and the length of the included jellium. Within this slice of jellium, the structured effect arising from the atomic potentials (local and non-local) has to vanish and adopt to the flat potential inside the semi-infinite electrode. The difficulty arising from the usage of jellium in combination with atomic buffer layers is to treat the interface right. The setup has a certain interface at the position of the jellium edge. The atomic buffer layers are, to produce no gap, situated such that the average density would be preserved i.e. the jellium edge is at a half a layer-layer distance from the first row of atomic positions. However there is a strong surface dipole which induces an unwanted interface between the jellium and the atomic buffer layers.

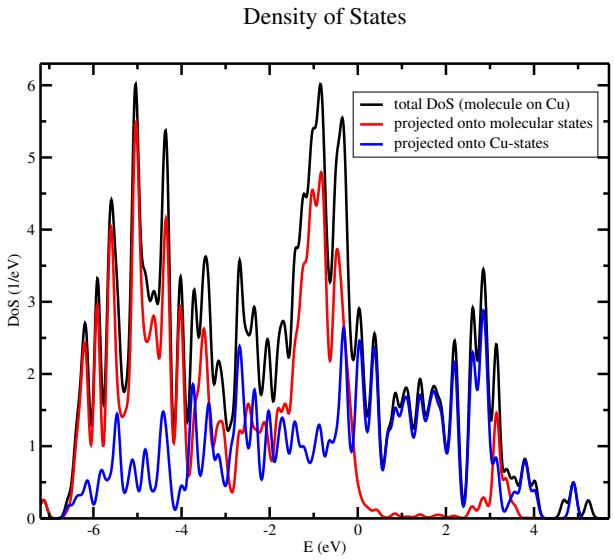

Figure 8.6: Projected density of states. The electronic structure of the molecule together with the junction is compared to the electronic structure of its components, the clean junction and the molecule only. Therefore, each state j of the junction is weighted with the expectation value of the projector onto the molecular state $w^{(j)}_{\mathrm{mol}} = \sum_i |\left\langle \psi^{(i)}_{\mathrm{mol}} \middle| \psi^{(j)}_{\mathrm{junc}} \right\rangle|^2$ and the expectation value of the projector onto the electrode states $w^{(j)}_{\mathrm{elec}} = \sum_i |\left\langle \psi^{(i)}_{\mathrm{elec}} \middle| \psi^{(j)}_{\mathrm{junc}} \right\rangle|^2$, respectively. The same boundary conditions and **k**-point sets are applied to all three setups. It has been checked that the density of states (DoS) of the junction containing the molecule deviates only slightly from the sum of the projected densities of states i.e. $w^{(j)}_{\mathrm{elec}} + w^{(j)}_{\mathrm{mol}} \approx 1$ for all j.

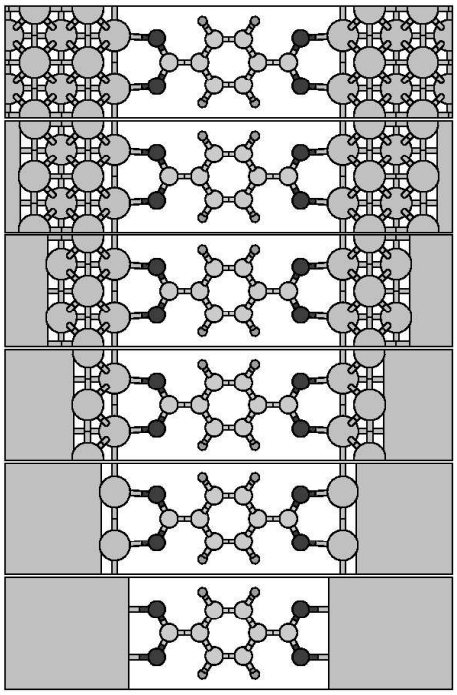

$N_{\text{buffer layers}}$	q_{jellium}	$G\,/\,G_0$
$4\frac{1}{2}$	$0\,e$	-
4	$22\,e$	$0.16 \cdot 10^{-4}$
3	$66\,e$	$0.24 \cdot 10^{-4}$
2	$110\,e$	$0.53 \cdot 10^{-4}$
1	$154\,e$	$0.58 \cdot 10^{-3}$
0	$198\,e$	$0.58 \cdot 10^{-1}$

Figure 8.7: Buffer layers of copper atoms. The electronic structure and total conductivity at the Γ-point have been calculated with different numbers of atomic buffer layers. The effect of the (110) surface structure can not be reproduced by a flat jellium surface (lowest configuration without atomic buffer layers). However the combination of copper atoms and jellium bares severe difficulties. The conduction is higher not including atomic buffer layers, but the density plots show, that the binding of the molecule to the textureless and flat jellium surface does not reproduce the effect of a (110) surface.

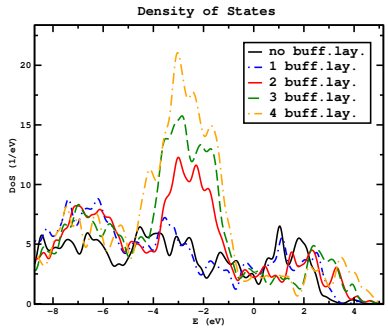

Figure 8.8: Density of states with different numbers of buffer layers. The high accumulation of states in the interval of $[-4.0, -1.0]$ eV are the strongly localized **d**-states of the real atoms. This explains the disappearing of the states when less atomic buffer layers but more jellium is used which does, due to the smooth potential, not produce localized states.

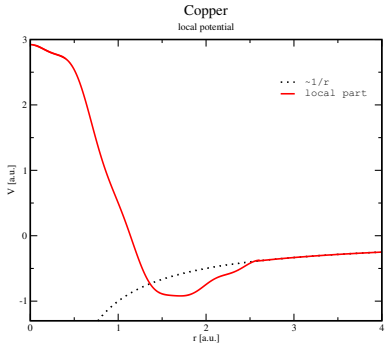

Figure 8.9: Local pseudopotential for copper. The localized **d**-states are treated as core states. The integrated effective potential may be constructed to be only local, i.e. no non-local projection of the Kleinmann-Bylander pseudopotential form is needed.

8.4 Friedel oscillations in jellium

A jellium surface creates a surface dipole due to its electronic states leaking out of the confining potential well. The constant electrical field of this dipole is screened by the charges underneath the surface which leads to Friedel oscillations. These in principle are a natural phenomenon but it has to be ensured that the oscillations of the surface have decayed in the center of a slab of finite thickness if we want to match bulk to it. Otherwise a finite size effect comes into play. If the charge density has not converged to a constant, bulk-like charge density but rather oscillates, the local effective potential oscillates as well. This is crucial for matching it to the constant potential of the electrode.

The valence electron configuration of copper is [Ar] $3\mathbf{d}^{10}$ $4\mathbf{s}^{1}$. The **d**-electrons are well localized around the core whereas the spatial extent of the 4**s**-wave function is

much larger. There are two ways to represent copper atoms by pseudopotentials. One way is using a nonlocal pseudopotential with **s**, **p** and **d**-states treating all 11 valence electrons ($Cu^{(10+1)}$). The alternative is integrating out the effect of the **d**-states using a local potential for the 4**s**-state only ($Cu^{(1)}$). This local potential is depicted in Figure 8.9.
The jellium charge density in the transport setup has to coincide with the average valence charge density of crystalline copper. For $Cu^{(10+1)}$ the density in the electrodes is $\varrho^{(10+1)} = 0.91\, e/\text{Å}^3$ while it is less by factor 11 for the **s**-electron only $\varrho^{(1)} = 0.083\, e/\text{Å}^3$.

The advantage of the local potential with only one valence electron per copper atom is in first place the relatively small total number of valence electrons in the system. Additionally, a pure local potential in the Hamiltonian is cheaper to apply to a wave function since it does not require nonlocal projection operations as described in Chapter 4. The disadvantage is the reduced screening effect. In the model of the single **s**-electron as valence charge, the charge density is not sufficient to damp these oscillations down. Figure 8.10 depicts that in particular. The results show that even a much longer electrode, with the same valence electron density and thus more charge in total, is not effectual to remove the finite size residuals.
A higher valence density allows more efficient screening so that the oscillations decay rather rapidly into the jellium. For these reasons the $Cu^{(10+1)}$ has to be applied for the buffer layers and $\varrho^{(10+1)}$ as valence density of the jellium electrodes. Figure 8.8 shows this for different numbers of buffer layers. It can be observed that the plane-integrated density converges to the constant 'bulk' value about one layer width behind the jellium edge. Note that the jellium surface is situated behind the buffer layers of real atoms. The position of the edge has been chosen in the center between the real atomic layer and the replaced atomic layer. It can be observed in Figure 8.11, that the plane integrated density has a minimum at the jellium edge, if there are atomic buffer layers separating the jellium from the molecule. For a pure jellium surface (i.e. no buffer layers), the plane-integrated density deviates strongly from the density of the atomic surface. This explains the enormous deviations of conductance values and other properties. The characteristic structure of the (110) surface is not reproduced by a flat jellium surface.

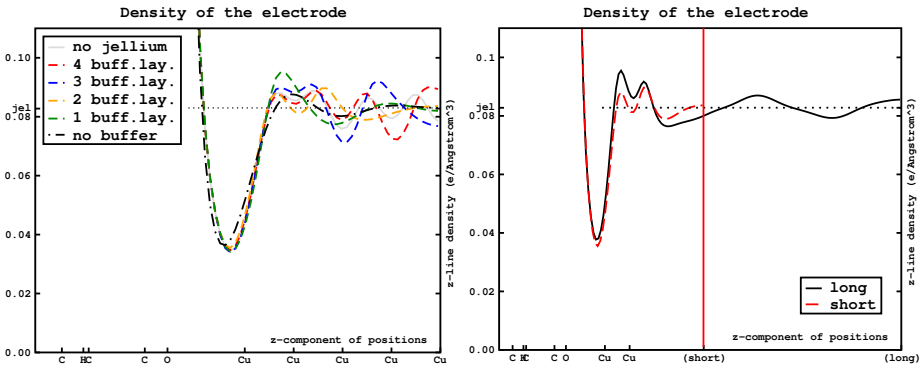

Figure 8.10: Valence density averaged over the x-y-direction. The $Cu^{(1)}$ model (copper with only the 4**s** electron) shows very large Friedel-oscillations (left hand side). Even for a much thicker slab size the density does not converge to a constant (right side). The low valence density does not screen the surface effect efficiently.

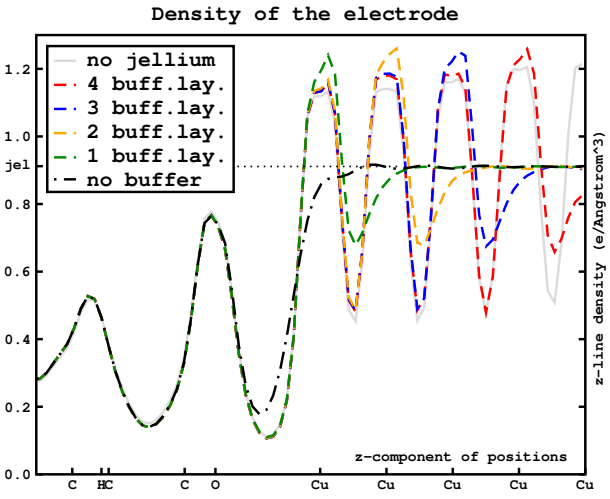

Figure 8.11: Valence density averaged over the x-y-direction. $Cu^{(11)}$, i.e. copper with 11 valence electrons suppresses the Friedel-oscillations strongly.

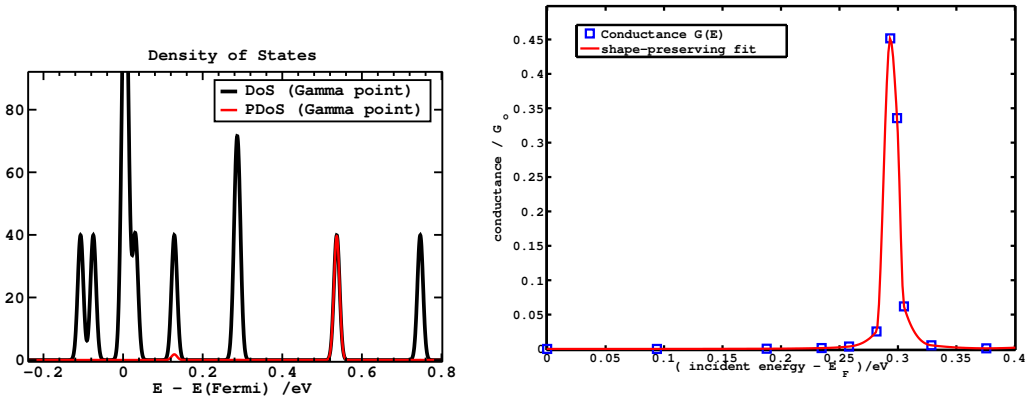

Figure 8.12: Comparison of the density of states and transmission $\mathcal{T}(E)$ above the Fermi level. The total conductance at the Γ-point (right plot) shows a significant similarity to the corresponding density of states. The finite width of the resonance peak is due to the broadened molecular state, whereas the width in the density of states is artificial.

8.5 Energy dependence

A main purpose of the transport calculation is to determine the total conductivity of a junction setup. For simplicity the Green-function $\mathcal{G}(E)$ is only calculated at the Fermi level i.e. $E = E_{\mathrm{F}}$ in equation (7.9). This provides the conductance value at the Fermi level and so the limit of zero voltage. In order to investigate the sensitivity of the total conductance $G(E)$ to changes of the Fermi level, the total transmission $\mathcal{T}(E)$ has been evaluated at a set of different energies above E_{F} for the transport setup of terephthalic acid (TPA). A very simple model predicts that the transmission $\mathcal{T}(E)$ depends only on the density of states at the particular energy E. Therefore, it is supposed to show a resonance when E matches the eigenenergy of a molecular state ϵ_i.

The corresponding distribution function for the density of states of a molecule is a set of δ-functions, each centered at a molecular eigenenergy. However, when the continuum of states of the electrode in the transport setup hybridizes with the molecule, its states will broaden i.e. the molecular states appear in the density of states as a peak with a finite width instead of a sharp delta-function. In practice, every calculation with a finite number of **k**-points will give discrete set of states instead of a continuum. The peaks will therefore split into a set of peaks, localized within the range of the energy broadening. This broadening should then be visible also in the width of the resonance of the transmission $\mathcal{T}(E)$.

We can expect of a symmetric transport setup that the molecular states cause a high transmission probability by coupling to both electrodes simultaneously and so

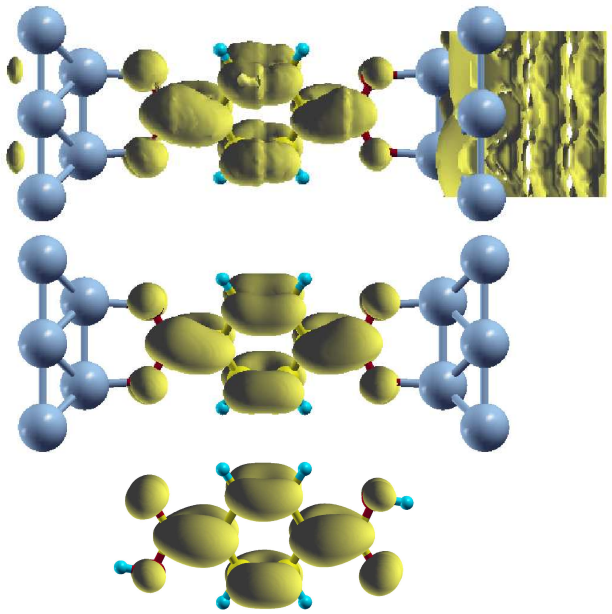

Figure 8.13: Comparison of the transmission channel and molecular states. The first iso-surface is the transmission channel wave function at +0.3 eV above the Fermi level. The second iso-surface is the state of the junction region at the corresponding energy. It is localized 99.3% on the molecule. The third state is the LUMO orbital of the isolated TPA molecule. All three structure show a similarity in their behavior around the carbon ring.

mediating incident electrons from the left electrode via the molecule into the right electrode. This has been found for the first resonance level above the Fermi energy E_{F}.

The transmission $\mathcal{T}(E)$ has been measured at a set of energy values above the Fermi level, especially at the eigenenergy of the LUMO state, which is expected to provide a non-vanishing total conductance. Figure 8.12 gives a comparison between the density of states and the total transmission $\mathcal{T}(E)$, both evaluated at the Γ-point. The resonance peak is centered at 0.29 eV. The density of states shows a single state at 0.29 eV but the projected density of states (PDoS) vanishes there. This means that this particular state has no weight on the molecule. Visualization of the density of this state shows, that it is bulk state inside the copper electrode. The next highest state at 0.54 eV however, is strongly localized on the molecule. This is a proper candidate for causing the high transmission. The energy shift of 0.25 eV can be explained by the different boundary conditions of the Hamiltonian. The Hamiltonian of the scattering region is determined self consistently in a electronic structure calculation using periodic boundary conditions. The Hamiltonian to be inverted in order to find the Green-function though, does not include this periodicity.

Figure 8.13 illustrates the similarity of the transmission channel at 0.29 eV above

the Fermi level and the molecular state at 0.54 eV. The transmission channel is the scattering wave function that is found by matching the incident wave to the reflected and transmitted wave. The third iso-surface picture is the LUMO state of the isolated molecule.

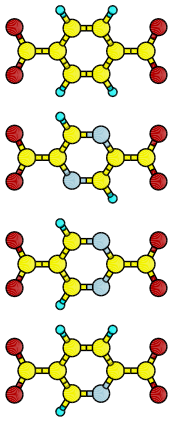

Name	N position	$G(E_F)/G_0$	$E_{LUMO} - E_F$
benzene-1,4-dicarboxylic acid	–	$53.0 \cdot 10^{-6}$	0.376 eV
pyrazine-2,5-dicarboxylic acid	para	$5.1 \cdot 10^{-6}$	0.405 eV
pyrimidine-2,5-dicarboxylic acid	meta	$22.7 \cdot 10^{-6}$	0.369 eV
pyridine-2,5-dicarboxylic acid	1	$104.4 \cdot 10^{-6}$	0.388 eV

Figure 8.14: Doping of the benzene ring with nitrogen. The names change according to the IUPAC nomenclature rules. Starting from terephthalic acid the carbon atoms C3, C4, C5 and C6 (comp. Figure 8.1) are systematically replaced by nitrogen. Simultaneously one hydrogen atom is removed so that the total number of valence electrons is unchanged. The aromatic character of the π-conjugated electronic structure within the ring is preserved.

8.6 Nitrogen doping

Terephthalic acid can be also be called **benzene-1,4-dicarboxylic acid**. Replacing some carbon atoms in the benzene ring creates new compounds. The effect of three different configurations of nitrogen in the benzene ring has been investigated by calculating the electronic structure and measuring the total conductance of these setups.

The effect of nitrogen doping is strongly localized in the ring structure of the molecule. This can bee seen from the difference of valence charges in Figure 8.15. Also the density of states is hardly affected close to the Fermi level. Figure 8.16

All values for the equilibrium conductance are very small compared to the quantum conductance G_0, which is the theoretical value for one conducting channel. This is an effect from the insulating nature of all these molecules. More interesting results could in principle be gained from the investigation of $G(E)$ like shown in Chapter 8.5. The important quantities then would be the position and width of the resonance peaks closest to the Fermi level.

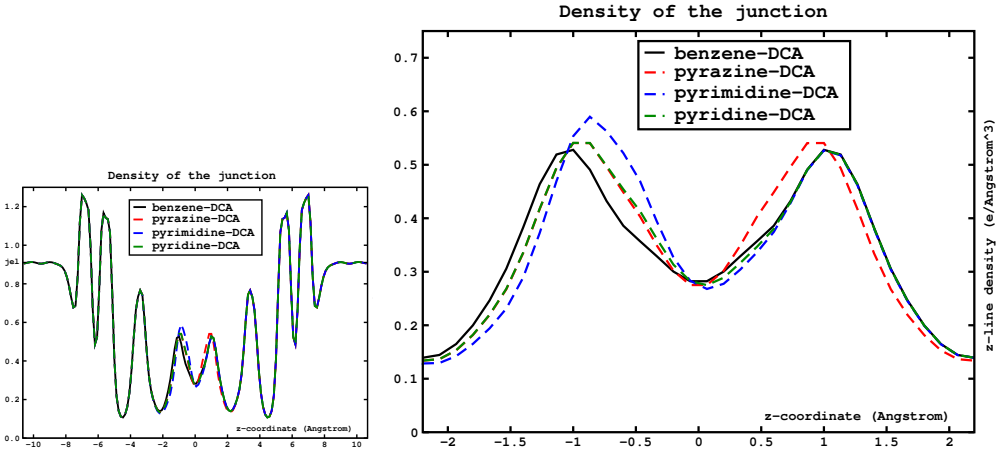

Figure 8.15: Comparison of the plane-integrated total valence densities for the four different molecules. The right plot is a closeup on the region of the ring. The effect that can be observed at the nitrogen sites is a slightly more localized valence charge density.

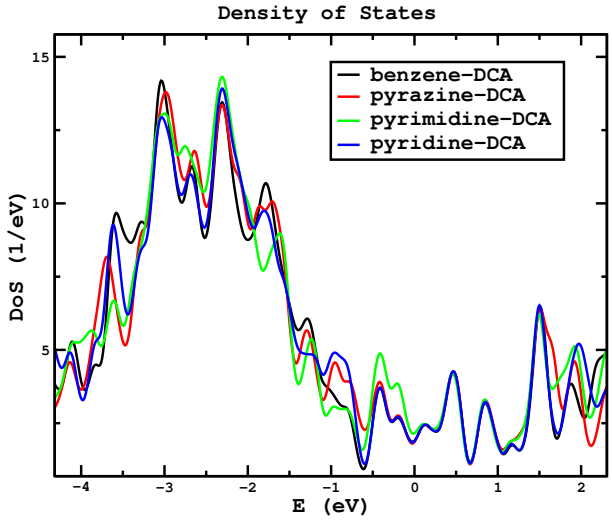

Figure 8.16: Density of KS-states around the Fermi-level. The deviations in the total density of states induced by nitrogen replacement in the benzene ring clearly affect only molecular states. The states above the Fermi level ($E_{\mathrm{F}} = 0.0$) are contributions of the electrode because all four molecules show a large HOMO-LUMO gap. This has been shown by the projected density of states for benzene-dicarboxylic acid (TPA).

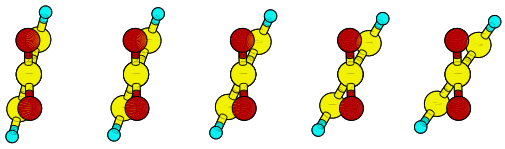

Figure 8.17: Tilted TPA molecules. The structures and conductivities have been investigated at 14.7, 19.7, 24.7, 29.7 and 34.7 degrees tilting against the $(1\bar{1}0)$ direction. The geometries have not been optimized.

$\Delta\phi$/degree	ϕ/degree	$G(\phi)/G_0$	ΔE_{tot}	$E_{\text{LUMO}} - E_{\text{F}}$
-10	14.7	$74.6 \cdot 10^{-6}$	0.583 eV	0.3698 eV
-5	19.7	$58.5 \cdot 10^{-6}$	0.122 eV	0.3729 eV
0	24.7	$52.8 \cdot 10^{-6}$	0.000 eV	0.3757 eV
5	29.7	$49.7 \cdot 10^{-6}$	0.035 eV	0.3782 eV
10	34.7	$43.9 \cdot 10^{-6}$	0.149 eV	0.3806 eV

Table 8.3: Data for different tilting angles. The conduction values at the Fermi level are all in the insolating regime. However, a trend can be observed. The less the molecule is tilted, the higher grows the conduction value and the closer comes the LUMO energy to the Fermi level.

8.7 Mechanical coupling

The equilibrium structure of the TPA molecule on a Cu(110) surface shows a tilting of the benzene ring with respect to the $(1\bar{1}0)$ direction. This is an effect of the intermolecular repulsion at full coverage (each molecules occupies exactly two surface unit cells of 3.59 Å × 2.54 Å). This angle has been driven away from its equilibrium value to see the response of the electronic structure and thus of the conductivity. Unfortunately, the setup is insulating, so that the effect is tiny. In Figure 8.18, a trend towards higher conductivity values can be observed, when the structure approaches the straight, planar configuration. Simultaneously, the level of the LUMO state at the Γ-point with respect to the Fermi energy shows a trend upwards. The sign of this change agrees with the variation of the conductivity. All out-of-equilibrium configurations have, as expected, a higher total energy than the equilibrium structure, but the minimum seems to be strongly asymmetric (compare ΔE_{tot} in Table 8.3).
A very interesting case study would be the $\phi = 0$ state. This configuration shows a higher symmetry than the tilted systems. Due to the repulsion of the molecules among each other, this configuration cannot be computed at full surface coverage. The hydrogen atoms are then brought too close leading to instability. The computation at quarter coverage, however, requires a super cell four times as large.

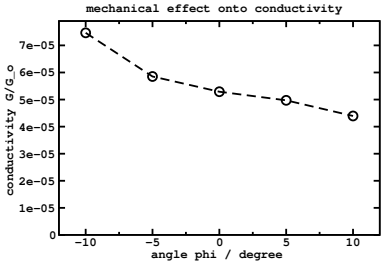

Figure 8.18: Conductivity in dependence of the angle. The molecule which is tilted by 24.7 degrees in equilibrium has been forced into a atomic configurations with smaller and larger values. At each step, the electronic structure has been determined and consequent to it, the conductivity at the Γ-point.

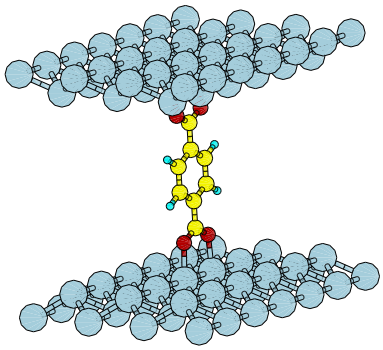

Figure 8.19: Transport setup at 1/4-coverage. Due to the sparse coverage, the intermolecular interaction can be neglected. Especially the transmission value at $\phi = 0.0$, i.e. no tilted ring structure, can then be investigated. This case is of particular interest because it provides a higher symmetry. However, the unit cell of this setup is twice as large in x- and y-direction as in the case of full coverage (compare Figure 8.5 and its setup). This leads to a much higher effort in the electronic structure computation and in the transport calculation.

9 Conclusions

In this thesis I applied a newly developed real-space finite difference method to investigate the electronic structure and transport properties of terephthalic acid within the framework of the density functional theory. We found out that such a real space method provides an excellent tool to investigate systems in low and broken structural symmetry and large number of atoms, situations which occur with increasing frequency in nanoscience. Especially the representation on equidistant grids and the usage of pseudopotentials and iterative methods allows a simple and most efficient parallelization. Thus this method opens a new vista using massively parallel supercomputers to challenge the system sizes.
The transport formalism, introduced in this work, combining first-principles calculations with the Landauer-Büttiker formulation of quantum transport extends the electronic structure calculation and allows to study the conductivity on an *ab initio* basis. Electronic transport calculations in the quantum regime can so be applied to realistic setups. This has been shown for terephthalic acid between two copper (110) surfaces. We are aware that several important aspects of the electron transport across a molecule has been neglected in this Diplomathesis, which included the aspects of non-equilibrium transport, inelastic effects such as coupling of transport to molecular vibrations as well as possible Coulomb blockade effects. All these effects may be included in the future.

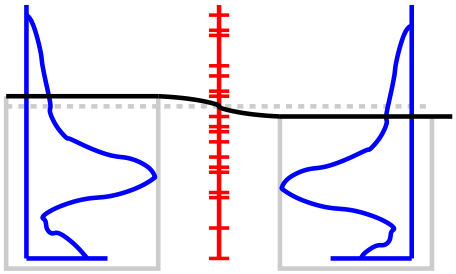

Figure 9.1: Sketch of a molecular switch. Two electrodes provide a continuous spectrum of states whereas the molecule in the junction shows discrete and localized states. Molecular states that lie between the Fermi levels of left and right electrode cause single conduction channels to open. If the alignment of a molecular spectrum to the Fermi level of the electrodes can be tuned, this setup is a candidate for a molecular switch or transistor.

In this thesis I investigated the electronic structure of the terephthalic acid molecule between the copper (110) leads. To simplify the transport calculations we replaced

parts of the copper leads by jellium electrodes. As a result I found that the insulating nature of the molecule is dominant when the surfaces are fully covered with adsorbed molecules. However, a promising application for molecular junctions is a nano switch. The molecule is an insulator by default but shifting the molecular states with respect to the electrodes' Fermi energies results in drastic changes of the electron transmission. A third 'gate' electrode in the setup which controls the molecular level shift over electrostatic interaction would provide this possibility. The conduction channels opening up from this manipulation give rise to a quantized conductance behavior. A nano device for digital data processing could exploit this feature properly.

A Appendix

A.1 Conjugate gradients

The CG method is a sophisticated way to find the solution of a set of linear equations $\hat{A}\,|x\rangle = |b\rangle$. Therefore a residual norm is defined which is to be minimized iteratively. The residual vector is

$$|r_m\rangle = |b\rangle - \hat{A}\,|x_m\rangle \tag{A.1}$$

and the residual norm

$$R_m = \langle r_m|\, r_m\rangle \tag{A.2}$$

The function R is quadratic in the components of x so the best search direction $|p\rangle$ from a starting vector $|x_0\rangle$ is according to the steepest descent algorithm a scalar multiple of $|r_0\rangle$.

$$|p_0\rangle = |r_0\rangle \tag{A.3}$$

now do iteratively:

$$|x_{m+1}\rangle = |x_m\rangle + \frac{R_m}{\langle p_m|\,\hat{A}\,|p_m\rangle}\,|p_m\rangle \tag{A.4}$$

$$|r_{m+1}\rangle = |b\rangle - \hat{A}\,|x_{m+1}\rangle \tag{A.5}$$

$$R_{m+1} = \langle r_{m+1}|\, r_{m+1}\rangle \tag{A.6}$$

$$|p_{m+1}\rangle = |r_{m+1}\rangle + \frac{R_{m+1}}{R_m}\,|p_m\rangle \tag{A.7}$$

until R_m has converged below a given threshold that determines the accuracy of the result vector $|x_m\rangle$. It can be seen that the new search direction always contains a fraction of $\frac{R_{m+1}}{R_m}$ of the old search direction. This can be understood as some kind of memory. Setting this fraction to zero gives back the SD algorithm (and $|p\rangle$ would be dispensable). In real CG minimizations the method can be stuck in a saddle point. Then a restart i.e. one SD step may help to get towards the minimum again.

A.2 Transport formalism

The general expressions for the equations (7.11),(7.12) and (7.13) in Chapter 7.2 are given by

$$\hat{H}_{\mathrm{LS}}^{\dagger} = \begin{pmatrix} \cdots & 0 & \hat{B}_{[1-N_f]}^{(-N_f)} & \cdots & \cdots & \cdots & \hat{B}_{[0]}^{(-1)} \\ & \cdots & 0 & \hat{B}_{[2-N_f]}^{(-N_f)} & \cdots & \cdots & \hat{B}_{[0]}^{(-2)} \\ & & & \ddots & \ddots & & \vdots \\ & & & \cdots & 0 & \hat{B}_{[-1]}^{(-N_f)} & \hat{B}_{[0]}^{(-N_f+1)} \\ & & & & \cdots & 0 & \hat{B}_{[0]}^{(-N_f)} \\ & & & & & \cdots & 0 \\ 0 & & & & & & \vdots \end{pmatrix}, \tag{A.8}$$

$$\hat{H}_{\mathrm{SR}} = \begin{pmatrix} \vdots & & & & & & 0 \\ 0 & \cdots & & & & & \\ \hat{B}_{[n_z-(N_f-1)]}^{(N_f)} & 0 & \cdots & & & & \\ \hat{B}_{[n_z-(N_f-2)]}^{(N_f-1)} & \hat{B}_{[n_z-(N_f-2)]}^{(N_f)} & 0 & \cdots & & & \\ \vdots & & \ddots & \ddots & & & \\ \hat{B}_{[n_z-1]}^{(2)} & \cdots & \cdots & \hat{B}_{[n_z-1]}^{(N_f)} & 0 & \cdots & \\ \hat{B}_{[n_z]}^{(1)} & \cdots & \cdots & \cdots & \hat{B}_{[n_z]}^{(N_f)} & 0 & \cdots \end{pmatrix} \tag{A.9}$$

and

$$\hat{H}_{\mathrm{S}} = \begin{pmatrix} \hat{H}_{[1]} & \hat{B}_{[1]}^{(1)} & \cdots & \hat{B}_{[1]}^{(N_f)} & & & & & & 0 \\ \hat{B}_{[1]}^{(-1)} & \hat{H}_{[2]} & \cdots & \hat{B}_{[2]}^{(N_f-1)} & \hat{B}_{[2]}^{(N_f)} & & & & & \\ \vdots & & \ddots & & & \ddots & & & & \\ \hat{B}_{[1]}^{(-N_f)} & \cdots & \cdots & \hat{H}_{[1+N_f]} & \cdots & \cdots & \hat{B}_{[1+N_f]}^{(N_f)} & & & \\ & \ddots & & & \ddots & & & \ddots & & \\ & & \hat{B}_{[n_z-2N_f]}^{(-N_f)} & \cdots & \cdots & \hat{H}_{[n_z-N_f]} & \cdots & \cdots & \hat{B}_{[n_z-N_f]}^{(N_f)} & \\ & & & \ddots & & & \ddots & & \vdots & \\ & & & & \hat{B}_{[n_z-1-N_f]}^{(-N_f)} & \hat{B}_{[n_z-N_f]}^{(-N_f+1)} & \cdots & \hat{H}_{[n_z-1]} & \hat{B}_{[n_z-1]}^{(1)} & \\ 0 & & & & & \hat{B}_{[n_z-N_f]}^{(-N_f)} & \cdots & \hat{B}_{[n_z-1]}^{(-1)} & \hat{H}_{[n_z]} & \end{pmatrix} \tag{A.10}$$

Equation (7.22) is written in general form as

$$\begin{pmatrix} \psi_{[1]} \\ \vdots \\ \psi_{[1+N_f]} \\ \psi_{[n_z-N_f]} \\ \vdots \\ \psi_{[n_z]} \end{pmatrix} = \begin{pmatrix} \hat{\mathcal{G}}_{[1,1]} & \cdots & \hat{\mathcal{G}}_{[1,1+N_f]} & \hat{\mathcal{G}}_{[1,n_z-N_f]} & \cdots & \hat{\mathcal{G}}_{[1,n_z]} \\ \vdots & \ddots & \vdots & \vdots & & \vdots \\ \hat{\mathcal{G}}_{[1+N_f,1]} & \cdots & \hat{\mathcal{G}}_{[1+N_f,1+N_f]} & \hat{\mathcal{G}}_{[1+N_f,n_z-N_f]} & \cdots & \hat{\mathcal{G}}_{[1+N_f,n_z]} \\ \hat{\mathcal{G}}_{[n_z-N_f,1]} & \cdots & \hat{\mathcal{G}}_{[n_z-N_f,1+N_f]} & \hat{\mathcal{G}}_{[n_z-N_f,n_z-N_f]} & \cdots & \hat{\mathcal{G}}_{[n_z-N_f,n_z]} \\ \vdots & & \vdots & \vdots & \ddots & \vdots \\ \hat{\mathcal{G}}_{[n_z,1]} & \cdots & \hat{\mathcal{G}}_{[n_z,1+N_f]} & \hat{\mathcal{G}}_{[n_z,n_z-N_f]} & \cdots & \hat{\mathcal{G}}_{[n_z,n_z]} \end{pmatrix} \times \cdots \tag{A.11}$$

$$\cdots \begin{pmatrix} \hat{B}^{(-N_f)}_{[1-N_f]}\psi_{[1-N_f]} + \cdots + \hat{B}^{(-1)}_{[0]}\psi_{[0]} \\ \vdots \\ \hat{B}^{(-N_f)}_{[0]}\psi_{[0]} \\ \hat{B}^{(N_f)}_{[n_z-(N_f-1)]}\psi_{[n_z+1]} \\ \vdots \\ \hat{B}^{(1)}_{[n_z]}\psi_{[n_z+1]} + \cdots + \hat{B}^{(N_f)}_{[n_z]}\psi_{[n_z+N_f]} \end{pmatrix}.$$

A.3 Code modules

The electronic structure code can be explained in a modular scheme as follows.

```
KK4                    main            Main program
 +-ARG                 arguments       Command line arguments
 |  +-DOC              documentation   Internal documentation
 +-INP                 input           Input processing
 +-ATM                 atoms           Atomic information
 +-KPT                 kpoints         K-point information
 +-PAR                 params          Parameters for everything
 |  +-RNK              ranks           MPI-Communicators for parallelization
 |  +-KPP              kparallel       K-point parallelization
 +-MDY                 moldyn          Molecular dynamics
 |  +-PRE              prepare         Initial wave functions
 |  |  +-PDD           pseudodata      Atomic species pseudopotential data
 |  |  +-WFS           wavefunctions   Wave functions
 |  |  +-DNS           density         Densities
 |  +-SCF              selfcon         Self consistency
 |  |  +-PSD           pseudo          Pseudo potential preparator
 |  |  |  +-PDD        pseudodata      Atomic species pseudopotential data
 |  |  |  +-PRJ        projector       Nonlocal projectors
 |  |  |  +-POT        potential       Local potentials
 |  |  |  +-FZC        fuzzycells      Fuzzy cells
 |  |  |  +-EWA        ewald           Ewald summations
 |  |  +-POT           potentials      Local potentials
 |  |  |  +-BND        boundary        Boundary conditions for the Hartree potential
 |  |  |  +-CGR        congradient     Conjugate gradient
 |  |  |  |  +-LPL     laplace         Laplace operator and parallelization
 |  |  |  |  |  +-FDF  finitediff      Finite difference coefficients
 |  |  |  +-DFT        denfunctional   Density functionals
 |  |  +-SDA           sdescent        SD/CG eigensolver
 |  |  |  +-WFS        wavefunctions   Wave functions
 |  |  |  +-HMT        hamiltonian     Hamiltonian
 |  |  |  |  +-FDF     finitediff      Finite difference coefficients
 |  |  |  |  +-OVL     overlap         Kinetic energy parallelization
 |  |  |  |  +-POT     potentials      Local potentials
 |  |  |  |  +-PRJ     projector       Nonlocal projectors
 |  |  +-BMX           broyden         Density mixing
 |  |  |  +-DNS        density         Densities
 |  |  +-FRC           force           Force calculation
 |  |  |  +-FDF        finitediff      Finite difference coefficients
 |  |  |  +-WFS        wavefunctions   Wave functions
 |  |  |  +-POT        potentials      Local potentials
 |  |  |  +-PRJ        projector       Nonlocal projectors
 |  |  +-EWA           ewald           Ewald summations
 |  +-PIO              parallelio      Parallel input/output
 |  +-DSP              display         Display results
 +-BST                 bstructure      Band structure
 +-DSP                 display         Display results
 +-OUT                 output          Output units, files
```

Bibliography

[1] W. Kohn and L. J. Sham.
Self-consistent equations including exchange and correlation effects.
Phys. Rev., 140:A1133, 1965.

[2] J. P. Perdew, and A. Zunger.
Self-Interaction Correction to Density-Functional Approximations for Many-Electron Systems.
Phys. Rev. B, 23:5048–5079, 1981.

[3] R. Waser (ed.).
Nanoelectronics and Information Technology.
Wiley-VCH, Weinheim, 2003.

[4] K. Hirose, T. Ono, Y.Fujimoto, and Sh. Tsukamoto.
First-Principles Calculations in Real-Space Formalism.
Imperial College Press, London, 2005.

[5] L. Kleinman, and D. M. Bylander.
Efficacious Form for Model Pseudopotentials.
Phys. Rev. Lett., 48:1425, 1982.

[6] G.B. Bachelet, D. R. Hamann, and M. Schlüter.
Pseudopotentials that work: From H to Pu.
Phys. Rev. B, 26(8):4199–4228, 1982.

[7] N. Troullier and J. L. Martins.
Efficient pseudopotentials for plane-wave calculations.
Phys. Rev. B, 43(3):1993–2006, 1991.

[8] M. C. Payne, M. P. Teter, D. C. Allan, T. A. Arias, and J. D. Joannopoulos.
Iterative minimization techniques for ab initio total-energy calculations: molecular dynamics and conjugate gradients.
Rev. Mod. Phys., 64(4):1045–1097, 1992.

[9] E. L. Briggs, D. J. Sullivan, and J. Bernholc.
Large-scale electronic-structure calculations with multigrid acceleration.
Phys. Rev. B, 52(8):R5471–R5474, Aug 1995.

[10] T. Ono, and K. Hirose.
Timesaving Double-Grid Method for Real-Space Electronic-Structure Calculations.
Phys. Rev. Lett., 82:5016, 1999.

[11] M. Büttiker, Y. Imry, R. Landauer, and S. Pinhas.
Generalized many-channel conductance formula with application to small rings.
Phys. Rev. B, 31(10):6207–6215, May 1985.

[12] S.M. Barlow N.G. Condon F.M. Leibsle B.G. Frederick, Q. Chen and N.V. Richardson.
Orientation and periodicity in the c(4 × 8) and p(2 × 1) structures of 3-thiophene carboxylic acid on Cu(110).
Surf. Sci., 352:238, Oct 1995.

[13] N. Atodiresei, V. Caciuc, K. Schroeder, and S. Blügel.
First-principles investigation of terephthalic acid on Cu(110).
Phys. Rev. B, 76:115433, 2007.

[14] N. Atodiresei, K. Schroeder, and S. Blügel.
Density-functional theory study on the arrangement of adsorbed formate molecules on Cu(110).
Phys. Rev. B, 75.

[15] D. S. Martin, R. J. Cole, and S. Haq.
Creating a functionalized surface: The adsorption of terephthalic acid onto Cu(110).
Phys. Rev. B, 66(15):155427, Oct 2002.

[16] P. Hohenberg and W. Kohn.
Inhomogeneous electron gas.
Phys. Rev., 136:B864, 1964.

[17] J. C. Slater.
A simplification of the Hartree-Fock method.
Phys. Rev., 81:395, 1951.

[18] F. Gygi, and G. Galli.
Real-space adaptive-coordinate electronic-structure calculations.
Phys. Rev. B, 52:2229, 1995.

[19] J.-L. Fatteberg, R. D. Hornung, A.M. Wissink.
Finite element approach for density functional theory calculations on locally-refined meshes.
J. Comp. Phys., 223:759–773, 2007.

[20] K. Laasonen, R. Car, C. Lee, and D. Vanderbilt.
Implementation of ultrasoft pseudopotentials in ab initio molecular dynamics.
Phys. Rev. B, 43(8):6796–6799, 1991.

[21] P. E. Blöchl.
Projector augmented-wave method.
Phys. Rev. B, 50:17953, 1994.

[22] C. J. Pickard and F. Mauri.
Projector augmented-wave method.

Phys. Rev. B, 63:245101, 2001.

[23] M. Benzi.
Preconditioning Techniques for Large Linear Systems: A Survey.
J. Comp. Phys., 182:418–4777, 2002.

[24] P. Pulay.
Convergence Acceleration of iterative sequences. The case of SCF iteration.
Chem. Phys. Letters, 73:393, 1980.

[25] John P. Perdew, Kieron Burke, and Matthias Ernzerhof.
Generalized gradient approximation made simple.
Phys. Rev. Lett., 77(18):3865–3868, Oct 1996.

[26] H. J. Monkhorst and J. D. Pack.
Special points for Brillouin-zone integrations.
Phys. Rev. B, 13:5188, 1976.

Acknowledgements

I would like to express my gratitude to my supervisor, Dr. Tomoya Ono, for his patience with me during the time I was learning how to handle his code, for discussions and advice, but also for bringing me closer to the Japanese language and culture.

Special thanks to Prof. Dr. Stefan Blügel for his support in key situations and his strong confidence in me.

I would like to thank also Dr. Daniel Wortmann for his constructive help regarding programming in the beginning and physics in the end of this work.

Furthermore, there are many colleagues who contributed to this in various ways. Although I will not mention them all here, they should be aware that their part is one of the most important and I gratefully appreciate their support.

Selbständigkeitserklärung

Hiermit versichere ich, die vorliegende Arbeit selbständig
und nur unter Zuhilfenahme der angegebenen Quellen
und Hilfsmittel angefertigt zu haben.

Jülich im Februar 2008

(Paul Baumeister)